Chapter 6

SURFACE-ENHANCED OPTICAL PHENOMENA IN NANOSTRUCTURED FRACTAL MATERIALS

Vladimir M. Shalaev

Department of Physics, New Mexico State University, Las Cruces, New Mexico, USA

Contents

1. INTRODUCTION

A giant enhancement of optical responses in metal nanocomposites and rough thin films consisting of small nanometer-sized particles or roughness features has been intensively studied during the last few years. This enhancement is associated with optical excitation of

Handbook of Nanostructured Materials and Nanotechnology, edited by H.S. Nalwa
Volume 4: Optical Properties

ISBN 0-12-513764-8/$30.00

surface plasmons which are collective electromagnetic modes and which strongly depend on the geometrical structure of the material.

Typically, random nanocomposites and rough thin films are characterized by fractal geometry within a certain interval of sizes. The emergence of the concept of fractals was a significant breakthrough in the description of irregularity. Fractal objects are not translationally invariant and, therefore, cannot transmit running waves. Accordingly, collective excitations, such as surface plasmons, tend to be localized in fractals [1, 2]. Mathematically, this is a consequence of the fact that plane running waves are not eigenfunctions of the operator of dilation symmetry that characterizes fractals.

In fractals, collective plasmon oscillations are strongly affected by the fractal morphology, leading to the existence of "hot" and "cold" spots (i.e., areas of high and low local fields). In many cases local enhancements in the hot spots exceed the average surface enhancement by many orders of magnitude because the local peaks of the enhancement are spatially separated by distances much larger than the peak sizes. Also, the spatial distributions of these high-field regions are very sensitive to the frequency and polarization of the applied field [2–7]. The positions of the "hot spots" change chaotically but reproducibly with frequency and/or polarization. This is similar to speckle created by laser light scattered from a rough surface with the important difference that the scale size for fractal plasmons in the hot spots is in the nanometer range rather than in the micrometer range for photons.

Two classes of surface plasmons are commonly recognized: localized surface plasmons (LSP) and surface plasmon waves (SPW). [SPW are also called surface plasmon polaritons (SPP)—coherent mixture of plasmons and photons.] SPW propagate laterally along a metal surface whereas LSP are confined to metal particles that are much smaller in size than the wavelength of the incident light. However, in fractal media plasmon oscillations in different particles (roughness features) strongly interact with each other via dipolar or, more generally, multipolar forces. Thus, plasmon oscillations on a self-affine surface and in a fractal aggregate are neither conventional SPW nor independent LSP. Rather, they should be treated as collective eigenmodes arising from multipolar interactions in a fractal object.

Fractal nanostructured materials can be fabricated with the aid of well-established chemical and depositional methods. For example, colloidal clusters with the fractal dimension $D = 1.78$ can be grown in colloidal solutions via the aggregation process which is known as the cluster–cluster aggregation [8]. Alternatively, clusters with fractal dimension $D = 2.5$ can be grown by the particle-cluster aggregation process (termed the Witten–Sander aggregation or WSA [8]). Also, by controlling conditions of atomic beam deposition and substrate temperature, self-affine thin films may be grown with various fractal dimensions [9]. Finally, random metal-dielectric films (called also semicontinuous metal films) produced by metal sputtering onto an insulating substrate also include fractal clusters of metal granules near the percolation threshold [8, 9].

The fractal plasmon, as any wave, is scattered from density fluctuations. The strongest scattering occurs from inhomogeneities of the same scale as the wavelength. In this case, interference in the process of multiple scattering results in Anderson localization. Anderson localization corresponds typically to uncorrelated disorder. A fractal structure is in some sense disordered, but it is also correlated for all length scales, from the size of constituent particles, in the lower limit, to the total size of the fractal, in the upper limit. Thus, what is unique for fractals is that because of their scale invariance, there is no characteristic size of inhomogeneity—inhomogeneities of all sizes are present from the lower to the upper limit. Therefore, whatever the plasmon wavelength, there are always fluctuations in a fractal with similar sizes, so that the plasmon is always strongly scattered and, consequently, localized [2, 10].

Large fluctuations of local electromagnetic fields in inhomogeneous metal nanostructures result in several optical effects. A well-known effect of this type is the surface-

enhanced Raman scattering (SERS) by molecules adsorbed on a rough metal surface or on aggregated colloid particles [11]. A giant enhancement of nonlinear optical responses was predicted [12] for metal fractals. In an intense electromagnetic field, a dipole moment induced in a particle can be expanded into power series: $d = \alpha^{(1)}E(r) + \alpha^{(2)}[E(r)]^2 + \alpha^{(3)}[E(r)]^3 + \cdots$, where $\alpha^{(1)}$ is the linear polarizability of a particle, $\alpha^{(2)}$, $\alpha^{(3)}$ are the nonlinear polarizabilities, and $E(r)$ is the local field at the site r. The polarization of the medium (dipole moment per unit volume), which is an additional source of an electromagnetic field in a medium, can be represented in an analogous form with the coefficients called susceptibilities. When the local field considerably exceeds the applied field, $E^{(0)}$, huge enhancements of nonlinear optical responses occur. Our chapter is concerned with theoretical and experimental results obtained in this promising area.

2. SURFACE-ENHANCED OPTICAL RESPONSES

In the following text we consider enhancement of optical responses on different fractal surfaces, such as aggregates of colloidal particles, self-affine thin films, and semicontinuous metal films. We assume that each site of the surface possesses a required nonlinear polarizability, in addition to the linear one. The local fields associated with the light-induced eigenmodes of a fractal surface can significantly exceed the applied macroscopic field, $\mathbf{E}^{(0)}$. For metal surfaces, this enhancement increases toward the infrared part of the spectrum where resonance quality factors are significantly larger, in accordance with the Drude model of metal [2, 5].

2.1. Kerr-Type Nonlinearity

We begin our consideration with the Kerr-type nonlinearity, $\chi^{(3)}(-\omega; \omega, \omega, -\omega)$, that is responsible for nonlinear corrections to absorption and refraction. This type of optical nonlinearities can be used, in particular, for optical switches and optical limiters. The local nonlinear dipole, in this case, is proportional to $|\mathbf{E}(\mathbf{r})|^2\mathbf{E}(\mathbf{r})$, where $\mathbf{E}(\mathbf{r})$ is the local field at the site $\mathbf{r}$. For the resonant eigenmodes, the local fields exceed the macroscopic (average) field by a quality factor, q.

The fields generated by the nonlinear dipoles can also excite resonant eigenmodes of a fractal surface resulting in an additional "secondary" enhancement $\propto \mathbf{E}(\mathbf{r})/\mathbf{E}^{(0)}$. Accordingly, the surface-enhanced Kerr-susceptibility, $\bar{\chi}^{(3)}$, can be represented as (the angular brackets in the following formulas denote an ensemble average) [2, 5, 13],

$$\frac{\bar{\chi}^{(3)}}{p\chi^{(3)}} = G_K = \frac{\langle|\mathbf{E}(\mathbf{r})|^2[\mathbf{E}(\mathbf{r})]^2\rangle}{[\mathbf{E}^{(0)}]^4} \tag{1}$$

Here $\chi^{(3)}$ is the initial "seed" susceptibility; it can be associated with some adsorbed molecules (then, $\bar{\chi}^{(3)}$ represents the nonlinear susceptibility of the composite material consisting of the adsorbed nonlinear molecules and a surface providing the enhancement). The seed $\chi^{(3)}$ can be also associated with an isolated colloidal particle. Then, G_K represents the enhancement due to the clustering of initially isolated particles into aggregates, with the average volume fraction of metal given by p. The applied field with the frequency in the visible, near IR or IR parts of the spectrum is typically off resonance for an isolated colloidal particle (e.g., silver) but it does efficiently excite the eigenmodes of fractal aggregates of the particles; the fractal eigenmodes cover a large frequency interval including the visible and infrared parts of the spectrum [2, 5].

For simplicity, we assume that $\mathbf{E}^{(0)}$ in (1) is linearly polarized and therefore can be chosen real. The previous formula was proven [5] from rigorous first-principle considerations. Note also that G_K depends on the local-field phases and it contains both real and imaginary parts.

2.2. Four-Wave Mixing

The high local fields associated with the localized eigenmodes experience strong spatial fluctuations on a random fractal surface. Because a nonlinear optical process is proportional to the local fields raised to some high power, the resultant enhancement associated with the fluctuation area (hot spot) can be extremely large. In a sense, one can say that enhancement of optical nonlinearities is especially large in fractals because of very strong field fluctuations.

Four-wave mixing (FWM) is determined by the nonlinear susceptibility similar to (1) $\chi^{(3)}_{\alpha\beta\gamma\delta}(-\omega_s;\omega_1,\omega_1,-\omega_2)$, where $\omega_s = 2\omega_1 - \omega_2$ is the generated frequency, and ω_1 and ω_2 are the frequencies of the applied waves. Coherent anti-Stokes Raman scattering (CARS) is an example of FWM. In one elementary CARS process, two ω_1 photons are transformed into the ω_2 and ω_s photons. Another example is degenerate FWM (DFWM); this process is used for optical phase conjugation (OPC) that can result in complete removal of optical aberrations [14]. In DFWM, all waves have the same frequency ($\omega_s = \omega_1 = \omega_2$) and they differ only by their propagation directions and, in general, by polarizations. In a typical OPC experiment, two oppositely directed pump beams, with field amplitudes $\mathbf{E}^{(1)}$ and $\mathbf{E}'^{(1)}$, and a probe beam, with amplitude $\mathbf{E}^{(2)}$ (and propagating at a small angle to the pump beams), result in an OPC beam which propagates against the probe beam. Because of the interaction geometry, the wave vectors of the beams satisfy the equation $\mathbf{k}_1 + \mathbf{k}'_1 = \mathbf{k}_2 + \mathbf{k}_s = 0$. Clearly, for the two pairs of oppositely directed beams, that have the same frequency ω, the phase-matching conditions are automatically fulfilled [14].

The third-order nonlinear susceptibility, $\chi^{(3)}$, that results in DFWM, also leads to the considered nonlinear refraction and absorption that are associated with the Kerr optical nonlinearity. Note also that as in the foregoing text the nonlinear susceptibility, $\chi^{(3)}$, can be associated with either the fractal surface itself or the molecules adsorbed on the surface.

For coherent effects, including the ones discussed in this section, averaging is performed for the generated field amplitude (rather than intensity) or, equally, for the nonlinear polarization of a medium. The average polarization, $P^{(3)}(\omega)$, is proportional to the nonlinear susceptibility, $P^{(3)}(\omega) \propto \bar{\chi}^{(3)} = \chi^{(3)} G_K$. The measured signal for coherent processes is proportional to $|\bar{\chi}^{(3)}|^2$. Thus we conclude that the resultant enhancement for degenerate (or near degenerate) four-wave mixing can be expressed in terms of the enhancement for the Kerr-susceptibility as follows [5],

$$G_{\mathrm{FWM}} = |G_K|^2 = \left| \frac{\langle |\mathbf{E}(\mathbf{r})|^2 [\mathbf{E}(\mathbf{r})]^2 \rangle}{[\mathbf{E}^{(0)}]^4} \right|^2 \tag{2}$$

Note that one can equally describe a medium optical response in terms of the nonlinear currents rather than the nonlinear polarizations; these two approaches are completely equivalent [7] (see Section 5).

2.3. Raman Scattering

Although Raman scattering is a linear optical process, the surface-enhanced Raman scattering at small Stokes shifts is proportional to the fourth power of the local fields [5, 11], so that the average enhancement factor is [5],

$$G_{RS} = \frac{\langle |\mathbf{E}(\mathbf{r})|^4 \rangle}{[\mathbf{E}^{(0)}]^4} \tag{3}$$

Note that in contrast to the enhanced Kerr-nonlinearity considered earlier, G_{RS} is real and the local enhancement is phase insensitive, so that there is no destructive interference of signals from different points of a surface. As a result, G_{RS} is, typically, larger than G_K.

2.4. Harmonic Generation

Under some simplifying conditions, the enhancement for the second harmonic generation (SHG) can be written as [2],

$$G_{\mathrm{SHG}} = \left| \left\langle \left[\frac{E_\omega(\mathbf{r})}{E_\omega^{(0)}} \right]^2 \left[\frac{E_{2\omega}(\mathbf{r})}{E_{2\omega}^{(0)}} \right] \right\rangle \right|^2 \tag{4}$$

where $E_{2\omega}^{(0)}$ and $E_{2\omega}(\mathbf{r})$ are the macroscopic and local *linear* fields at frequency 2ω. If there is no enhancement at frequency 2ω, then $E_{2\omega}(\mathbf{r}) = E_{2\omega}^{(0)}$.

The previous formula can be easily generalized for the nth harmonic generation (nHG),

$$G_{n\mathrm{HG}} = \left| \left\langle \left[\frac{E_\omega(\mathbf{r})}{E_\omega^{(0)}} \right]^n \left[\frac{E_{n\omega}(\mathbf{r})}{E_{n\omega}^{(0)}} \right] \right\rangle \right|^2 \tag{5}$$

Note that the previous formulas are valid for an arbitrary surface fractal or nonfractal. In fractals, however, because of the extremely large field fluctuations the ensemble-average enhancements are typically much larger than for nonfractal surfaces. In addition, the fractal modes provide enhancements in a very large spectral range including the infrared part, where the enhancement is particularly large because of the high quality factor for metal surfaces in this spectral range [2]. We also show in the following text that the local enhancements in the hot zones (associated with the localized eigenmodes) can exceed the ensemble-average enhancement by many orders of magnitude.

3. FRACTAL AGGREGATES OF COLLOIDAL PARTICLES

As well known, there is only one dipolar mode that can be excited by a homogeneous field in a spherical object. For a three-dimensional (nonfractal) collection of small particles, such as randomly close-packed hard spheres of particles or a random gas of particles, absorption spectra are peaked near the relatively narrow resonance of the individual particles, that is, all eigenmodes of a collection of particles are located within a small spectral interval [5].

In contrast to such conventional (nonfractal) three-dimensional systems, dipolar interactions in low-dimensional fractal clusters are not long range. This results in the spatial localization of the eigenmodes at various random locations in the cluster [2–7, 10]. The spectrum of these eigenmodes exhibits strong inhomogeneous broadening as a result of the spatial variability of the local environment. It is also important to note that, despite the asymptotically zero mean density of particles in a fractal cluster, a high probability always exists of finding a number of particles in close proximity to a given particle (stated more precisely, in fractals, the pair correlation $g \propto r^{D-d}$ $(D < d)$, where D is the fractal dimension and d is the dimension of the embedding space; accordingly, g becomes large at small r). Thus, objects with fractal morphology possess an unusual combination of properties. Namely, despite the fact that the volume fraction, p, filled by $N = (R_c/R_0)^D$ particles in a fractal (R_c and R_0 are the size of a fractal cluster and a typical separation between neighbor particles, respectively) is very small, $p \propto N^{1-d/D} \to 0$, strong interactions nevertheless exist between neighboring particles [2]. These strong interactions between neighboring particles, which are highly variable because of the variability of local particle configurations in a cluster, lead to the formation of inhomogeneously broadened eigenmodes covering a broad spectral range [2, 4, 5].

Localization of eigenmodes in fractals leads to a patchworklike distribution of the local fields associated with hot and cold zones [2–5, 10]. This, in turn, results in large spatial fluctuations of local fields in fractal composites and in giant enhancements of various optical effects [2–7, 10, 12, 15].

For the special case of fractals formed by metal particles, the dipole eigenmodes span the visible and the infrared regions of the spectrum; because the mode quality factors

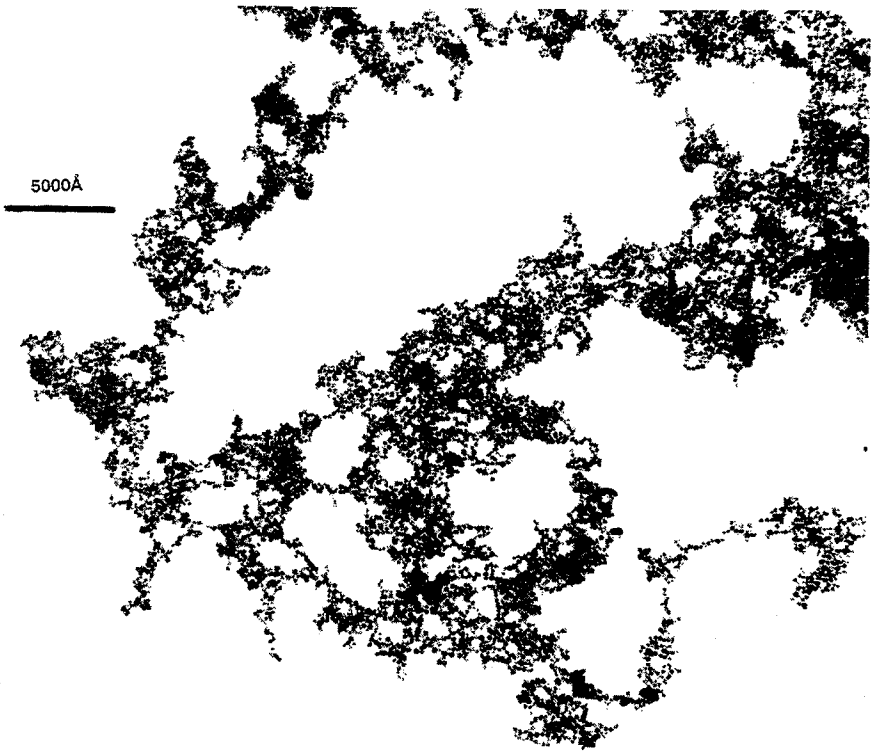

Fig. 1. Electron microscope picture of a fractal aggregate of silver colloidal particles. (Source: Reprinted with permission from I. Stockman, V. M. Shalaev, M. Moskovits, R. Botet, and T. F. George, *Phys. Rev. B* 46, 2821 [1992]. © 1992 American Physical Society.)

increase with wavelength, local fields are especially large in the long-wavelength part of the spectrum [2, 5].

An electron microscope picture of a fractal aggregate of silver colloidal particles is shown in Figure 1. The fractal dimension of these aggregates is $D \approx 1.78$. Using the well-known model of cluster–cluster aggregation, colloidal aggregates can be readily simulated numerically [8]. Note that voids are present at all scales from the minimum one (about the size of a single particle) to the maximum one (about the size of the whole cluster). This is an indication of the statistical self-similarity of a fractal cluster. The size of an individual particle is $\sim$10 nm, whereas the size of the whole cluster is $\sim 1\ \mu$m.

The process of aggregation can be described as follows. A large number of initially isolated silver nanoparticles execute random walks in the solution. Encounters with other nanoparticles result in their sticking together, first to form small groups, which then aggregate into larger formations, and so on. The "cluster–cluster aggregates" (CCA) having fractal dimension $D \approx 1.78$ are eventually formed.

3.1. Coupled-Dipole Equations

As shown in Section 2, enhancement for various optical phenomena on random surfaces can be expressed in terms of the local fields. For calculations of the local fields we solve the coupled-dipole equations (CDE) describing an optical response of an arbitrary collection of N identical polarizable particles (monomers) possessing a linear scalar polarizability α. When irradiated by a plane monochromatic incident wave of the form,

$$\mathbf{E}_{\text{inc}}(\mathbf{r}, t) = \mathbf{E}^{(0)} \exp(\mathrm{i}\mathbf{k} \cdot \mathbf{r} - \mathrm{i}\omega t) \tag{6}$$

the monomers interact with the incident field and with each other through induced dipole moments. The local electric field $\mathbf{E}_i$ at the monomer's position $\mathbf{r}_i$ is given by the sum of the incident wave and all the scattered (secondary) waves: $\mathbf{E}_i = \mathbf{E}_{\text{inc}}(\mathbf{r}_i, t) + \mathbf{E}_{sc}(\mathbf{r}_i, t)$. The dipole moment $\mathbf{d}_i$ at the ith site is determined as

$$\mathbf{d}_i = \alpha_0 \mathbf{E}_i \tag{7}$$

The field $\mathbf{E}_{sc}(\mathbf{r}_i)$, scattered from all other dipoles, generally, contains the near-, intermediate-, and far-zone terms. We restrict our consideration to the quasi-static limit, that is, the characteristic system size L is assumed to be much smaller than the wavelength $\lambda = 2\pi c/\omega$. In this approximation, we leave only the near field term in the expression for $\mathbf{E}_{sc}(\mathbf{r}_i)$ and the factor $\exp(\mathrm{i}\mathbf{k}\cdot\mathbf{r}_i)$ is always close to unity. In addition, the time dependence, $\exp(-i\omega t)$, is the same for all time-varying fields, so that the whole exponential factor can be omitted. After that, the coupled-dipole equations (CDE) for the induced dipoles acquire the following form [2, 10],

$$d_{i,\alpha} = \alpha_0 \left(E_\alpha^{(0)} + \sum_{j \neq i} W_{ij,\alpha\beta} d_{j,\beta} \right) \tag{8}$$

$$W_{ij,\alpha\beta} = \frac{3 r_{ij,\alpha} r_{ij,\beta} - \delta_{\alpha\beta} r_{ij}^2}{r_{ij}^5} \tag{9}$$

where $W_{ij,\alpha\beta}$ is the quasi-static interaction operator between two dipoles, $\mathbf{r}_i$ is the radius vector of the ith monomer, and $\mathbf{r}_{ij} = \mathbf{r}_i - \mathbf{r}_j$. The Greek indices denote Cartesian components of vectors and should not be confused with the polarizability, α_0. Hereafter, summation over repeated Greek indices is implied, except if stated otherwise.

The linear polarizability of an elementary dipole representing a spherical monomer, α_0, is given by the Lorenz–Lorentz formula (see, for example, [16]),

$$\alpha_0 = R_m^3 \frac{\varepsilon - \varepsilon_h}{\varepsilon + 2\varepsilon_h} \tag{10}$$

where $\varepsilon = \varepsilon' + i\varepsilon''$ is the bulk dielectric permittivity of the film material and ε_h is the dielectric constant of the host material.

Because $W_{ij,\alpha\beta}$ is independent of the frequency ω in the quasi-static approximation, the spectral dependence of solutions to (8) is manifested only through $\alpha_0(\omega)$. For convenience, we introduce the variable $Z(\omega) \equiv 1/\alpha(\omega) = -[X(\omega) + \mathrm{i}\delta(\omega)]$. Using Eq. (10), we obtain

$$X \equiv -\mathrm{Re}\left[\alpha_0^{-1}\right] = -R_m^{-3}\left[1 + \frac{3\varepsilon_h(\varepsilon' - \varepsilon_h)}{|\varepsilon - \varepsilon_h|^2}\right] \tag{11}$$

$$\delta \equiv -\mathrm{Im}\left[\alpha_0^{-1}\right] = 3R_m^{-3}\frac{\varepsilon_h \varepsilon''}{|\varepsilon - \varepsilon_h|^2} \tag{12}$$

The variable X indicates the proximity of ω to an individual particle resonance occurring at $\varepsilon' = -2\varepsilon_h$ and it plays a role of a frequency parameter; δ characterizes dielectric losses. The resonance quality factor is proportional to δ^{-1}. One can find $X(\lambda)$ and $\delta(\lambda)$ for any material using theoretical or experimental data for $\varepsilon(\lambda)$ and formulas (11) and (12).

In Figure 2a and b, we plot X and δ as functions of the wavelength λ for silver in water and vacuum using the tabulated data for ε [17], (the units in which $(4\pi/3)R_m^3 = 1$ are used). As seen in the figure, X changes significantly from 400 to 800 nm and then, for longer wavelengths, remains almost constant, $X \approx -4\pi/3$. The relaxation constant is small in the visible spectral range and decreases toward the infrared.

For metal particles, the dielectric function is well described by the Drude formula

$$\varepsilon = \varepsilon_0 - \frac{\omega_p^2}{\omega(\omega + i\Gamma)} \tag{13}$$

where ε_0 includes the contribution to the dielectric constant associated with interband transitions in bulk material, ω_p is the plasma frequency and Γ is the relaxation constant.

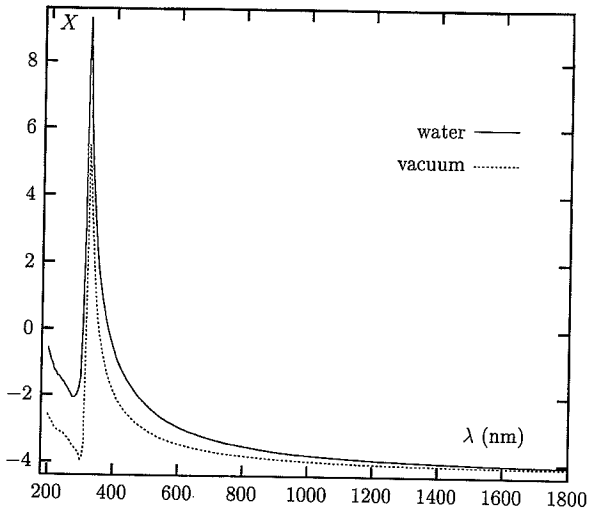

(a)

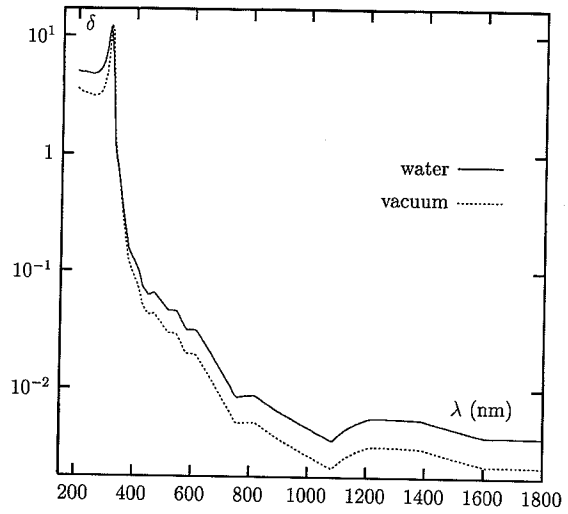

(b)

Fig. 2. Spectral dependence of the frequency parameter, X, and loss parameter, δ, for silver. (Source: Reprinted with permission from V. A. Markel, V. M. Shalaev, E. B. Stechel, W. Kim, and R. L. Armstrong, *Phys. Rev. B* 53, 2425 [1996]. © 1996 American Physical Society.)

Now we write Eq. (8) in a matrix form. Following Refs. [2, 5, 10], we introduce a $3N$-dimensional vector space R^{3N} and an orthonormal basis $|i\alpha\rangle$. The $3N$-dimensional vector of dipole moments is denoted by $|d\rangle$, and the incident field is denoted by $|E_{\text{inc}}\rangle$. The Cartesian components of three-dimensional vectors $\mathbf{d}_i$ and $\mathbf{E}_{\text{inc}}$ are given by $\langle i\alpha|d\rangle = d_{i,\alpha}$ and $\langle i\alpha|E_{\text{inc}}\rangle = E_{0,\alpha}$. The last equality follows from the assumption that the incident field is uniform throughout the film. The matrix elements of the interaction operator are defined by $\langle i\alpha|\widehat{W}|j\beta\rangle = W_{ij,\alpha\beta}$. Then Eq. (8) can be written as

$$\left[Z(\omega) - \widehat{W}\right]|d\rangle = |E_{\text{inc}}\rangle \tag{14}$$

The interaction operator $\widehat{W}$ in (14) is real and symmetrical, as it can be easily seen from the expression (9) for its matrix elements.

By diagonalizing the interaction matrix $\widehat{W}$ with $\widehat{W}|n\rangle = w_n|n\rangle$ and by expanding the $3N$-dimensional dipole vectors in terms of the eigenvectors $|n\rangle$ (as $|d\rangle = \sum_n C_n|n\rangle$), we obtain a relation between the local fields and the amplitudes of linear dipoles induced by

the incident wave (6) [2, 5, 10],

$$E_{i,\alpha} = \alpha_0^{-1} d_{i,\alpha} = \alpha_0^{-1} \alpha_{i,\alpha\beta} E_{0,\beta} \tag{15}$$

where we introduced the polarizability tensor of the ith dipole, $\hat{\alpha}_i(\omega)$, with its matrix elements, $\alpha_{i,\alpha\beta}$, given by

$$\alpha_{i,\alpha\beta} \equiv \alpha_{i,\alpha\beta}(\omega) = \sum_{j,n} \frac{\langle i\alpha|n\rangle\langle n|j\beta\rangle}{Z(\omega) - w_n} \tag{16}$$

The local dipoles, according to (15), are expressed in terms of the eigenmodes as follows,

$$d_{i,\alpha} = \sum_n \frac{\langle i\alpha|n\rangle\langle n|E_{\text{inc}}\rangle}{Z(\omega) - w_n} = \sum_{n,j} \frac{\langle i\alpha|n\rangle\langle n|j\beta\rangle}{Z(\omega) - w_n} E_{0,\beta} \tag{17}$$

Equations (15) and (16) allow one to express the local fields in terms of the eigenfunctions and eigenfrequencies of the interaction operator; the local fields then can be used to calculate enhancements of optical phenomena, using the formulas of Section 2.

The average cluster polarizability is given by

$$\alpha = \frac{1}{3N} \sum_i \text{Tr}[\alpha_{\alpha\beta}^{(i)}] \tag{18}$$

The extinction cross-section σ_e is expressed through the imaginary part of the polarizability as

$$\sigma_e = 4\pi k N \,\text{Im}\,\alpha \tag{19}$$

For small clusters scattering can be neglected so that the extinction cross-section is approximately equal to the absorption cross-section.

From (16) and (18) the following useful sum rules can be obtained [10],

$$\int \text{Im}\,\alpha(X) = \pi \qquad \int X\,\text{Im}\,\alpha(X)\,dX = 0 \tag{20}$$

3.2. Absorption Spectra in Fractal Aggregates

In the following text we discuss results of our numerical and experimental studies of the extinction (absorption) spectra of fractal aggregates of nanoparticles.

To simulate the silver colloid aggregates studied in our experiment, we used the cluster–cluster aggregation model [8]. The cluster–cluster aggregates (CCA) have fractal dimension, structure, and aggregation pattern very similar to those observed in the experiment. The CCA were built on a cubic lattice with periodic boundary conditions using a well-known algorithm [8].

In Figure 3, the absorption spectrum, $\text{Im}\,\alpha(X)$, as function of the frequency parameter X is shown for CCA (the units $a = 1$ are used, where a is the lattice period). The simulations were performed for clusters consisting of $N = 500$ and $N = 10{,}000$ particles each. Note the spectrum reflects a strong inhomogeneous broadening in CCA; the spectrum width is much larger than the resonance width for an individual monomer which is δ (in the simulations we used $\delta = 0.1$).

The used CCA model contains two adjustable parameters, the lattice period, a, which defines the relative distances, r_{ij}, between particles, and the radius of a monomer, R_m. Clearly, solutions of the CDE are very sensitive to the ratio a/R_m, because this parameter determines the interaction strength. The model of geometrically touching spheres, which seems to be the most natural, implies that $a/R_m = 2$. However, as was shown in Ref. [18], this model fails to describe the long-wavelength resonances observed in a group of particles; it also fails to describe the long-wavelength tail observed in the absorption spectra of colloid aggregates (see, for example, Refs. [15] and [19]).

The physical reason for the failure of this model is that the dipole approximation is not strictly applicable for touching spheres [18, 20–23]. Indeed, the dipole field produced

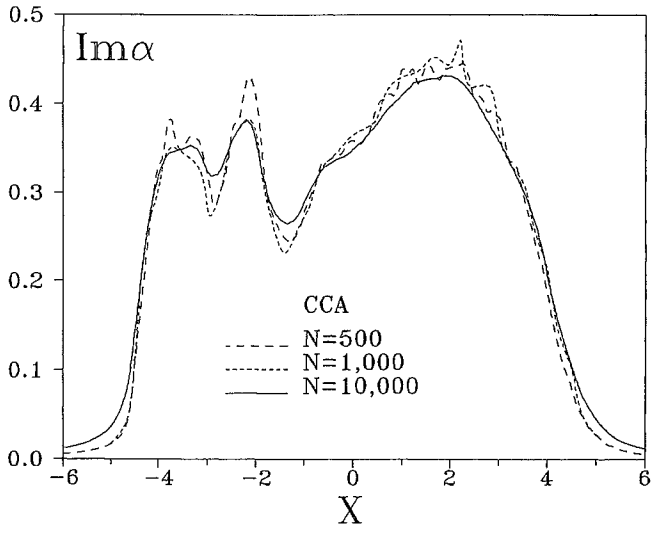

Fig. 3. Calculated absorption spctra, $\mathrm{Im}\,\alpha(X)$, for cluster–cluster aggregates containing a different number of particles, $N = 500$, $N = 1000$, and $N = 10{,}000$. (Source: Reprinted with permission from V. A. Markel, V. M. Shalaev, E. B. Stechel, W. Kim, and R. L. Armstrong, *Phys. Rev. B* 53, 2425 [1996]. © 1996 American Physical Society.)

by one of the touching monomers is highly inhomogeneous ($\propto r^{-3}$) within the volume of the other one. This inhomogeneous field should result in high-order multipole moments, coupled both to each other and to the incident field. The high-order moments, when they are taken into account, effectively increase depolarization factors, and lead to the low-frequency resonances observed in experiments [18]. However, incorporating these high-order moments into the calculation results in an essentially intractable problem for the large fractal clusters considered here.

As suggested by Purcell and Pennypacker [24], and developed by Draine [25], a description of the optical response of an arbitrary shaped object can be obtained, remaining within the dipole approximation. (It is worth noting that the macroscopic Maxwell equations also contain only dipolar terms, i.e., polarization.) In the following text we generalize these ideas for fractal aggregates.

To account for multipolar effects in the CDE, real touching spheres may be replaced by effective spheres which geometrically intersect. Formally, this requires the ratio a/R_m to be taken less than 2. The physical reason underlying this procedure can be understood from the following arguments. Consider a pair of touching spheres and ascribe to the first sphere a dipole moment d located at its center. Because we would like to remain within the dipole approximation, the second sphere should also be replaced by a point dipole located at a certain distance from the first sphere. Clearly, because the field associated with the first sphere decreases nonlinearly, $\sim d/r^3$, the second dipole should be placed somewhere closer than $2R_m$ from the center of the first sphere (otherwise, the interaction between the spheres would be underestimated). In other words, in order to correctly describe the interaction between the spheres remaining within the dipolar approximation, the distance between the dipoles must be taken less than $2R_m$. This is equivalent to replacing the original touching spheres by overlapping spheres with the dipole moments located at their centers.

To gain insight concerning selection of the ratio a/R_m, we first consider cases for which a/R_m is known exactly. As shown in Refs. [24–26], the correct description of the optical response of a small object of arbitrary shape was obtained by considering the dipolar interactions of a set of spherical monomers placed on a simple cubic lattice inside the volume of the object; the lattice period, a, was chosen such that $a^3 = (4\pi/3)R_m^3$. This relation which provides equality of the total volume of the spheres and the original object under

consideration, gives the ratio $a/R_m = (4\pi/3)^{1/3} \approx 1.612$. In Ref. [27] it was shown that, within the dipole approximation, correct depolarization coefficients for a linear array of spherical monomers are obtained provided a/R_m is chosen to be $(4\zeta_3)^{1/3} \approx 1.688$ ($\zeta_3 = \sum_k k^{-3}$), that is, close to the previously mentioned value. We used $a/R_m = (4\pi/3)^{1/3}$ in our calculations.

We also require that the radius of gyration R_c and the total mass of clusters used in the simulations must be the same as in the experiment. This condition, combined with $a/R_m = (4\pi/3)^{1/3}$, can be satisfied for fractals ($D \neq 3$) if one chooses $R_m = R_{\text{exp}}(\pi/6)^{D/[3(3-D)]}$, where R_{exp} is the radius of monomers used in experiments. In our experiments described later, the radius of silver particles forming colloidal aggregates was $R_{\text{exp}} \approx 7$ nm, so that $R_m \approx 5$ nm for $D = 1.78$.

For a light beam propagating in a system which contains randomly distributed clusters far away from each other (so that the clusters do not interact), the intensity dependence is given by the expression $I(z) = I(0)\exp(-\sigma_e \varsigma z)$, where ς is the cluster density, $\varsigma = p/[(4\pi/3)R_{\text{exp}}^3\langle N\rangle]$, and p is the volume fraction filled by spherical particles. Introducing the extinction efficiency,

$$Q_e = \frac{\langle\sigma_e\rangle}{\langle N\rangle \pi R_{\text{exp}}^2} = \frac{4k\,\text{Im}\,\alpha}{R_{\text{exp}}^2} \tag{21}$$

the intensity dependence $I(z)$ acquires the form,

$$I(z) = I(0)\exp\left[-\frac{3}{4}Q_e p\frac{z}{R_{\text{exp}}}\right]. \tag{22}$$

As follows from (22) the extinction efficiency Q_e is the quantity that is measured in experiments on light transmission (rather than σ_e).

In Refs. [4, 5, 15] experiments were performed to measure extinction in silver colloid aggregates. In [5] fractal aggregates of silver colloid particles were produced from a silver sol generated by reducing silver nitrate with sodium borohydride [28]. The color of fresh (nonaggregated) colloidal solution is opaque yellow; the corresponding extinction spectrum (see Fig. 4) peaks at 400 nm with the halfwidth about 40 nm. Addition of adsorbent

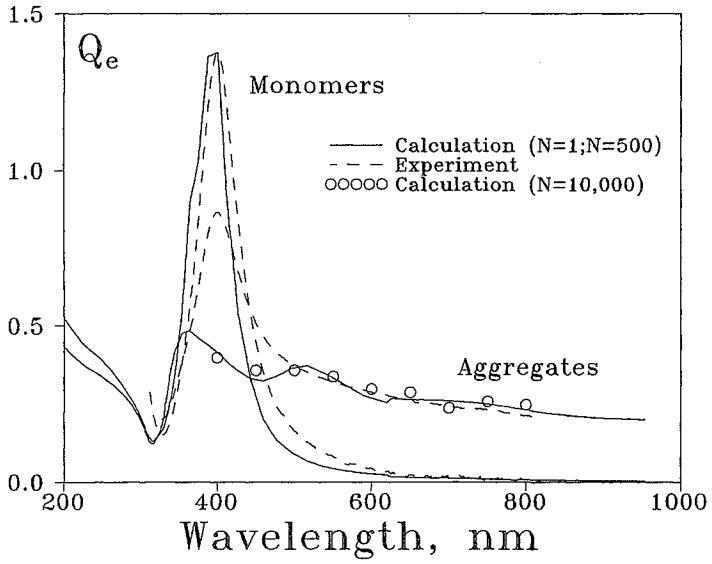

Fig. 4. Experimental and calculated extinction spectra of silver colloid CCA. The theoretical spectra are presented for 500-particle and 10,000-particle CCA. (Source: Reprinted with permission from V. A. Markel, V. M. Shalaev, E. B. Stechel, W. Kim, and R. L. Armstrong, *Phys. Rev. B* 53, 2425 [1996]. © 1996 American Physical Society.)

(fumaric acid) promoted aggregation, and fractal colloid clusters formed. When adding the fumaric acid (0.1 cm^3 of 0.5 M aqueous solution) into the colloids (2.0 cm^3), the colloid's color changed through dark orange and violet to dark grey over 10 h. Following aggregation, a large wing in the long wavelength part of the spectrum appeared in the extinction, as seen from Figure 4. Note to plot Figure 4, we used the results of Figure 3, where X was expressed in terms of λ for silver particles (see Fig. 2).

A broadening of absorption spectra of silver colloidal aggregates due to the interaction between particles constituting the aggregates is well seen in Figure 4 [5, 29, 30]. The results of calculation of the absorption wing shape by the coupled-dipoles method describe experimental data fairly well [5, 29, 30].

The calculations were performed for 500-particle CCA (solid line with a large wing) and for 10,000-particle CCA (circles) [5]. Clearly, the aggregation results in a large tail in the red and infrared part of the spectrum, which is well described by the simulations. The discrepancy in the central part of the spectrum probably occurs because, in the experiments, a number of particles remained nonaggregated and led to additional (not related to fractal aggregates) absorption near 400 nm.

3.3. Local-Field Enhancements in Fractal Aggregates

We now discuss the enhancement of local fields in small-particle composites. The parameter characterizing the enhancement of local-field intensity can be defined as

$$G = \frac{\langle |E_i|^2 \rangle}{|E^{(0)}|^2} \tag{23}$$

The enhancement G is related to $\mathrm{Im}\,\alpha(X)$ as follows [10] (see (15), (16), and (18)),

$$G = \delta\left[1 + \frac{X^2}{\delta^2}\right]\mathrm{Im}\,\alpha \tag{24}$$

According to Eq. (24), the enhancement factor $G \approx (X^2/\delta)\mathrm{Im}\,\alpha$ for $|X| \gg \delta$, that is, it can be very large.

Note that, because in fractals the fluctuations are very large so that $\langle |E|^2 \rangle \gg \langle |E| \rangle^2$ [2, 10], we have $\langle |\Delta E|^2 \rangle \approx \langle |E|^2 \rangle$; therefore, in this case, G characterizes both the enhancement of local fields and their fluctuations as well. In other words, the larger the fluctuations, the stronger the enhancement.

In the following text we consider results of numerical simulations of G for cluster–cluster aggregates (CCA) having fractal dimension $D \approx 1.78$, and for two nonfractal ensembles of particles: a random gas of particles (RGP) and a close-packed sphere of particles (CPSP). While RGP is a very dilute system of particles randomly distributed in space, CPSP represents a dense (but still random) system of particles. In both cases $D = d = 3$ and the correlation function $g(r)$ is constant. The particles were assumed to be hard spheres. To provide better comparison with CCA, the RGP was generated in a spherical volume that would be occupied by a CCA with the same number of particles; this means that particles in CCA and RGP fill the same volume fraction, p (p was small, $p \approx 0.05$ for $N = 500$). In contrast, a fairly dense packing of spherical particles, with $p \approx 0.44$, was used for CPSP.

In Figure 5 results of the simulations for the enhancement factor G in silver CCA in vacuum are compared with those for nonfractal composites, RGP and CPSP [5]. (The material optical constants for silver were taken from Ref. [17].) As seen in Figure 5, the enhancement of local-field intensities in fractal CCA is significantly larger than in nonfractal RGP and CPSP clusters, as was anticipated. The enhancement can reach very high values, $\sim 10^3$, and increases with λ. This occurs because both the localization of fractal eigenmodes and their mode quality factor ($q \sim 1/\delta \sim |\varepsilon - \varepsilon_h|^2/3\varepsilon''\varepsilon_h$) increase for the modes in the long-wavelength part of the spectrum.

We next consider a more detailed comparison between fractal small-particle composites and nonfractal inhomogeneous media. The simulations were performed for RGP and CCA

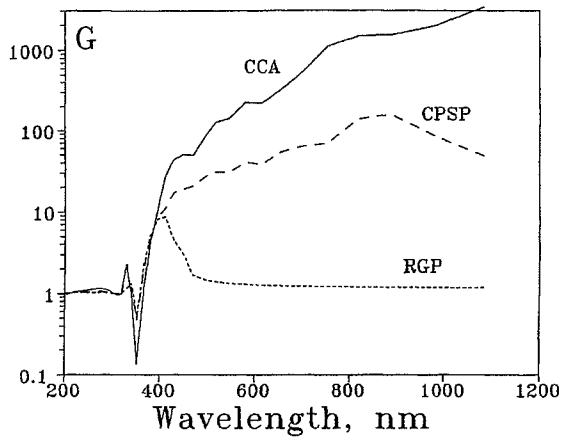

Fig. 5. Enhancement factors, G, of local-field intensities plotted against λ for 500-particle aggregates: CCA (solid line), a random gas of particles (RGP) with the same as for a CCA volume fraction of metal (short-dashed line), and a close-packed sphere of particles, CPSP, (long-dashed line). (Source: Reprinted with permission from V. M. Shalaev, E. Y. Poliakov, and V. A. Markel, *Phys. Rev. B* 53, 2437 [1996]. © 1996 American Physical Society.)

having the same volume fraction p filled by metal. The volume fraction p of particles in a fractal cluster is very small. (In fact, $p \to 0$ at $R_c \to \infty$; but p is, of course, finite for a finite number of particles.) According to the Maxwell-Garnett theory [2], there is only one resonant frequency in conventional ($d = D$) media with $p \ll 1$; the resonance is just slightly shifted from the resonance of an isolated particle at $X(\omega) = 0$. In contrast, in fractal media, despite the fact that p is asymptotically zero, there is a high probability of finding a number of particles close to any given one. (This is because the pair correlation function, $g(r) \propto r^{D-d}$, increases with decreasing distance r between particles.) Thus, in fractals there is always a strong interaction of a particle with others distributed in its random neighborhood. As a result, there exist localized eigenmodes with distinct spatial orientations in different parts of a cluster, where the location depends on the frequency and polarization characteristics of the mode. As mentioned earlier, some of these modes are significantly shifted to the red part of the spectrum where their quality factors q are much larger than that at $X(\omega) = 0$, for a noninteracting particle. Thus, the dipole–dipole interactions of constituent particles in a fractal cluster "generate" a wide spectral range of resonant modes with enhanced quality factors and with spatial locations which are very sensitive to the frequency and polarization of the applied field. The localization of modes in various random parts of a cluster also brings about giant spatial fluctuations of the local fields, when one moves from hot to cold zones corresponding to high- and low-field-intensity areas, respectively.

In the case of a CPSP, the volume fraction, p, is not small. However, because the dipole–dipole interaction for a three-dimensional CPSP is long range, one expects that eigenmodes are delocalized over the whole sample so that all particles are involved in the excitation. Accordingly, fluctuations (and enhancements) of local fields are much smaller than in a fractal aggregate where the modes are localized.

As seen in Figure 5, enhancements and fluctuations of local fields in nonfractal CPSP and RGP are significantly less than those in the case of fractal CCA, in accordance with the foregoing arguments.

The localized optical modes in fractal aggregates can be imaged using photon scanning tunneling microscopy (PSTM) providing subwavelength spatial resolution. In [31], fractal aggregates of silver colloidal particles were prepared originally in solution, then deposited onto a glass prism and the water was soaked out. The optical images were taken at different light wavelengths and polarizations. The near-field optical images shown in Figure 6 exhibit spatially localized (within 150–250 nm) intensity enhancement $10\times$ and more for different wavelengths and polarizations. The spatial positions of the hot spots changes with

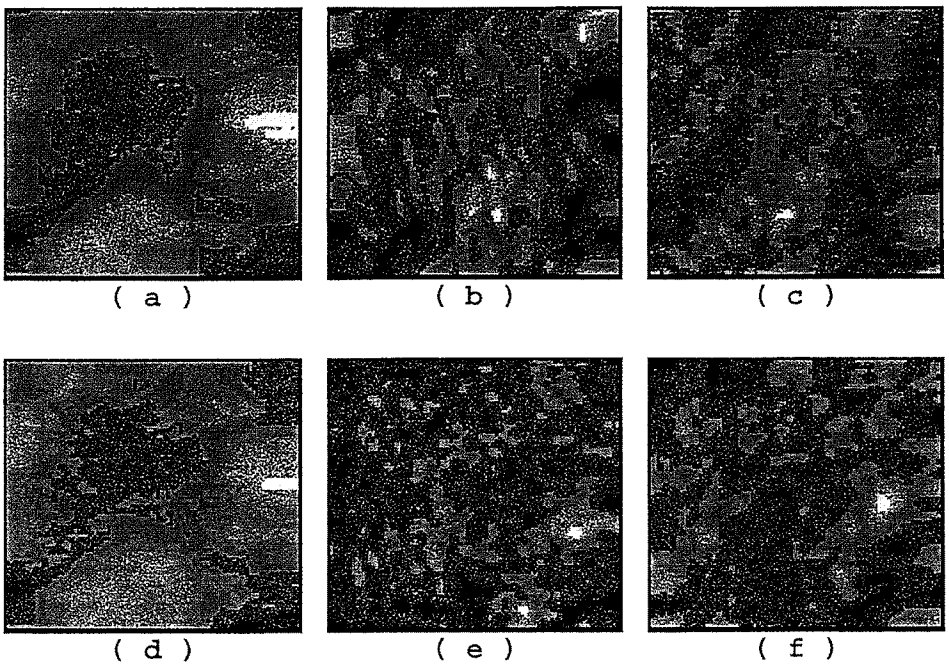

Fig. 6. Gray-scale (a, d) topographical and (b, c, e, f) near-field optical images (4.4×4.4 μm) of the same area of the sample surface taken with $\lambda = 633$ nm, (b) s- and (c) p-polarized laser beams, and with $\lambda = 594$ nm, (e) s-, and (f) p-polarized laser beams. (Source: Reprinted with permission from [31]. © 1998 American Physical Society.)

both wavelength and polarization, as predicted by the theory. Similar results were earlier reported in Ref. [3].

The enhanced local fields result in enhancements of the optical processes considered later. Based on the simulations presented in the preceding text, one anticipates that in fractal composites, where the fluctuations are strong, the enhancements can be very large. In the following text, we analyze various enhanced optical phenomena in fractal aggregates of nanoparticles.

3.4. Surface-Enhanced Optical Phenomena in Fractal Aggregates

In this section, using general formulas of Section 2 and the calculated values of the local fields (see (15) and (16)), we consider the surface-enhanced optical phenomena in fractal aggregates. Theoretical results are compared with experimental studies.

We begin with Raman scattering. In Figure 7 results of our theoretical calculations and experimental studies of surface-enhanced Raman scattering (SERS) in fractal aggregates of silver colloidal particles are shown [5, 11]. As seen in the figure, the theory successfully explains the experimental observations. Note that the enhancement is large and increases toward the near infrared part of the spectrum, where the local fields associated with the localized fractal modes are significantly larger (cf., Fig. 5).

In Figure 8a and b, we show results of our calculations for the real, G'_K, and imaginary, G''_K, parts of the enhancement for the Kerr-nonlinearity defined in (1)); in Figure 8c, the enhancement for the degenerate four-wave mixing in silver colloidal aggregates, $G_{\mathrm{FWM}} = |G_K|^2$. The enhancement factors increase toward the infrared part of the spectrum where the resonance quality factors are larger and the localization of the eigenmodes is stronger [2, 5].

The nonlinear susceptibility, $\bar{\chi}^{(3)}$ of the composite material consisting of fractal aggregates of colloidal particles in solution is given by $\bar{\chi}^{(3)} = p \cdot G_K \chi_m^{(3)}$, where $\chi_m^{(3)}$ is

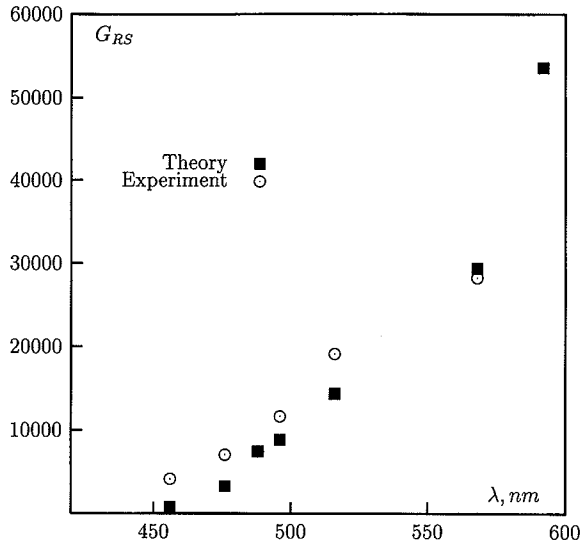

Fig. 7. Theoretical and experimental enhancement factors, G_{RS}, for silver colloid aggregates as a function of the wavelength. (Source: Reprinted with permission from V. M. Shalaev, E. Y. Poliakov, and V. A. Markel, *Phys. Rev. B* 53, 2437 [1996]. © 1996 American Physical Society.)

the susceptibility of the nonaggregated colloidal particles and p is the volume fraction filled by metal. The experimentally measured value [15, 29, 30] of $\chi_m^{(3)}$ for nonaggregated silver monomers at $\lambda = 532$ nm is $\chi_m^{(3)} \approx 10^{-8}$ esu. The value of $\chi_m^{(3)}$ re-estimated for $\lambda = 532$ nm from the data [32] is close to the foregoing value.

When the initially separated silver particles aggregate and fractal clusters are formed, a huge enhancement of the cubic susceptibility is observed [15]. The enhancement factor as high as 10^6 was obtained for degenerate four-wave mixing. As follows from Figure 8c, the calculated value of G_{FWM} agrees satisfactorily in the order of magnitude with the measured one for $\lambda = 532$ nm. The cubic susceptibility obtained experimentally for an aggregated sample was [30] $|\bar{\chi}^{(3)}| = 5.7 \cdot 10^{-10}$ esu with $p \approx 5 \cdot 10^{-6}$. Note that p is a variable quantity and can be increased. We can assign the value 10^{-4} esu to the nonlinear susceptibility, $\chi^{(3f)}$, of fractal aggregates, that is, $\bar{\chi}^{(3)} = p \cdot \chi^{(3f)}$, with $\chi^{(3f)} \sim 10^{-4}$ esu. This is a very large value for the third-order nonlinear susceptibility.

In the other series of experiments, using the Z-scan technique [33], both nonlinear refraction and absorption were measured [29, 30]. It has been found that for $\lambda = 540$ nm and $p = 5 \cdot 10^{-6}$, the aggregation of silver colloidal particles into fractal clusters is accompanied by the increase of the nonlinear correction, α_2, to the absorption, $\alpha_{\mathrm{abs}}(\omega) = \alpha_{\mathrm{abs},0} + \alpha_2 I$, from $\alpha_2 = -9 \cdot 10^{-10}$ cm/W to $\alpha_2 = -5 \cdot 10^{-7}$ cm/W, that is, the enhancement factor is 560 [29] (I is the laser intensity). The measured nonlinear refraction at $\lambda = 540$ nm for fractal aggregates of silver colloidal particles is $n(\omega) = n_0 + n_2 I$, with $n_2 = 2.3 \cdot 10^{-12}$ cm^2/W. Similar measurements at $\lambda = 1079$ nm give the following values $n_2 = -0.8 \cdot 10^{-12}$ cm^2/W and $\alpha_2 = -0.7 \cdot 10^{-7}$ cm/W.

The measured n_2 and α_2 allow one to find the real and imaginary parts of the Kerr-susceptibility [14, 33]; they are $\mathrm{Re}[\bar{\chi}^{(3)}] = 1 \cdot 10^{-10}$ esu, $\mathrm{Im}[\bar{\chi}^{(3)}] = -0.8 \cdot 10^{-10}$ esu, for $\lambda = 540$ nm, and $\mathrm{Re}[\bar{\chi}^{(3)}] = -3.5 \cdot 10^{-11}$ esu, $\mathrm{Im}[\bar{\chi}^{(3)}] = -2.7 \cdot 10^{-11}$, for $\lambda = 1079$ nm. This means that the saturation of absorption and the nonlinear refraction provide comparable contributions to the nonlinearity. Note that the real part changes its sign with the wavelength. The measured enhancement factors are comparable with the calculated values of G'_K and G''_K with the accuracy approximately 1 order of magnitude.

Using a different technique based on a dispersion interferometer, the nonlinear correction to the refractive index, n_2, was also measured for $\lambda = 1064$ nm (at $p = 5 \cdot 10^{-6}$

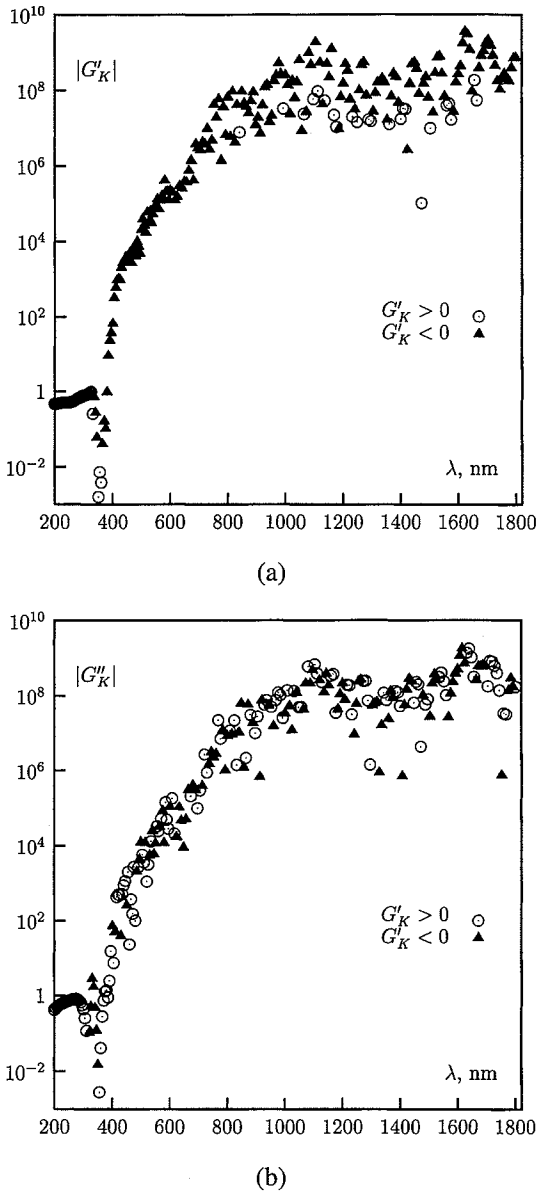

Fig. 8. Enhancements on silver CCAs for the real, G'_K, (a) and imaginary, G''_K, (b) parts of the Kerr-type optical nonlinearity and for four-wave mixing, G_{FWM}, process (c). (Source: Reprinted with permission from V. M. Shalaev, E. Y. Poliakov, and V. A. Markel, *Phys. Rev. B* 53, 2437 [1996]. © 1996 American Physical Society.)

and low intensity). The obtained value is $n_2 = -1.5 \cdot 10^{-11}$ cm^2/W that corresponds to $\mathrm{Re}[\bar{\chi}^{(3)}] \approx -7 \cdot 10^{-10}$ esu [30].

Note that fractal aggregates of colloidal particles can be placed into a polymer matrix (like gel). Then, thin films can be prepared with fractal aggregates in such matrices. The volume fraction filled by metal fractal aggregates in such thin films is typically larger than in the case of colloidal solution and therefore the nonlinearities are significantly higher [29].

A laser pulse duration used in the previous experiments was ~10 ns. The Kerr-type third-order nonlinearity was also detected with the use of 30 ps laser pulses. However, the obtained optical nonlinearities were in this case significantly smaller than in the ex-

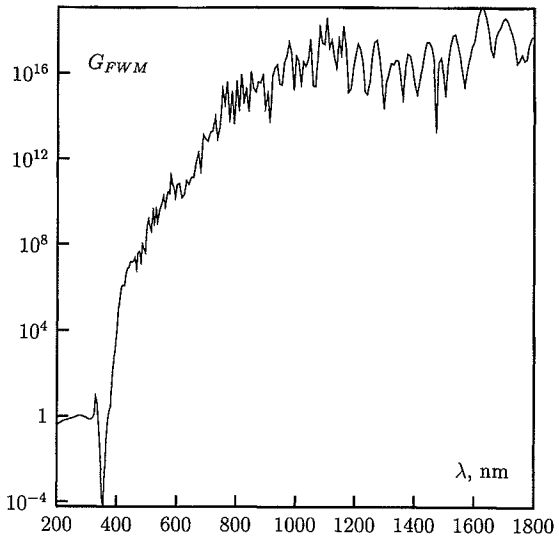

(c)

Fig. 8. (*Continued.*)

periments with nanosecond laser pulses. Our studies indicate that there are probably two different types of the optical nonlinearities, $\bar{\chi}^{(3)}$. The smaller one has the time of nonlinear response in the picosecond scale and the larger one has the time of nonlinear response in the nanosecond scale. The first of them can be associated with thermalization of the photoexcited hot electron gas of metal particles in an aggregate through electron-phonon coupling [32], whereas the second one probably involves effects connected with the heating of the crystal lattice of the metal.

Of particular interest for nonlinear optics are composites of particles with a high intrinsic nonlinearity and metal fractal aggregates that can provide a significant enhancement of the local fields. A high efficiency of the four-wave mixing in films of J-aggregates of pseudo-isocyanine in a polymer matrix was observed [34]. A $30\times$ increase in the nonlinear susceptibility of a film under doping of gold colloidal aggregates in a composite was observed. Very high optical susceptibilities, $|\bar{\chi}^{(3)}| \approx 10^{-6}$ esu with a subpicosecond response time were achieved.

The authors of [35] reported observation of a 200-fold enhancement in the third-order optical coefficient of a polydiacetylene doped by gold clusters with respect to that of a pure polymer. The increasing of the quadratic electro-optic coefficient of a polymethylmethacrylate due to the doping by silver aggregates was also reported [36].

The surface-enhanced second-order optical nonlinearity was found in [37]. A $10^2\times$ increase was observed in the second-harmonic intensity in silver particles aggregated into clusters.

Thus, the preceding experiments give evidence to enhancement of nonlinear coefficients in the fractal-structured aggregated colloids in comparison with nonaggregated ones. There is a qualitative agreement between the theory and the experiments. We mention that enhanced optical nonlinearities were also obtained in nonfractal composite materials [38].

3.5. Selective Photomodification of Fractal Aggregates

The previous high nonlinearities in aggregates of silver colloidal particles were obtained at the laser intensity $I \leqslant 1.5$ MW/cm^2. At higher intensities the light-induced modification (selective in frequency and polarization) occurs resulting in local restructuring of

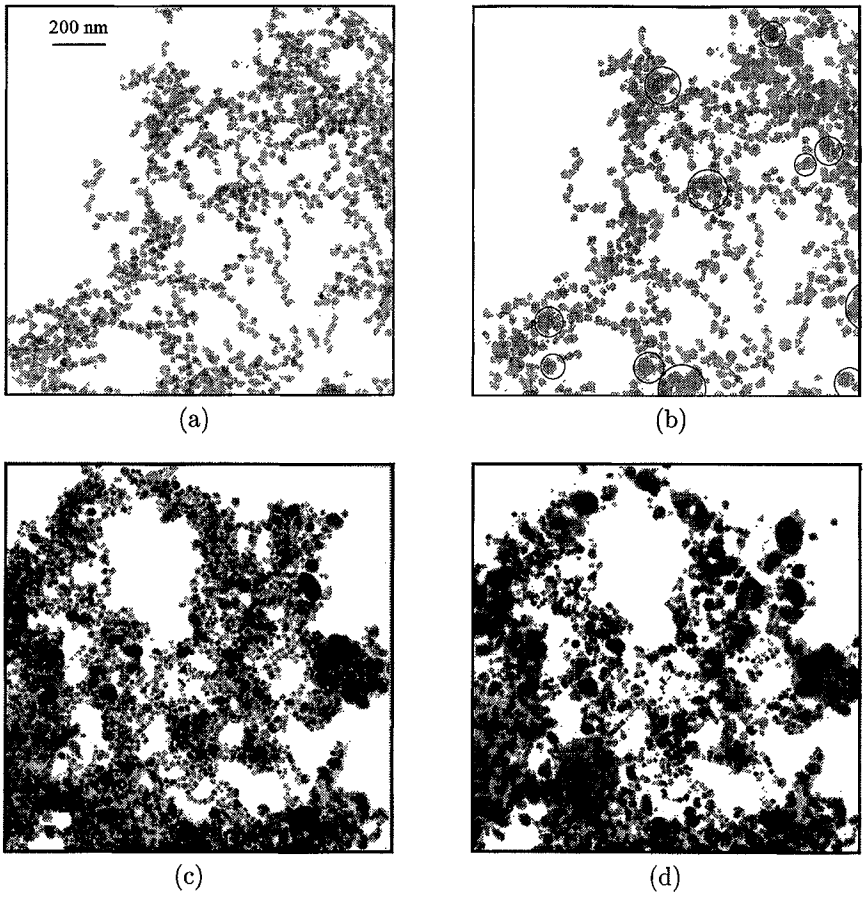

Fig. 9. Electron micrographs of silver colloid aggregates before (a, c) and after (b, d) irradiation by laser pulses at $\lambda_L = 1079$ nm, and the energy of a laser pulse per unit area $W = 11$ mJ/cm^2 (b), and $\lambda_L = 450$ nm, $W = 20$ mJ/cm^2 (d). The circles in Figure 1b are an aid to the eye. (Source: Reprinted with permission from [40]. © 1998 American Physical Society.)

resonant domains in the irradiated cluster. This modification can be also observed in a pulsed laser regime when the pulse energy per unit area, W, is higher than a certain threshold, W_{th}. Electron micrographs of colloidal silver aggregates before and after irradiation by a sequence of laser pulses at two different wavelengths are shown in Figure 9 [40]. Comparison of the micrographs of the cluster before and after irradiation at the laser wavelength $\lambda_L = 1079$ nm (Fig. 9a and b, respectively) shows that the structure of the cluster as a whole remained the same after the irradiation, but monomers within small nm-sized domains change their size, shape, and local arrangement. The minimum number of monomers in the region of modification is 2–3 at $\lambda_L = 1079$ nm. Thus, the resonance domain at $\lambda_L = 1079$ nm can be as small as $\lambda_L/25$. Although there are fluctuations in both shape and size of the modified domains, Figure 9b reveals that hot zones associated with resonant excitation are highly localized, in accordance with the theoretical predictions [10, 12]. When the laser wavelength is close to the isolated monomer absorption peak, $\lambda_L = 450$ nm (Fig. 9c and d), localization of optical excitations is much weaker. We estimate that about 70% of all monomers are photomodified at $\lambda_L = 450$ (see Fig. 3d), while only about 10% of monomers were modified at $\lambda_L = 1079$ nm. Note that the ratio W/W_{th} was approximately the same in both cases. The increase of localization of optical excitations in fractals toward longer wavelengths (relatively to the monomer absorption peak was predicted theoretically in [10].

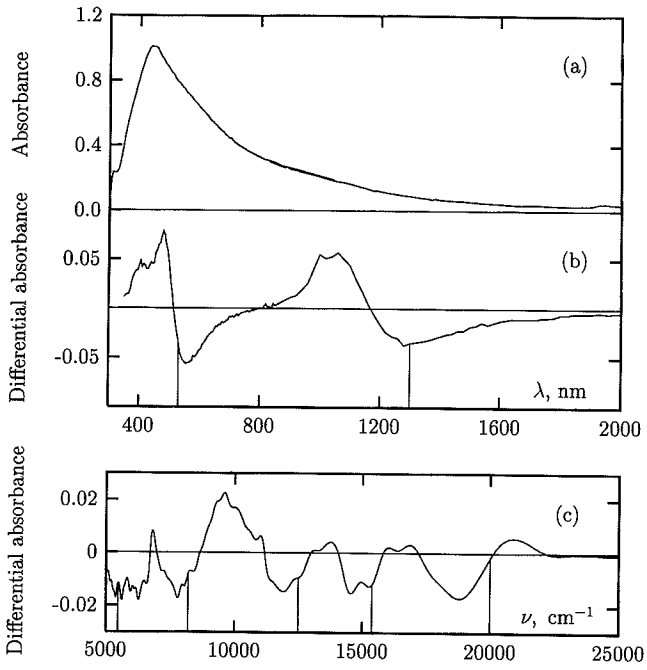

Fig. 10. (a) Absorption spectrum of silver aggregates in a gelatin film. (b) Difference in the absorbance of the silver-gelatin film before and after irradiation by pulses at $\lambda_L = 532$ nm, $W = 24$ mJ/cm^2 and at $\lambda_L = 1300$ nm, $W = 11$ mJ/cm^2. (c) An example of five spectral holes recorded at the same area. The vertical bars denote laser frequencies. $W/W_{th} = 1.1$–1.3; the number of pulses increases from 5 in the visible to 30 in the IR range to obtain the holes of the same depth. (Source: Reprinted with permission from [40]. © 1998 American Physical Society.)

The photomodification leads, in turn, to a spectral hole in the aggregate absorption spectrum in the vicinity of the laser wavelength [4, 39]. An example of spectral hole burning is shown in Figure 10 [40]. The dependence of the hole depth on laser intensity demonstrates a threshold character of the photomodification process [4]. Therefore, one can find a contribution of the resonant domains (hot spots) to the enhanced nonlinearities by measuring the nonlinear responses before and after photomodification. Corresponding experiments show an evidence of considerable decreasing of the four-wave mixing signal, nonlinear absorption and refraction when the photoburning occurs [29, 30]. This decreasing is illustrated in Figure 11 for the case of the nonlinear refraction [30]. [The increase in $-\Delta n$ after it drops down is due to the persistent holographic grating recorded in a colloidal solution at high intensities; this results in an additional contribution to the measured signal [30].]

Further insight concerning the interaction of metal fractal clusters with light can be obtained from the spectral dependence of the energy absorbed per unit volume, P, in the layer where photomodification occurs. This series of experiments was performed at a laser pulse energy near threshold (defined by the requirement of a fixed spectral hole depth, $\Delta\alpha/\alpha_{\mathrm{abs},0} = 10^{-2}$ after irradiation by 10 laser pulses). In this case, the spectral dependence of Q is given by $P(\lambda_L) \approx \alpha_{\mathrm{abs},0}(\lambda_L) W_{th}(\lambda_L)$. Figure 11 shows that P significantly decreases as λ_L varies from 355 to 2000 nm [40].

To complement the experimental observations, we also performed numerical calculations for the fraction of most absorbing resonant monomers, n_r, contributing 50% to the total absorption [40]. (We assume that the resonant monomers contribute up to 50% to the total absorption, with the rest being due to nonresonant particles; this conclusion is supported by the fact that the largest spectral holes observed in our experiments contribute about half the initial absorption.) Because photomodification occurs in the most absorbing monomers it is plausible to assume that $W_{th} \propto n_r$. To compare with the experimental data

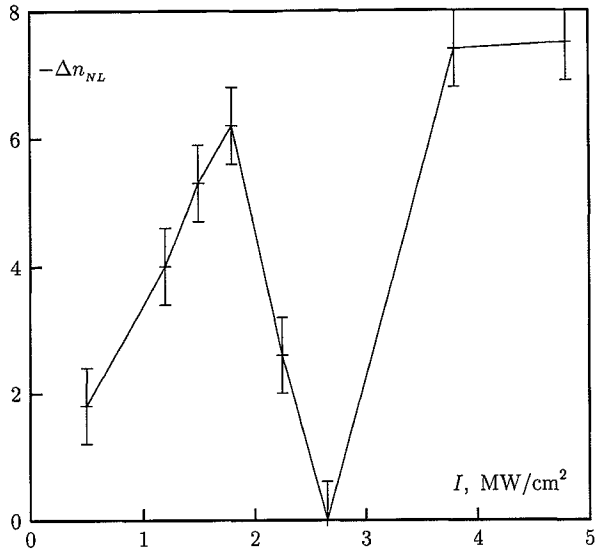

Fig. 11. Dependence of the nonlinear addition to the refractive index of aggregated silver colloid on laser intensity, $\Delta n_{NL} = [n(\omega) - n_0] \cdot 10^5$. (Source: Adapted from [30].)

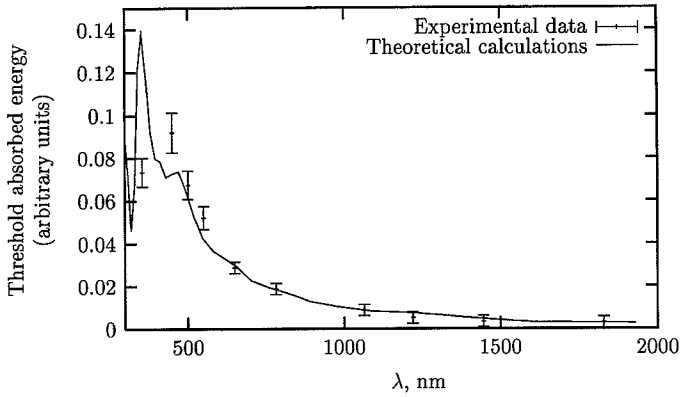

Fig. 12. Spectral dependence of the threshold absorbed energy per unit volume, $\alpha_{\text{abs},0} W_{th}$ (see the text for details). (Source: Reprinted with permission from [40]. © 1998 American Physical Society.)

for $\alpha_{\text{abs},0} W_{th}$, we plot in Figure 12 (solid line) results of our theoretical calculations for the product $\alpha_{\text{abs},0} n_r$ [40].

As seen in Figure 12, the theoretical calculations agree well with the experimental observations for almost all wavelengths (poor agreement at the range $\lambda \sim 400$ nm is probably because of the presence in a sample of some amount of nonaggregated particles). According to the results obtained, for λ close to the monomer absorption peak (~450 nm), the absorption is almost equally distributed over all monomers in a cluster (cf., Fig. 9d); the absorption, however, becomes progressively more localized as λ increases toward the infrared region, and for $\lambda \approx 2\mu$m, only about 5% of monomers provide 50% of the total absorption (cf., Fig. 9b). This means that at longer wavelengths there are small resonance domains in a fractal that account for a large fraction of the total absorption. Consequently, the threshold photomodification energy tends to decrease with λ. This can be interpreted as an effective "focusing" of the incident light in resonance domains whose size is much smaller than λ.

Now we briefly discuss a possible mechanism for the observed photomodification. We made an estimate of the laser heating of silver nanospheres in gelatin for an exponential pulse shape. We used the adiabatic approximation (i.e., the pulse duration was assumed to be much larger than all characteristic times of the system) and we neglected the temperature dependence of all thermodynamic constants. From the thermal conductivity equation for an isolated spherical silver nanoparticle in gelatin, with the heat source homogeneously distributed inside the particle, we estimate the increase in the particle temperature as

$$T_p - T_0 \approx 3\sigma W\{4\pi R^3 c_1 \varrho_1[1+\sqrt{\Gamma t_p}(\sqrt{\Gamma t_p}+a)]\}^{-1}$$

where $a = \sqrt{3c_2\varrho_2/c_1\varrho_1}$, $\Gamma = \kappa_2/c_1\varrho_1 R^2$, c_1, c_2 and ϱ_1, ϱ_2 are the specific heats and mass densities of silver and gelatin, κ_2 is the thermal conductivity of gelatin, R is the radius of silver particles, σ is the absorption cross section per monomer, t_p is the pulse duration, and $T_0 = 300$ K is the initial temperature. With the known values of the thermodynamic constants, and the measured absorption cross-section, the previous formula yields $T_p \approx 600$ K at the threshold energy $W_{th} = 10$ mJ/cm^2 for $\lambda_L = 550$ nm.

According to [41], sintering of metal nanoparticles starts as early as the temperature exceeds half the melting point T_m (for Ag, $T_m \approx 1200$ K), and the characteristic time of this process is 100 ps. Thus, the preceding temperature T_p is sufficient to start the process of sintering in silver colloids at the threshold pulse energy W_{th}. Note that enlargement of Ag nanoparticles by approximately a factor of 2 was also observed in island Ag films after thermal heating to 570 K [42].

To conclude, the spectral dependence of selective photomodification of fractal colloidal aggregates shows that in accordance with theoretical predictions, the number of monomers strongly interacting with the incident light decreases substantially toward the IR. The localization of optical excitations in fractal clusters permits the optical recording of data on nm scales.

3.6. Discussion

As shown earlier, the clustering of small particles embedded in a host material may result in a giant enhancement of both linear (e.g., Rayleigh and Raman scattering) and nonlinear (four-wave mixing, harmonic generation, and nonlinear reflection and absorption) optical effects. The enhancement occurs because of strongly fluctuating local fields that can have very large values in particle aggregates (see Fig. 5). Nonlinearities emphasize these fluctuations, leading to giant enhancements.

If particles aggregate into fractal clusters, fluctuations of the local fields are especially large (see Fig. 5). This is because the dipole interactions in fractals are not long range (as they are in conventional three-dimensional media) and many of the collective eigenmodes are localized in different parts of a cluster with various random structures. This ultimately leads to strong spatial fluctuations of the fields. In contrast, in compact three-dimensional clusters of particles, the long-range dipolar interaction involves all particles into the excitation of eigenmodes, thereby suppressing the fluctuations (see Fig. 5).

Enhancement in small-particle clusters can be understood and roughly estimated using the following simple arguments. Consider the enhancement for an arbitrary nonlinear optical process $\propto E^n$. As discussed earlier, for the resonant dipolar eigenmodes in fractals, local fields, E_i, exceed the external field, $E^{(0)}$, by the factor $\sim|\alpha_0^{-1}/\delta| = |X + i\delta|/\delta$ (see (15)–(17)), that is, $\sim|X|/\delta$ for $|X| \gg \delta$. However, the fraction of the monomers involved in the resonant optical excitation is small, $\sim\delta\,\mathrm{Im}\,\alpha(X)$.

For a nonlinear optical process, $\propto |E|^n$, one can estimate the ensemble average of the enhancement, $\langle|E_i/E^{(0)}|^n\rangle$, as the resonant value, $|E_i/E^{(0)}|^n_{\mathrm{res}}$, multiplied by the fraction of the resonant modes (in other words, the fraction of particles involved in the resonant

excitation). This gives the following estimate for the enhancement,

$$\left\langle \left| \frac{E_i}{E^{(0)}} \right|^n \right\rangle \sim |X|^n \delta^{-n} \times \delta \operatorname{Im}\alpha(X) \sim |X|^n \delta^{1-n} \operatorname{Im}\alpha(X) \tag{25}$$

which is $\gg 1$ for $n > 1$. Because this is only a rough estimation, an adjustable constant, C, should be, in general, added as a prefactor.

The nonlinear dipole amplitude can be enhanced along with the linear local fields provided the generated frequency lies within the spectral region of the cluster eigenmodes. For enhancements of incoherent processes, such as Raman scattering and nonlinear refraction and absorption in Kerr media, we obtain from Eq. (25): $G \sim CX^4\delta^{-3} \operatorname{Im}\alpha(X)$. For coherent processes, the resultant enhancement $\sim|\langle|E_i/E^{(0)}|^n\rangle|^2$; accordingly, the enhancement factor $\sim CX^6\delta^{-4}[\operatorname{Im}\alpha(X)]^2$ for the third harmonic generation, and $\sim CX^8\delta^{-6}[\operatorname{Im}\alpha(X)]^2$ for degenerate four-wave mixing. (The latter enhancement is larger because of the "additional" enhancement of the generated nonlinear amplitudes oscillating at the same frequency as the applied field.) All these estimates are in good agreement with numerical calculations of [5].

There are other optical phenomena (not considered here) that can also be enhanced in small-particle composites. For example, fluorescence (from molecules adsorbed on a small-particle aggregate) following the two photon absorbtion by the aggregate is enchanced by the factor: $G_F \sim \langle|E_i/E^{(0)}|^4\rangle \sim |\alpha_0|^{-4}\langle|\alpha_i|^4\rangle \propto \delta^{-3}$.

In conclusion of this section, the fractal morphology of small-particle aggregates results in very strong local fields associated with localized optical modes in fractals; the large and strongly fluctuating local fields lead to giant enhancement of optical phenomena in fractal aggregates.

In the following text we consider surface-enhanced optical processes in another class of fractal nanostructured materials which are self-affine thin films.

4. SELF-AFFINE THIN FILMS

4.1. General Approach

In the following text we consider results of studies of linear and nonlinear optical properties of self-affine thin films. Rough thin films, formed when an atomic beam condenses onto a low-temperature substrate, are typically self-affine fractal structures [9]. Contrary to the case of "usual" roughness, there is no correlation length for self-affine surfaces, which implies that inhomogeneities of all sizes are present (within a certain size interval) according to a power-law distribution. Self-affine surfaces obtained in the process of the film growth belong to the Kardar–Parisi–Zhang universality class.

Although self-affine structures differ from self-similar fractal objects (to reveal the scale invariance they require two different scaling factors in the surface plane and in the normal direction), optical properties of self-affine thin films are, in many respects, similar to those of fractal aggregates [6]. For example, both fractal aggregates and self-affine films possess a variety of dipolar eigenmodes distributed over a wide spectral range [2, 6]. In contrast, for the case of conventional (nonfractal) random ensembles of monomers, such as a gas of particles or randomly close-packed spheres, the absorption spectra are peaked near a relatively narrow resonance of an individual particle. In fractals, a variety of dipolar eigenmodes can be excited by a homogeneous electric field, whereas only one dipolar eigenmode can be excited in a small dielectric sphere [43]. These striking differences are explained by localization of optical modes in various random, spatially separated, parts of a fractal object [2, 10].

In random but homogeneous, on average, media, dipolar modes (polaritons) are, typically, delocalized over large spatial areas. All monomers absorb light energy with approximately equal rate in the regions whose linear dimensions significantly exceed the incident

field wavelength. This is, however, not the case for fractal nanocomposites and self-affine films. Optical excitations in these fractal objects tend to be localized [2, 10]. Because of this localization, and because there is a large number of different local geometrical structures in fractals that resonate at different frequencies, the fractal optical modes cover a large spectral interval.

Most rough surfaces are self-affine within a certain interval of sizes and, therefore, their optical properties are typical for fractals. Because the field distributions are extremely inhomogeneous at the rough surfaces of thin films, there are "cold" regions of small local fields and "hot" areas of high local fields. Strong enhancements of a number of optical phenomena in rough metal films are associated with much higher values of local fields in the hot spots of a rough film [2, 11].

To simulate a self-affine film, we used the restricted solid-on-solid (RSS) model (for details see Ref. [44] and references therein). In this model, a particle is incorporated into the growing aggregate only if the newly created interface does not have steps which are higher than one lattice unit, a. The surface structure of such deposits is relatively simple, because there are no overhangs. In this way strong corrections to scaling effects are eliminated and the true scaling behavior appears clearly, even for small dimensions. In the long-time regime, the height–height correlation function for a self-affine surface has the form,

$$\left\langle \left[h(\mathbf{r}) - h(\mathbf{r}+\mathbf{R}) \right]^2 \right\rangle \sim R^{2H} \tag{26}$$

where $\mathbf{R}$ is the radius vector in the plane normal to the growth direction, z, and the scaling exponent (codimension), H, is related to the fractal dimension, D, through the formula $H = 3 - D$. For the RSS model, $D = 2.6$ and the scaling formula presented earlier is valid for large values of the average height, $\bar{h}$, (which is proportional to the deposition time), such that $\bar{h} \gg l^{\zeta}$, where $\zeta = 2(d+1)/(d+2) = 2 - H$; here, l is the linear size of a system and d is the dimension of the embedding space. Our simulations satisfied this condition, and the foregoing scaling relation was well manifested.

In the simulations, we removed the bulk (regular) part of the computer-generated film so that the resultant sample had, at least, one hole. Clearly, the removal of the bulk part of a film does not affect the scaling condition (26). A typical simulated self-affine film is shown in Figure 13.

Unlike for "conventional" random surfaces, the contribution of higher spatial harmonics (with amplitudes larger than the harmonic wavelengths) plays an important role in the

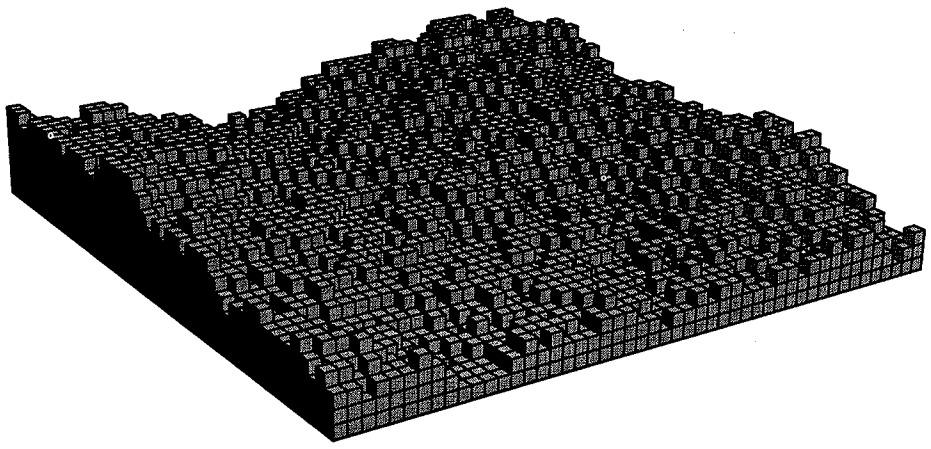

Fig. 13. Self-affine film obtained in the restricted solid-on-solid model. The scaling exponent $H = 0.4$ and the fractal dimension $D = 3 - H = 2.6$. (Source: Reprinted with permission from V. M. Shalaev, R. Botet, J. Mercer, and E. B. Stechel, *Phys. Rev. B* 54, 8235 [1996]. © 1996 American Physical Society.)

Fourier expansion of a self-affine surface profile. This means that neither the Rayleigh perturbation approximation [45] nor the Kirchoff (geometrical optics) approach can be directly applied to describe optical properties of self-affine structures [48]. Apart from these two basic approaches, there exists a phase perturbation method [49, 50], which is intermediate between the former two methods, and cannot be applied to self-affine surfaces either.

Our approach is based on the discrete dipole approximation (DDA) [6]. As mentioned in the previous section, the DDA was originally suggested by Purcell and Pennypacker [24] and was developed in later articles [25] and [51–53] to calculate optical responses from an object of an arbitrary shape. It is based on replacing an original dielectric medium by an array of pointlike elementary dipoles. The DDA has been also applied to fractal clusters built from a large number of small interacting monomers [2, 10, 54, 55] (see Section 3). We briefly recapitulate the DDA and the related method based on solving the coupled-dipole equations [2, 6, 10].

Following the main idea of the DDA, we model self-affine films by point dipoles placed according to an algorithm described in the following text in sites of a simple cubic lattice with a period a, which is assumed to be much smaller than the size of spatial inhomogeneities. The occupied sites correspond to the spatial regions filled by the film, while empty sites correspond to the empty space. The linear polarizability of an elementary dipole (monomer), α_0, is given by the Lorenz–Lorentz formula having the same form as the polarizability of a dielectric sphere with radius $R_m = (3/4\pi)^{1/3}a$ (see, for example, [16]),

$$\alpha_0 = R_m^3 \frac{\varepsilon - 1}{\varepsilon + 2} \tag{27}$$

where as earlier $\varepsilon = \varepsilon' + i\varepsilon''$ is the bulk dielectric permittivity of the film material (note that (27) coincides with (10), if $\varepsilon_h = 1$). The choice of the sphere radius, R_m, provides equality of the cubic lattice elementary cell volume (a^3) and the volume of an imaginary sphere (monomer) that represents a pointlike dipole ($4\pi R_m^3/3$) [24, 25, 52]. Consequently, for large films consisting of many elementary dipoles, the volume of the film is equal to the total volume of the imaginary spheres. Note that the neighboring spheres intersect geometrically because $a < 2R_m$. Using the intersecting spheres allows one, to some extent, to take into account the effects of the multipolar interaction within the pure dipole approximation [2, 6, 24, 25, 52] (cf., Section 3). We also note that using the DDA allows us to treat a film as a cluster of polarizable monomers that interact with each other via the light-induced dipoles which makes this problem similar to the problem of fractal aggregates considered previously in Section 3.

4.2. Linear Optical Properties

Being given the coordinates of all dipoles in a self-affine film we can find its optical eigenmodes, the local fields, and the film polarizability, in the same way it was done for small-particle aggregates (see (15)–(18)). In Figure 14, we show plots for the imaginary parts (describing absorption) of the "parallel" and "perpendicular" components of the mean polarizability per particle, $\alpha_\parallel \equiv (1/2)\langle \alpha_{i,xx} + \alpha_{i,yy} \rangle$ and $\alpha_\perp \equiv \langle \alpha_{i,zz} \rangle$. The parallel component, $\alpha_\parallel$, characterizes the polarizability of a self-affine film in the (x, y)-plane, whereas the perpendicular component, $\alpha_\perp$, gives the polarizability in the normal, z, direction. The polarizability components satisfy the sum rule: $\int \alpha_{\perp,\parallel}(X)\, dX = \pi$ (see (20)).

From the figure it is clear that there is a strong dichroism expressed in the difference between the two spectra, $\alpha_\parallel(X)$ and $\alpha_\perp(X)$. The modes contributing most to $\alpha_\parallel$ (the "longitudinal" modes) are located in the long wavelength part of the spectrum (negative X; cf. (11)), whereas the "transverse" modes tend to occupy the short wavelength part of the spectrum (positive X). To some extent, this can be understood by roughly considering a film as an oblate spheroid, where the longitudinal and transverse modes are shifted to the red and blue, respectively, in comparison with the eigenmode of a sphere. However, in contrast to the case of a spheroid, there is a large variety of eigenmodes in self-affine films, as

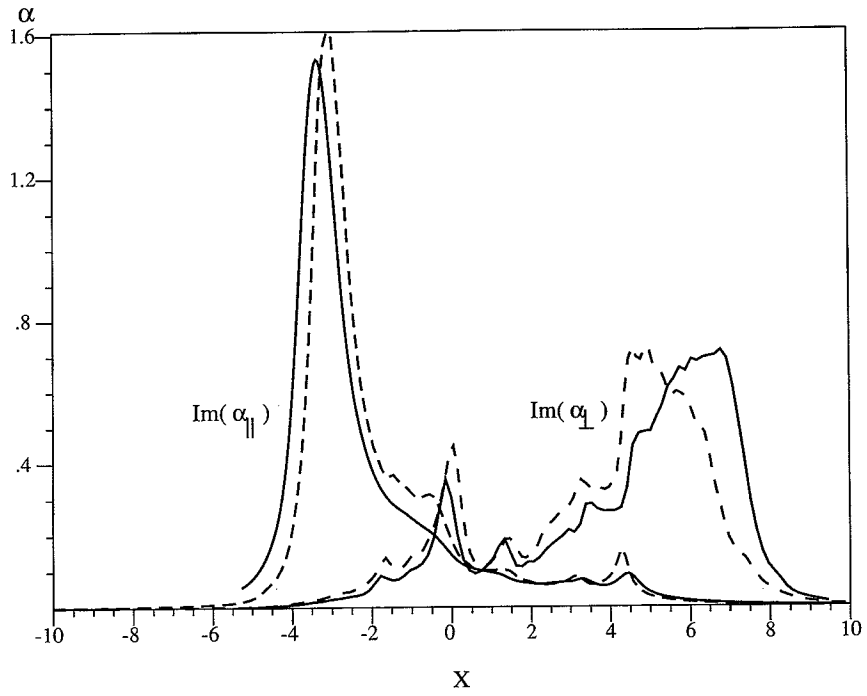

Fig. 14. The imaginary parts of the parallel, $\alpha_{\parallel}$, and the perpendicular, $\alpha_{\perp}$, components of the polarizability. The results for samples with $N \sim 10^4$ and $N \sim 10^3$ dipoles each (solid and dashed lines, respectively) are shown. (Source: Reprinted with permission from V. M. Shalaev, R. Botet, J. Mercer, and E. B. Stechel, *Phys. Rev. B* 54, 8235 [1996]. © 1996 American Physical Society.)

follows from Figure 14. Really, the widths of the spectra in Figure 14 are much larger than the width of an individual resonance, δ; this indicates a strong inhomogeneous broadening associated with a variety of the dipolar eigenmodes on a self-affine surface. Thus, the dipole–dipole interactions of constituent monomers in a self-affine film generate a wide spectral range of resonant modes, similar as it was in the case of fractal aggregates.

From Figure 14, we also make an important conclusion that in the quasi-static approximation, the optical properties of a self-affine film do not depend on the number of monomers, N, and, therefore, on the linear size, l, of the film. The calculations that were performed for the ensembles of samples with very different numbers of particles and linear sizes give similar results. Note also that the fact that the spectra are almost independent of the number of the dipoles, N, justifies the used discrete dipole approximation.

The field distributions of eigenmodes on a self-affine surface are extremely inhomogeneous. On such a surface, there are hot spots associated with areas of high local fields, and cold zones with small local fields. (A similar patchworklike picture of the field distribution is observed in fractal clusters [2, 3, 10, 31, 56].) Spatial locations of the modes are very sensitive to both frequency and polarization of the applied field.

To demonstrate this, in Figure 15, we show the intensity distributions for the local fields, $|\mathbf{E}(\mathbf{R}_i)|^2$, on the film-air interface [$E_{i,\alpha} \equiv E_\alpha(\mathbf{R}_i) = \alpha_0^{-1} d_{i,\alpha}$, where $d_{i,\alpha}$ are defined in (15)–(17), and $\mathbf{R}_i \equiv (x_i, y_i)$, with x_i and y_i being the coordinates of the dipoles on the surface of a film]. The results are shown for different values of frequency parameter, X. Note that the local-field distributions, $|\mathbf{E}(\mathbf{R}_i)|^2$, can be measured with the use of a near-field scanning optical microscope, provided the probe is passive [57].

As seen in Figure 15, for a modest value of $\delta = 0.03$, which is typical for metals in the visible and near-infrared parts of the spectrum, the local-field intensities in the hot zones can significantly, up to 3 orders of magnitude, exceed the intensity of the applied field

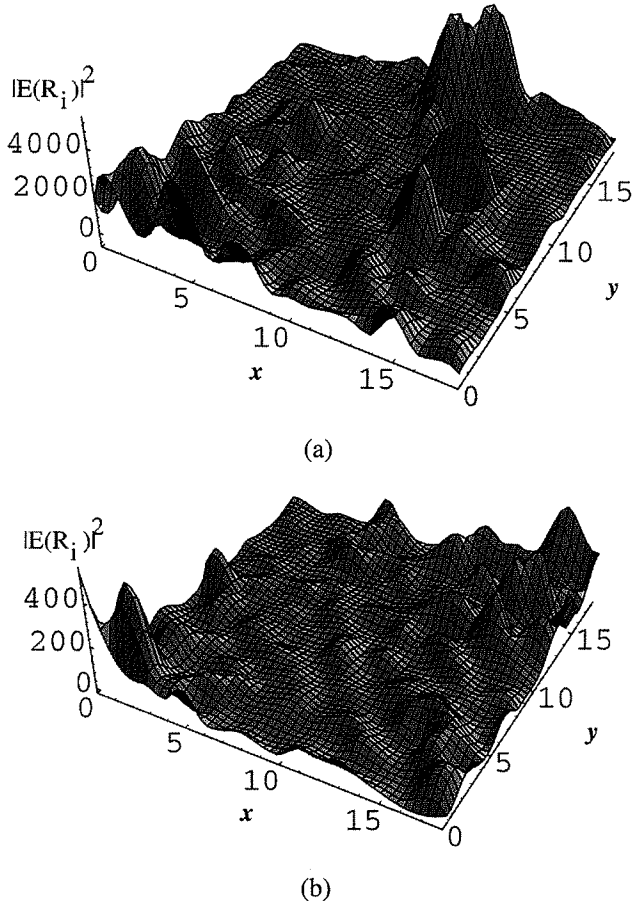

Fig. 15. Spatial distributions of the local-field intensities, $|\mathbf{E}(\mathbf{R}_i)|^2$, on the self-affine surface for different values of frequency parameter, X. (a) $X = -3$ ($\lambda = 500$ nm, (b) $X = -2$ ($\lambda = 400$ nm). The decay parameter $\delta = 0.03$ in both cases. The applied field is polarized in the (x, y)-plane, $\mathbf{E}^{(0)} = (2)^{-1/2}(1, 1, 0)$. (Source: Reprinted with permission from V. M. Shalaev, R. Botet, J. Mercer, and E. B. Stechel, *Phys. Rev. B* 54, 8235 [1996]. © 1996 American Physical Society.)

(for smaller values of δ, the enhancements can be even larger). The high frequency and polarization sensitivity of the field distributions are also obvious from the figure.

Strongly inhomogeneous distributions of local fields on a self-affine surface bring about large spatial fluctuations of local fields and strong enhancements of optical processes. These enhancements are especially large for nonlinear optical phenomena which are proportional to the local fields raised to some high power.

To study localization of eigenmodes on a self-affine surface, we calculated the mode pair-correlation function defined as

$$\nu_n(R, X) = \left\langle C \sum_{i,j \in s;\alpha,\beta} \delta(R_{ij} - R)\left[(i\alpha|n)\right]^2\left[(j\beta|n)\right]^2 \right\rangle \tag{28}$$

where the normalization constant C is defined by the requirement $\nu(R = 0) = 1$, and the summations are over dipoles on the surface only. If the mode is localized within a certain area of radius R_0, then $\nu(R)$ is small for $R > R_0$ and the rate of decay of $\nu(R)$ at $R > R_0$ reflects a character of localization (strong or weak) for the state n [58].

The calculated $\nu(R, X)$ (see Fig. 16) are well approximated by the formula $\nu(R, X) = \exp\{-[R/L(X)]^\kappa\}$, where $\kappa \approx 0.7$. When the exponent is larger than 1, $\kappa > 1$, the modes

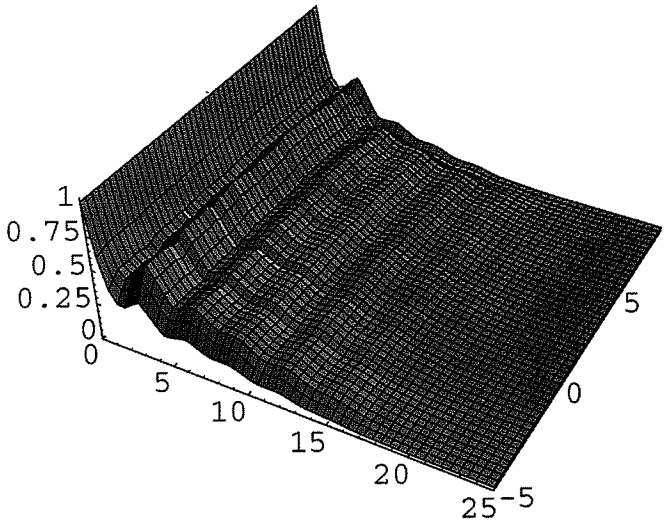

Fig. 16. The mode correlation function, $\nu(R, X)$. (Source: Reprinted with permission from V. M. Shalaev, R. Botet, J. Mercer, and E. B. Stechel, *Phys. Rev. B* 54, 8235 [1996]. © 1996 American Physical Society.)

are commonly called superlocalized; in our case, with $\kappa \approx 0.7$, the modes can be referred to as sublocalized (or quasi-localized), on average.

4.3. Enhanced Optical Phenomena on a Self-Affine Surface

Calculating the local fields with (15) and (16) and substituting them to the general formulas of Section 2, we find enhancement factors for different optical phenomena.

In Figure 17, we show results of our theoretical calculations for the average enhancement of Raman scattering for both small and large Stokes shifts on self-affine films generated in the RSS model. $G_{RS,\parallel}$ and $G_{RS,\perp}$ describe enhancements for the applied field polarized in the plane of the film and perpendicular to it, respectively, (see (3)). As seen in the figure, the enhancement increases toward the long-wavelength part of the spectrum and it reaches very large values, $\sim 10^7$. This agrees well with the experimental observations of SERS on cold-deposited thin films [11].

In Figure 18, the field spatial distributions at the fundamental and Stokes frequencies are shown. As seen in the figure, the distributions contain hot spots, where the fields are very high. Although the Stokes signal is proportional to the local field at the fundamental frequency, ω, the generated Stokes field, with frequency ω_s, excites, in general, other eigenmodes. Hence the field spatial distributions produced by the applied field and by the Raman signal can be different, as clearly seen in the figure.

This pattern is expected to be typical for various optical processes in strongly disordered fractal systems, such as self-affine thin films. Specifically, hot spots associated with fields at different frequencies and polarizations can be localized in spatially separated nm-sized areas. These novel nano-optical effects can be probed with NSOM providing subwavelength resolution [3, 31, 57].

If molecules possess the second-order nonlinear susceptibility, $\chi^{(2)}$, then second harmonic generation (SHG) can be strongly enhanced when adsorbing the molecules on a metal self-affine surface (see (4)). In Figure 19, we plot the calculated enhancement for SHG from molecules on a silver self-affine surface (for the applied field polarized parallel and perpendicular to the surface, $G_{\mathrm{SHG},\parallel}$ and $G_{\mathrm{SHG},\perp}$, respectively). As seen in the figure, the enhancement is very large and increases toward larger wavelengths.

We see that the anticipated inequality $G_\parallel \gg G_\perp$ holds, because the linear dipoles and corresponding local fields (17) are, on average, larger for the incident field polarized in the

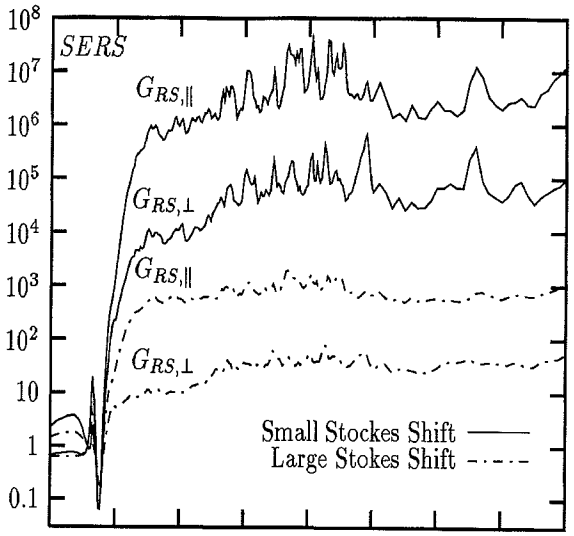

Fig. 17. Enhancement factor for Raman scattering, $G_{RS,\parallel} = [G_{RS,x} + G_{RS,y}]/2$ and $G_{RS,\perp} = G_{RS,z}$, on silver self-affine films for small and large Stokes shifts. (Source: Reprinted with permission from E. Y. Poliakov, V. M. Shalaev, V. A. Markel, and R. Botet, *Opt. Lett.* 21, 1628 [1996]. © 1996 American Institute of Physics.)

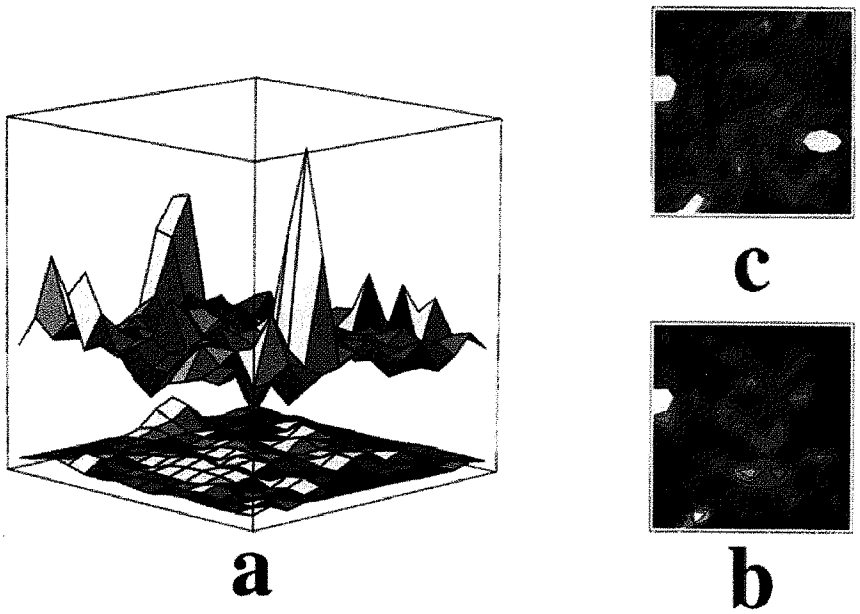

Fig. 18. Spatial distributions for the local fields at the fundamental frequency, $\lambda = 550$ nm, (bottom; the field distribution is magnified by 3) and for the Stokes fields, $\lambda_s = 600$ nm, (top). [The applied field is linearly polarized in the plane of the film.] (b) and (c) The contour plots for the field distributions shown on (a). (Source: Reprinted with permission from E. Y. Poliakov, V. M. Shalaev, V. A. Markel, and R. Botet, *Opt. Lett.* 21, 1628 [1996]. © 1996 American Institute of Physics.)

plane of the film than in the normal direction; this is because a thin film can be roughly thought as an oblate spheroid with a high aspect ratio. The largest average enhancement for SHG is $\sim 10^7$.

In Figure 20, we show the enhancement factor for THG, G_{THG}, calculated using formula (5) with $n = 3$. The values of G_{THG} are even larger than for G_{SHG}, reaching $\sim 10^{11}$ values.

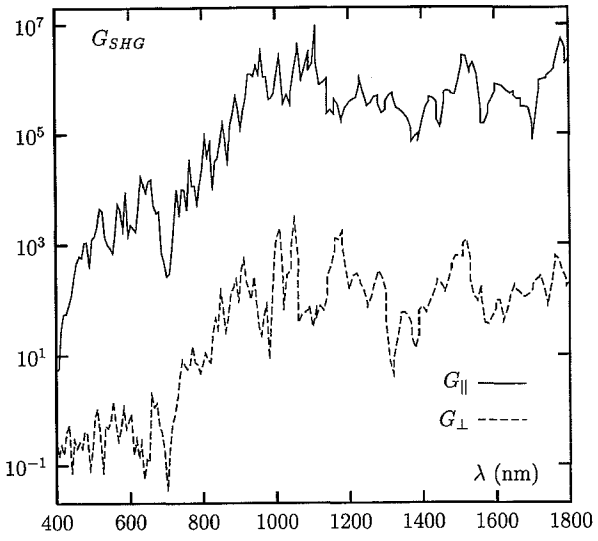

Fig. 19. Average enhancement factors for second harmonic generation (SHG) from a self-affine silver surface, for the light polarized in the (x, y)-plane of the film ($G_{\text{SHG}} \equiv G_{\|}$) and in the normal z-direction ($G_{\text{SHG}} \equiv G_{\perp}$). (Source: Reprinted with permission from E. Y. Poliakov, V. A. Markel, V. M. Shalaev, and R. Botet, *Phys. Rev. B* 57, 14901 [1998]. © 1998 American Physical Society.)

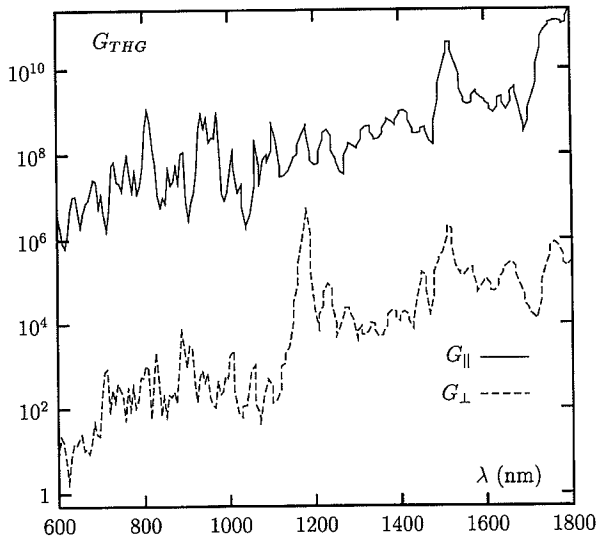

Fig. 20. Average enhancement factors for the third harmonic generation (THG) from a self-affine silver surface, for the light polarized in the (x, y)-plane of the film ($G_{\text{THG}} \equiv G_{\|}$), and in the normal z-direction ($G_{\text{THG}} \equiv G_{\perp}$). (Source: Reprinted with permission from E. Y. Poliakov, V. A. Markel, V. M. Shalaev, and R. Botet, *Phys. Rev. B* 57, 14901 [1998]. © 1998 American Physical Society.)

The THG involves a higher power of electric fields, so that the dominance of local fields $\mathbf{E}_i$ over $\mathbf{E}_0$ leads to larger values of enhancement factors.

In Figure 21a and b, we plot spatial distributions for local-field enhancements at the fundamental frequency, $g = |\langle E_i \rangle / E_0|^2$ and for the local enhancements of SHG and THG, $g_{\text{SHG}} = g_{\text{SHG}}(\mathbf{r}_i) = |\mathbf{d}_i^{NL}(2\omega)|^2 / |\mathbf{d}_0^{NL}(2\omega)|^2$ and $g_{\text{THG}} = g_{\text{THG}}(\mathbf{r}_i) = |\mathbf{d}_i^{NL}(3\omega)|^2 / |\mathbf{d}_0^{NL}(3\omega)|$ (where $\mathbf{d}_0^{NL}$ and $\mathbf{d}_i^{NL}$ are the nonlinear dipoles in vacuum and on the film surface, respectively). The interactions of the nonlinear dipoles at the generated frequency is taken into account for both SHG and THG effects. The distributions of local enhancements are calculated for two wavelengths, 1 and 10 μm, for the light polarized

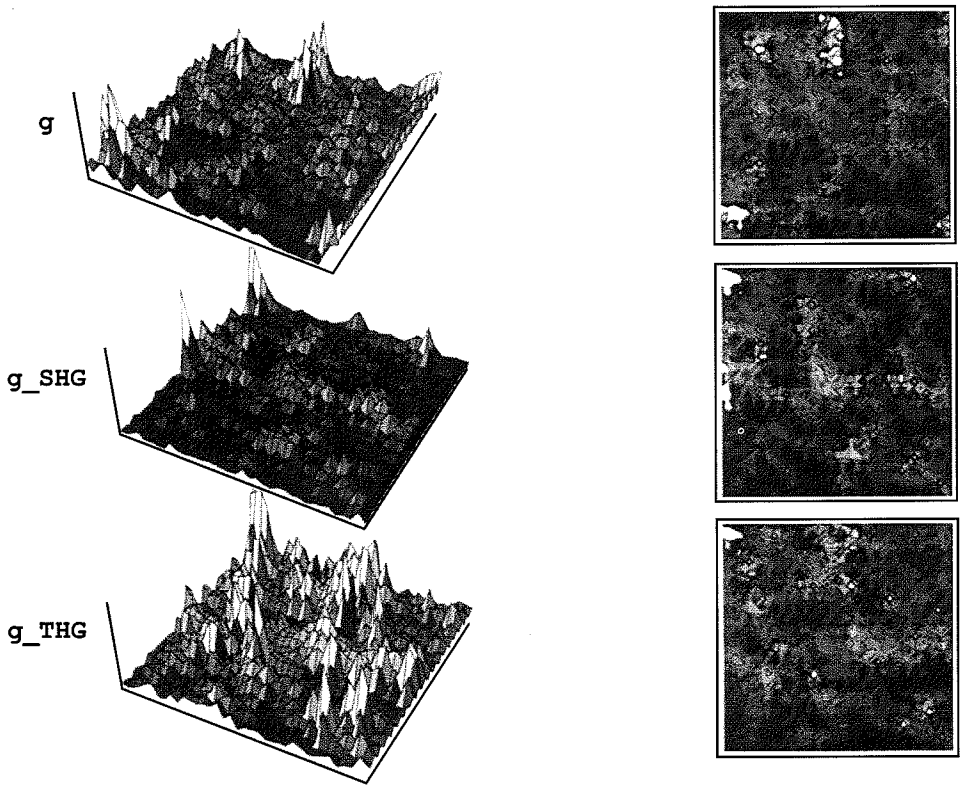

(a)

Fig. 21. Spatial distributions of the local enhancements for the field at the fundamental wavelength, g, for SHG signal, g_{SHG}, and for THG signal. The corresponding counterplots for the spatial distributions are also shown, in all cases. (a) The fundamental wavelength is $\lambda = 1$ μm. The linear scales are used in all cases. The highest enhancement values in the figures are as follows: $g = 5 \times 10^3$, $g_{SHG} = 5 \times 10^8$, and $g_{THG} = 2 \times 10^{12}$. (b) Same as in (a) but for $\lambda = 10$ μm. The highest enhancement values are as follows: $g = 3 \times 10^4$, $g_{SHG} = 10^{13}$, and $g_{THG} = 2 \times 10^{19}$. (Source: Reprinted with permission from E. Y. Poliakov, V. A. Markel, V. M. Shalaev, and R. Botet, *Phys. Rev. B* 57, 14901 [1998]. © 1998 American Physical Society.)

in the plane of the film. As was discussed earlier, the largest average enhancements are achieved in the infrared region, for the incident light polarized in the plane of the film. The local enhancements are also very large in this case.

In the counterplots of Figure 21a and b, the white spots correspond to higher intensities whereas the dark areas represent the low-intensity zones. We can see that spatial positions of the hot and cold spots in the local enhancements at the fundamental and generated frequencies are localized in small spatially separated parts of the film. Because the fundamental and generated frequencies are different, the fundamental and generated waves excite different optical modes of the film surface and, therefore, produce different local-field distributions. With the frequency alternation, the locations of the hot and cold change for all the fields, at the fundamental and generated frequencies. Thus different waves involved in the nonlinear interactions in a self-affine thin film produce nanometer-sized hot spots spatially separated for different waves. A similar effect was shown in the preceding text for Raman scattering from self-affine film [6].

The values of the local field intensities in Figure 21a and b, grow with the wavelength. The highest local enhancement factor in the spatial distribution g changes from 5×10^3 at $\lambda = 1$ μm to 3×10^4 at $\lambda = 10$ μm. For the SHG and the THG spatial distributions, the maximum increases from 5×10^8 to 10^{13} and from 2×10^{12} to 2×10^{19}, respectively. Such behavior correlates with the fact that the average enhancement factor also increases

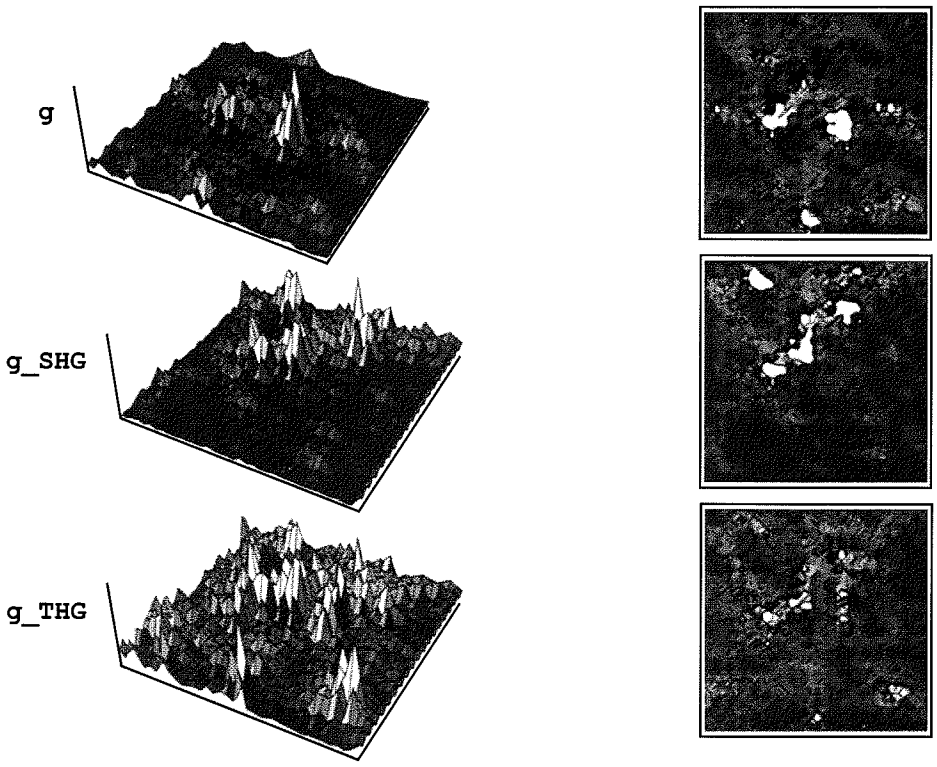

(b)

Fig. 21. (*Continued.*)

toward the infrared spectral region. We emphasize that the local enhancements can exceed the average one by several orders of magnitude. For example, comparison of the maximum local enhancement with the average enhancement for $\lambda = 1$ μm shows that the maximum intensity peaks exceed the average intensity by approximately 2 orders of magnitude for SHG (cf. Figs. 19 and 21) and by 4 orders of magnitude, for THG (cf. Figs. 20 and 21). This occurs, in part, due to the fact that the spatial separation between the hot spots can be significantly larger than their characteristic sizes, and, in part, due to destructive interference between the generated fields in different peaks.

The giant local enhancements of nonlinear processes (e.g., up to 10^{19} for THG at 10 μm) open a fascinating possibility of the fractal-surface-enhanced nonlinear optics and spectroscopy of single molecules. Also, if the near-field scanning optical microscopy is employed, nonlinear nano-optics and nanospectroscopy (with nanometer spatial resolution) become possible. In contrast, with the conventional far-zone optics only the average enhancement of optical processes can typically be measured.

The huge average enhancement for DFWM on a self-affine film is illustrated in Figure 22 (see (2)). The larger values of enhancement for DFWM, compared to THG, are explained by the fact that the interaction of nonlinear dipoles is stronger when the generated frequency is equal to the fundamental one. Also, the role of destructive interference for the field generated in different points is much larger for high-order harmonic generation than for DFWM.

In Figure 23a and b, we show the calculated real and imaginary parts of the Kerr enhancement factor. We calculated the enhancements using formula (1).

The calculations show that $|G'_K| > |G''_K|$, and both are especially large in the near-infrared. Note however that the signs of both real and imaginary parts of G_K strongly vary with λ; this means that the sign of nonlinear correction to refraction and absorption strongly

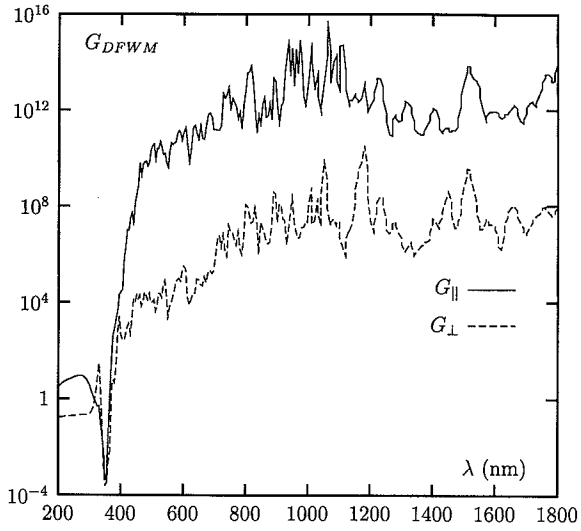

Fig. 22. Average DFWM enhancement factors from a self-affine silver surface, for the light polarized in the (x, y)-plane of the film ($G_{\mathrm{DFWM}} \equiv G_{\parallel}$) and in the normal z-direction ($G_{\mathrm{DFWM}} \equiv G_{\perp}$). (Source: Reprinted with permission from E. Y. Poliakov, V. A. Markel, V. M. Shalaev, and R. Botet, *Phys. Rev. B* 57, 14901 [1998]. © 1998 American Physical Society.)

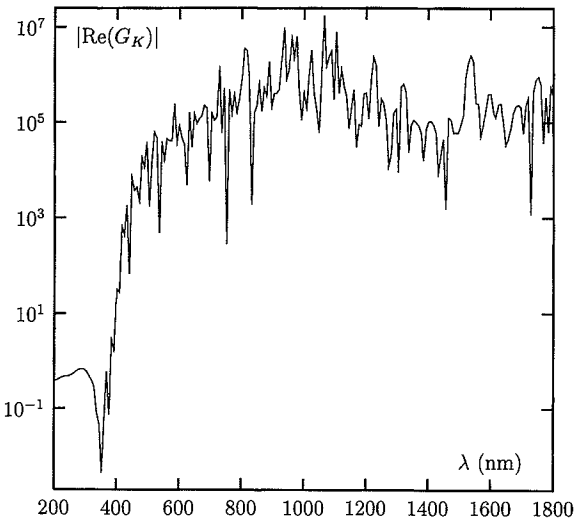

(a)

Fig. 23. Absolute values of (a) the real, $|G'_K|$, and (b) imaginary, $|G''_K|$, parts of the average enhancement factors for the Kerr-nonlinearity for the light polarized in the (x, y)-plane of the film. (Source: Reprinted with permission from E. Y. Poliakov, V. A. Markel, V. M. Shalaev, and R. Botet, *Phys. Rev. B* 57, 14901 [1998]. © 1998 American Physical Society.)

depends on the wavelength that can be a very useful property in designing photonic devices, such as optical switches.

5. RANDOM METAL-DIELECTRIC FILMS

For applications, it is important to have fractal films that retain their fractal morphology at room temperatures, such as two-dimensional random metal-dielectric films (referred to

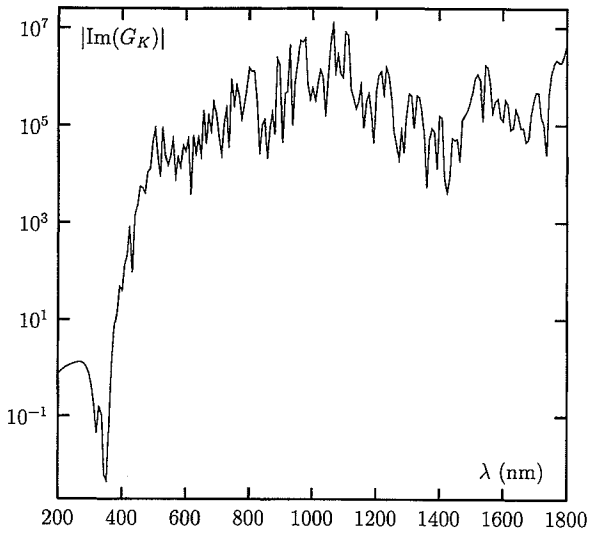

(b)

Fig. 23. (*Continued.*)

also as semicontinuous metal films) near the percolation threshold. In contrast to cold-deposited self-affine films that are essentially three-dimensional and do change their morphology when annealed, two-dimensional semicontinuous films remain stable at room temperatures.

Many of optical properties of particle aggregates are similar to those observed in metal-insulator random films. A semicontinuous metal film can be viewed as a two-dimensional ($2d$) composite material. Semicontinuous metal films can be produced by thermal evaporation or sputtering of metal onto an insulating substrate. In the growing process, first, small metallic grains are formed on the substrate. As the film grows, the metal filling factor increases and coalescences occur, so that irregularly shaped clusters are formed on the substrate eventually resulting in $2d$ fractal structures. The sizes of the fractal structures diverge in a vicinity of the percolation threshold. A percolating cluster of metal is eventually formed, when a continuous conducting path appears between the ends of a sample. The metal-insulator transition (the conductivity threshold) is very close to this point, even in the presence of quantum tunneling. At higher surface coverage, the film is mostly metallic, with voids of irregular shape; at further coverage increase, the film becomes uniform.

The optical properties of metal-dielectric films show anomalous phenomena that are absent for bulk metal and dielectric components. For example, the anomalous absorption in the near-infrared spectral range leads to anomalous behavior of the transmittance and reflectance. Typically, the transmittance is much higher than that of continuous metal films, whereas the reflectance is much lower (see Refs. [13, 59–64] and references therein). Near and well below the conductivity threshold, the anomalous absorptance can be as high as 50% [63, 65–68].

A number of the effective-medium theories were proposed for the calculation of the optical properties of semicontinuous random films, including the Maxwell-Garnett [69] and Bruggeman [70] approaches and their various modifications [13, 63, 64]. The renormalization group method is also widely used to calculate the effective dielectric response of $2d$ percolating films near the percolation threshold (see [71–73] and references therein).

A new theory based on the direct solution of the Maxwell equations have been suggested [74]. This new theory allows one to *quantitatively* describe the anomalous

absorption and other optical properties of semicontinuous films. However, the field fluctuations in semicontinuous metal films and the effects resulting from these fluctuations were not considered neither by the effective-medium theories nor by the theory of Ref. [74].

Nonlinear electrical and optical properties of percolating composites have attracted much attention. At zero frequency, strong nonlinearity may result in breaking down conducting elements when the electric current exceeds some critical value [75]. This fuse model can be also applied for the description of fractures in disordered media and related problem of weak tensility of materials in comparison to the strength of the atomic bonds (see [76] and references therein). The tension concentrates around weak points of materials and a crack spreads out starting from these weak points. Another example of unusual nonlinear behavior was observed for the ac and dc conductivity in the percolating mixture of carbon particles embedded in the wax matrix [77]. In this case, neither carbon particles nor wax matrix have any nonlinearity in their conductivities; nevertheless, the conductivity of a macroscopic composite sample increases twice when applied voltage is increased by a few volts. Such a strong nonlinear response can be attributed to the quantum tunneling between carbon particles; this is a distinguished feature of the electric transport in composites near the percolation threshold [78]. The current and electric field are concentrated in few hot junctions and they make it possible to change their conductances under action of the high local fields, whereas the external field is relatively small.

Percolating systems are very sensitive to the external electric field because their transport and optical properties are determined by a rather sparse network of conducting channels and the field concentrates in the weak points of the channels. Therefore composite materials can have much larger nonlinear susceptibilities at zero and finite frequencies than those of ordinary bulk materials. In particular, the cubic nonlinearity, which is of particular interest for a number of applications, was intensively studied (see, for example, [79, 80] and references therein).

The local-field fluctuations can be strongly enhanced in the optical and IR spectral ranges for a composite material consisting of a dielectric host and embedded in the host metallic elements that are characterized by the dielectric constant with negative real and small imaginary parts. Then the enhancement is due to the plasmon resonances in the metallic granules [2, 5–7, 32, 38, 79–83].

Nanostructured composite materials are potentially of great practical importance as media with an intensity-dependent dielectric function and, in particular, as nonlinear filters and optical bistable elements [80]. The response of a nonlinear composite can be tuned by controlling the volume fraction and the morphology of constitutes.

The enhancements of the optical nonlinearities associated with strong field fluctuations are especially large in composites with fractal morphology where the local fields experience giant fluctuations [2, 5, 6, 10, 56, 84] (see Sections 3 and 4).

Nonlinear optical properties of fractal aggregates were studied in [2, 5, 15, 82], where the authors showed that the aggregation of initially isolated particles into fractal clusters results in a huge enhancement of the nonlinear response within the spectral range of cluster modes associated with surface-plasmon resonances (see Section 3). The eigenmodes were found by diagonalizing the interaction operator of the dipoles induced by light on particles forming the cluster. Giant fluctuations of the local fields were studied by Markel et al. [10], Shalaev [2], Tsai et al. [3], Shalaev et al. [5, 6, 82] for the fractal aggregates, and Brouers et al. [84] for $2d$ percolating composites.

The areas of large field fluctuations are localized in different parts of the conducting clusters with random local structure [2, 3, 5, 6, 10, 40, 56, 84]. The prediction of large enhancements of optical nonlinearities in fractal clusters was confirmed experimentally for the example of degenerate four-wave mixing (DFWM) and nonlinear refraction and absorption [15, 30]. As shown in Section 3, aggregation of initially isolated silver particles into fractal clusters in these experiments led to a 10^6-fold enhancement of the efficiency of the nonlinear four-wave process and $\sim 10^3$ enhanced nonlinear refraction and absorption.

The localized and strongly fluctuating modes of fractal composites were also imaged by means of near-field optical spectroscopy in [3, 31].

Enhanced optical processes in composites of various (nonfractal and nonpercolating) morphology were also studied by Sipe, Boyd, and their co-workers both theoretically and experimentally [38].

If the skin effect in the metal grains is small, a semicontinuous film can be considered as a $2d$ object. Then in the optical spectral range where the frequency ω is much larger than the relaxation rate $\omega_\tau = \tau^{-1}$, a semicontinuous metal film can be modeled as a $2d$ L-R—C lattice [13, 85, 86]. The capacitance C stands for the gaps between metal grains that are filled by dielectric material (substrate) with the dielectric constant ε_d; the inductive elements, L-R, represent the metallic grains that for the Drude metal are characterized by the following dielectric function,

$$\varepsilon_m(\omega) = \varepsilon_b - \frac{(\omega_p/\omega)^2}{1 + i\omega_\tau/\omega} \tag{29}$$

where ε_b is a contribution to ε due to the interband transitions, ω_p is the plasma frequency, and $\omega_\tau = 1/\tau \ll \omega_p$ is the relaxation rate (note that earlier in formula (13) we used slightly different notations).

In the high-frequency range considered here, losses in metal grains are small, $\omega_\tau \ll \omega$. Therefore, the real part of the metal dielectric function is much larger (in modulus) than the imaginary part and it is negative for the frequencies ω exceeding the renormalized plasma frequency, $\omega_p^* = \omega_p/\sqrt{\varepsilon_b}$. Thus the metal conductivity is almost purely imaginary and metal grains can be modeled as L-R elements, with the active component much smaller than the reactive one.

It is instructive to consider first the film properties at the percolation threshold, p_c, where the exact Dykhne's result for the effective dielectric constant $\varepsilon_e = \sqrt{\varepsilon_d \varepsilon_m}$ [87] holds in the quasi-static case. If we neglect the metal losses and if we put $\omega_\tau = 0$, the metal dielectric constant ε_m is negative for frequencies smaller than the renormalized plasma frequency ω_p^*. We also neglect possible small losses in a dielectric substrate, assuming that ε_d is real and positive. Then, ε_e is purely imaginary for $\omega < \omega_p^*$. Therefore, a film consisting of loss-free metal and dielectric grains is absorptive, for $\omega < \omega_p^*$. The effective absorption in a loss-free film means that the electromagnetic energy is stored in the system and thus the local fields could increase unlimitedly. In reality, the local fields in a metal film are, of course, finite because of the losses. If the losses are small, one anticipates very strong field fluctuations. These large fluctuations result in giant enhancements of optical nonlinearities [2, 5–7, 10, 68, 74].

In this section we consider surface-enhanced optical nonlinearities of semicontinuous metal films. The section is organized as follows. First, we briefly recapitulate the approach developed in [7] for calculating local fields on a semicontinuous film. We describe here the used numerical recipe and we show results of our calculations for local-field distributions. It is shown that local-field distributions consist of very sharp peaks that in some cases are correlated in space. We also consider here dependencies of the field distributions on the light wavelength and metal concentration. We discuss the scaling theory that describes the field distributions and their dependencies on the wavelength and metal concentration. The theory allows one to estimate enhancements of different nonlinearities. We discuss results of numerical simulations of the surface-enhanced optical nonlinearities. The spatial local distributions of the enhanced optical nonlinearities on a random semicontinuous films are considered. A distinctive feature of these distributions is that most of the enhancement occurs in localized nm-sized areas. The enhancement in these "hot zones" is giant and exceeds a "background" nonlinear signal by many orders of magnitude. These novel effects can be obtained experimentally in the optical range by using, for example, near-field scanning optical microscopy (NSOM) allowing a subwavelength resolution [3, 31, 57, 88] and, in the microwave range, by using the subwavelength probe method [68].

5.1. Linear Response

We consider the optical properties of a semicontinuous film consisting of metal grains randomly distributed on a dielectric substrate. The film is placed in the $\{x, y\}$ plane, whereas the incident wave propagates in the z direction. The local conductivity, $\sigma(\mathbf{r})$, of the film takes either the "metallic" values $\sigma(\mathbf{r}) = \sigma_m$ in metallic grains or the "dielectric" values, $\sigma(\mathbf{r}) = -i\omega\varepsilon_d/4\pi$, outside the metallic grains. The vector $\mathbf{r} = \{x, y\}$ has two components in the plane of the film; ω is the frequency of the incident wave. The gaps between metallic grains are assumed to be filled by the material of the substrate, so that the previously introduced ε_d is assumed to be equal to the dielectric constant of the substrate. The electric field in the film is homogeneous in the direction z perpendicular to the film plane; this means that the skin depth for the metal, $\delta \cong c/(\omega\sqrt{|\varepsilon_m|})$, is much larger than the metal grain size, a_0, and the quasi-static approximation can be applied for calculating the field distributions. We also take into account that the wavelength of the incident wave is much larger than any characteristic size of the film, including the grain size and the gaps between the grains. In this case, the local field, $\mathbf{E}(\mathbf{r})$, can be represented as

$$\mathbf{E}(\mathbf{r}) = -\nabla\phi(\mathbf{r}) + \mathbf{E}_e(\mathbf{r}) \tag{30}$$

where $\mathbf{E}_e(\mathbf{r})$ is the applied (macroscopic) field, and $\phi(\mathbf{r})$ are the potentials of the fluctuating fields inside the film. The current density, $\mathbf{j}(\mathbf{r})$, at point $\mathbf{r}$ is given by the Ohm's law,

$$\mathbf{j}(\mathbf{r}) = \sigma(\mathbf{r})\big[-\nabla\phi(\mathbf{r}) + \mathbf{E}_e(\mathbf{r})\big] \tag{31}$$

The current conservation law, $\nabla \cdot \mathbf{j}(\mathbf{r}) = 0$, has the following form,

$$\nabla \cdot \big(\sigma(\mathbf{r})\big[-\nabla\phi(\mathbf{r}) + \mathbf{E}_e(\mathbf{r})\big]\big) = 0 \tag{32}$$

We solve Eq. (32) to find the fluctuating potentials, $\phi(\mathbf{r})$, and the local fields, $\mathbf{E}(\mathbf{r})$ induced in the film by the applied field, $\mathbf{E}_e(\mathbf{r})$. Because the wavelength of the incident EM wave is much larger than all spatial scales in a semicontinuous metal film, the applied field, $\mathbf{E}_e$, is constant in the film plane, $\mathbf{E}_e(\mathbf{r}) = \mathbf{E}^{(0)}$. The local fields, $\mathbf{E}(\mathbf{r})$, induced by the applied field, $\mathbf{E}^{(0)}$, can be obtained by using the nonlocal conductivity, $\widehat{S}$, introduced in [7],

$$\mathbf{E}(\mathbf{r}) = \frac{\mathbf{j}(\mathbf{r})}{\sigma(\mathbf{r})} = \frac{1}{\sigma(\mathbf{r})}\int \widehat{S}(\mathbf{r}, \mathbf{r}')\mathbf{E}^{(0)}\, d\mathbf{r}' \tag{33}$$

According to (33), the nonlocal conductivity, $\widehat{S}(\mathbf{r}, \mathbf{r}')$ relates the applied field at point $\mathbf{r}'$ to the current and the local field at point $\mathbf{r}$.

The nonlocal conductivity in (33) has been expressed in terms of the Green function of Eq. (32) [7],

$$S^{\alpha\beta}(\mathbf{r}_2, \mathbf{r}_1) = \sigma(\mathbf{r}_2)\sigma(\mathbf{r}_1)\frac{\partial^2 G(\mathbf{r}_2, \mathbf{r}_1)}{\partial r_2^{\alpha}\, \partial r_1^{\beta}} \tag{34}$$

where the Greek indices take values 1 or 2. The Green function is symmetric with respect to the interchange of its arguments: $G(\mathbf{r}_1, \mathbf{r}_2) = G(\mathbf{r}_2, \mathbf{r}_1)$; therefore, Eq. (34) implies that the nonlocal conductivity is also symmetric [7],

$$S^{\alpha\beta}(\mathbf{r}_1, \mathbf{r}_2) = S^{\beta\alpha}(\mathbf{r}_2, \mathbf{r}_1) \tag{35}$$

The introduced nonlocal conductivity $\widehat{S}$ is useful for analysis of different processes in the system.

Later we use the nonlocal conductivity matrix $S^{\alpha\beta}(\mathbf{r}_1, \mathbf{r}_2)$ to express various nonlinear currents in terms of the local fields.

To calculate the local electric fields in the system we discretize Eq. (32) on a square lattice. The potentials in the cites of the lattice reproduce the local-field potentials in a semicontinuous film. The conductivities of the lattice bonds stand for the local film conductivity and take either σ_m or σ_d values. In such a way the partial differential Eq. (32) is

reduced to the set of the Kirchhoff's equations that are solved by the method presented in the next subsection. As soon as distribution is known we use the nonlocal conductivity to calculate the optical nonlinearities.

Next in this section, we first describe the used numerical procedure and then we describe the results of our numerical simulations for the field distributions and for the surface-enhanced optical nonlinearities.

5.2. Numerical Model

There now exist very efficient numerical methods for calculating the effective conductivity of composite materials (see [13, 61]), but they typically do not allow calculations of the field distributions. Here, we use instead the real space renormalization group (RSRG) method that was suggested by Reynolds et al. [89] and Sarychev [90] and then extended to study the conductivity [91] and the permeability of oil reservoirs [92]. Later, we follow the approach used by Aharony [92]. This method can be adopted to finding the field distributions in the following way. First, we generate a square lattice of L-R (metal) and C (dielectric) bonds using a random number generator. As seen in Figsure 24, such a lattice can be considered as a set of "corner" elements. One of such elements is labeled as (ABCDEFGH), in Figure 24. In the first stage of the RSRG procedure, each of these elements is replaced by the two Wheatstone bridges, as shown in Figure 24. After this transformation, the initial square lattice is converted to another square lattice, with the distance between the sites twice larger and with each bond between the two nearest neighboring sites being the Wheatstone bridge. Note that there is a one-to-one correspondence between the "x" bonds in the initial lattice and the x bonds in the x directed bridges of the transformed lattice, as seen in Figure 24. The same one-to-one correspondence exists also between the "y" bonds. The transformed lattice is also a square lattice, and we can again apply to it the RSRG transformation. We continue this procedure until the size l of the system is reached. As a result, instead of the initial lattice, we have two large Wheatstone bridges in the x and y directions. Each of them has a hierarchical structure consisting of bridges with the sizes from 2 to l. Because the one-to-one correspondence is preserved at each step of the transformation, the correspondence also exists between the elementary bonds of the transformed lattice and the bonds of the initial lattice.

After using the RSRG transformation, we apply an external field to the system and we solve the Kirchhoff equations to determine the fields and the currents in all the bonds of the transformed lattice. Due to the hierarchical structure of the transformed lattice, these equations can be solved exactly. Then, we use the one-to-one correspondence between the elementary bonds of the transformed lattice and the bonds of the initial square lattice to find the field distributions in the initial lattice as well as its effective conductivity. The number of operations to get the full distributions of the local fields is proportional to l^2 to be compared with l^7 operations needed in the transform-matrix method [13] or l^3 operation needed in

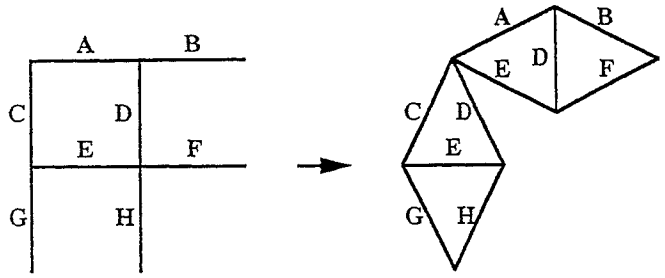

Fig. 24. Real space renormalization scheme. (Source: Reprinted with permission from F. Brouers, S. Blacher, A. Lagarkov, A. K. Sarychev, P. Gadenne, and V. M. Shalaev, *Phys. Rev. B* 56, 13234 [1997]. © 1997 American Physical Society.)

the well-known Frank–Lobb algorithm [93], which does not give the field distributions but the effective conductivity only.

The RSRG procedure is certainly not exact because the effective connectivity of the transformed system does not repeat exactly the connectivity of the initial square lattice. To check the accuracy of the RSRG, we solved the $2d$ percolating problem using this method. Namely, we calculated the effective parameters of a two component composite with the real metallic conductivity, σ_m, much larger than the real conductivity, σ_d, of the dielectric component, $\sigma_m \gg \sigma_d$. We obtained the percolation threshold $p_c = 0.5$ and the effective conductivity at the percolation threshold that is very close to $\sigma(p_c) = \sqrt{\sigma_m \sigma_d}$. These results coincide with the exact ones for $2d$ composites [87]. This is not surprising because the RSRG procedure preserves the self-duality of the initial system. The critical exponents obtained by the RSRG are also close to the known values of the exponents from the percolation theory [13].

5.3. Field Distributions on a Semicontinuous Film

In the following text, we set the applied field $E^{(0)}$ to equal unity, $E^{(0)} = 1$, whereas the local fields inside the system are complex quantities.

The dielectric constant of silver grains has the form of Eq. (29), with the interband transitions contribution $\varepsilon_b = 5.0$, the plasma frequency $\omega_p = 9.1$ eV, and the relaxation frequency $\omega_\tau = 0.021$ eV [17]. Later, we set $\varepsilon_d = 2.2$ typical for glass.

In Figure 25 we show the field distributions $g(\mathbf{r}) = |\mathbf{E}(\mathbf{r})/\mathbf{E}^{(0)}|^2$ for $\varepsilon_m = -\varepsilon_d$ that for silver corresponds to $\lambda \approx 365$ nm. The value $\varepsilon_m = -\varepsilon_d$ gives the resonance of an isolated metal particle. (For a $2d$, i.e., z-independent problem, particles can be thought of as infinite in the z-direction cylinders that resonate, in the quasi static approximation, at $\varepsilon_m = -\varepsilon_d$, for the field polarized in the x, y-plane.) The results are presented for the various metal fraction, p.

For $p = 0.001$, particles practically do not interact, so that all the peaks are almost of the same height and they indicate the locations of metal particles. Note that similar distribution is obtained for $p = 0.999$ when the role of particles is played by the dielectric voids.

For $p = 0.1$ and, especially, for $p = 0.5$, particles form clusters of strongly interacting particles. These clusters resonate at different frequencies (than that for an isolated particle) and therefore for the chosen frequency the field peaks are, on average, smaller than those for isolated particles. We emphasize a strong resemblance in the field distributions for p and $1 - p$ (cf. Fig. 25a, g, b, and f, c, and e).

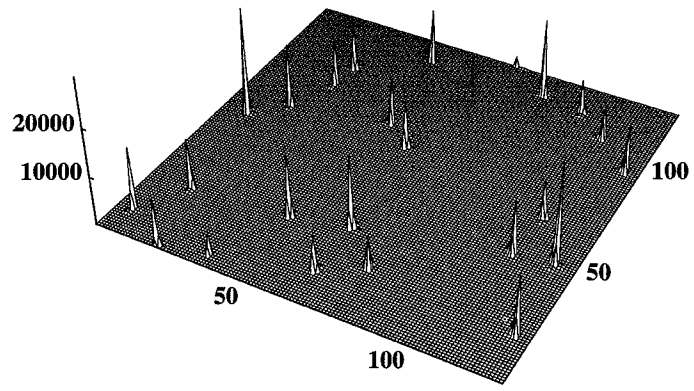

(a)

Fig. 25. Distribution of the local field intensities on a metal semicontinuous film for $\varepsilon'_m = -\varepsilon_d = -2.2$ ($\lambda \approx 365$ nm for silver in air) at different metal concentrations, p. (a) $p = 0.001$, (b) $p = 0.01$, (c) $p = 0.1$, (d) $p = 0.5$, (e) $p = 0.9$, (f) $p = 0.99$, and (g) $p = 0.999$. (Source: Reprinted with permission from V. M. Shalaev and A. K. Sarychev, *Phys. Rev. B* 57, 13265 [1998]. © 1998 American Physical Society.)

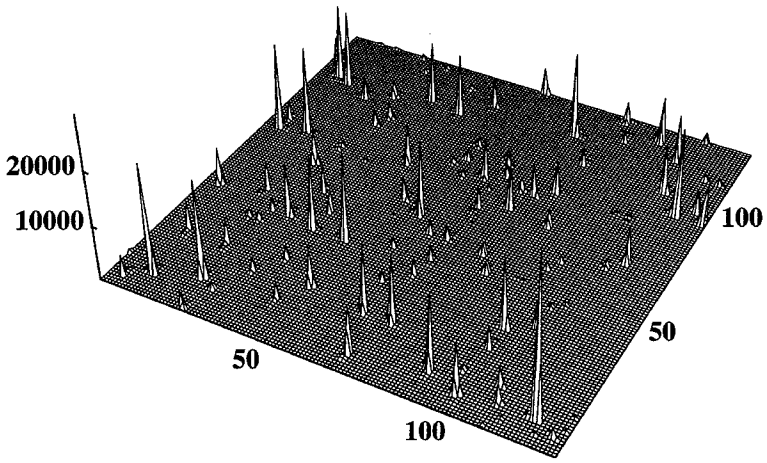

(b)

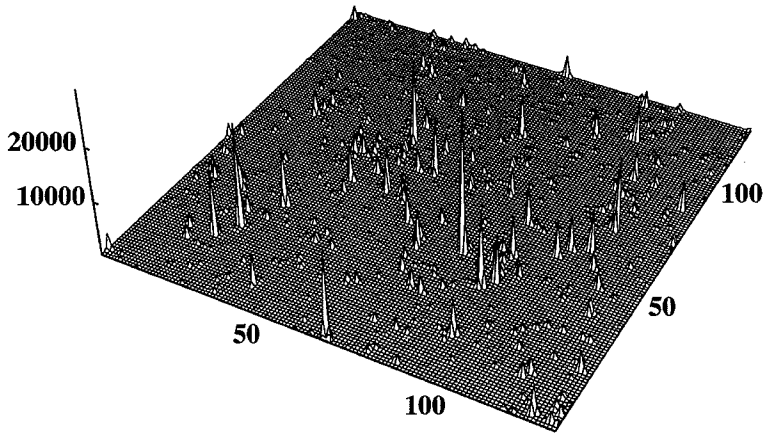

(c)

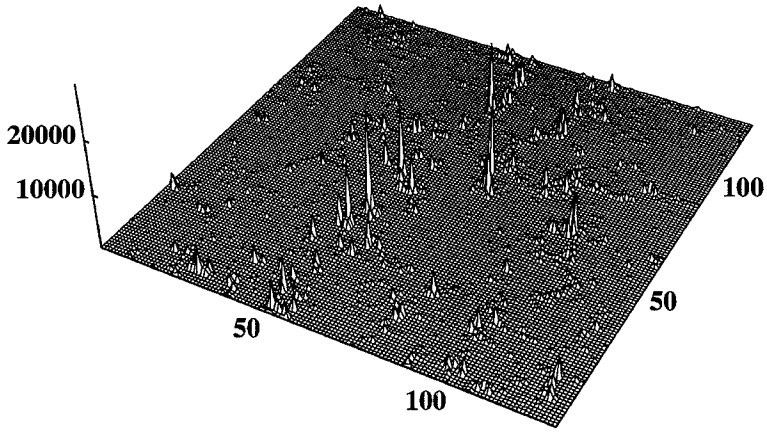

(d)

Fig. 25. (*Continued.*)

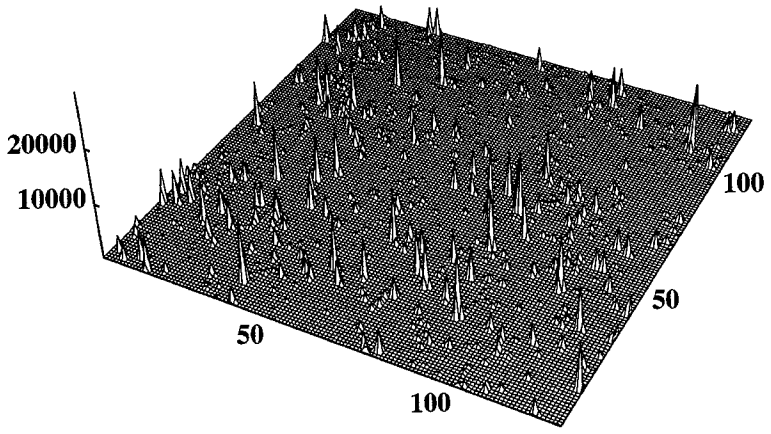

(e)

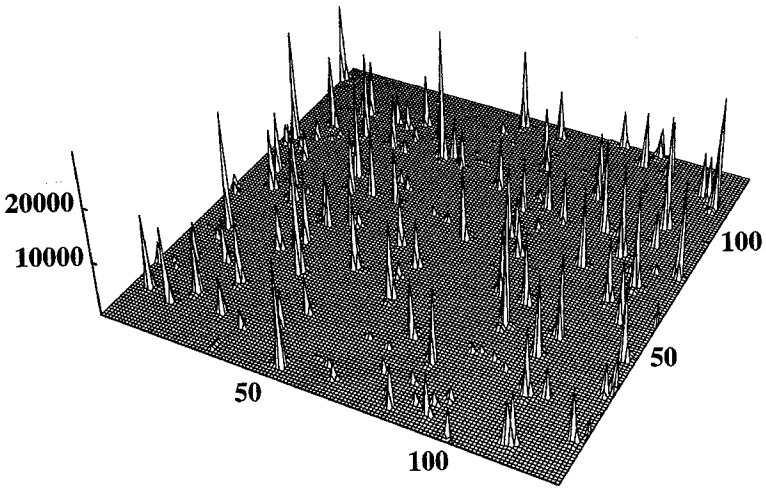

(f)

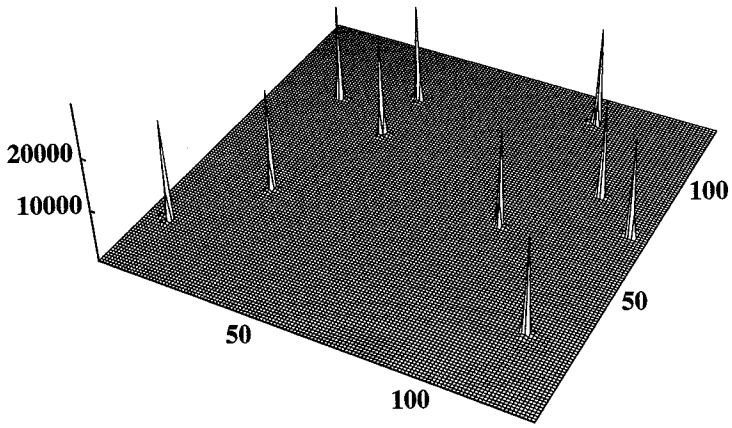

(g)

Fig. 25. (*Continued.*)

For larger wavelengths, a single metal grain is off the plasmon resonance. Nevertheless, as one can see from Figure 26a–d, the local-field fluctuations are even larger than those at the plasmon resonance frequency. At these wavelengths, clusters of the conducting particles (rather than individual particles) resonate with the external field oscillations. Therefore it is not surprising that the local-field distributions are quite different from those in Figure 25.

In Figure 26, the field distributions at the percolation threshold $p = p_c = 0.5$ are shown, for different wavelengths. Note that the field intensities in peaks increase with λ, reaching very high values, $\sim 10^5$; the peak spatial separations increase with λ as well. In the next subsection, we consider a scaling theory for the field distributions on a semicontinuous film that explains the pevious results of simulations.

Note that in our method of simulating films, samples with same p correspond to identical films. Thus from Figure 26, we can conclude that spatial locations of the field peaks strongly depend on the frequency. Qualitatively similar results were previously

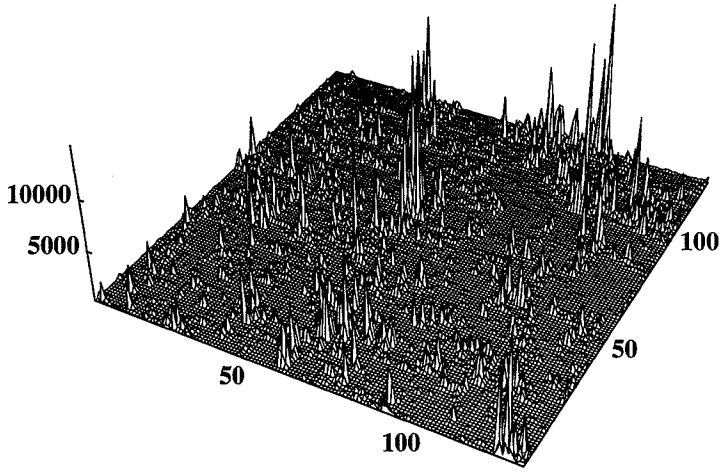

(a)

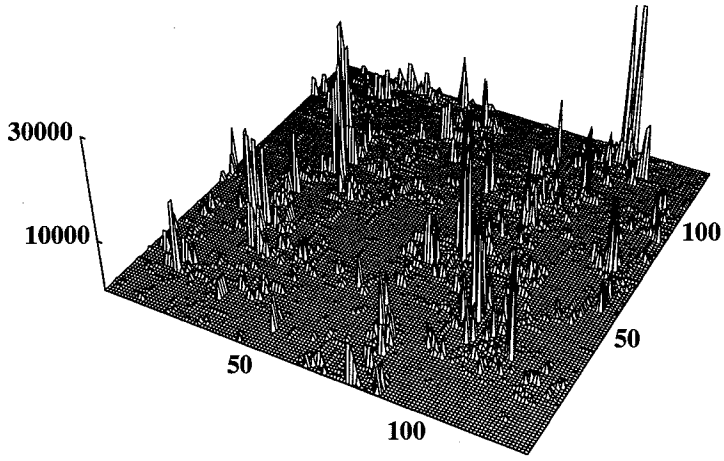

(b)

Fig. 26. Distribution of the local field intensities on a semicontinuous film at the percolation threshold for different wavelengths; (a) $\lambda = 0.5$ μm, (b) $\lambda = 1.5$ μm, (c) $\lambda = 10$ μm, and (d) $\lambda = 20$ μm. (Source: Reprinted with permission from V. M. Shalaev and A. K. Sarychev, *Phys. Rev. B* 57, 13265 [1998]. © 1998 American Physical Society.)

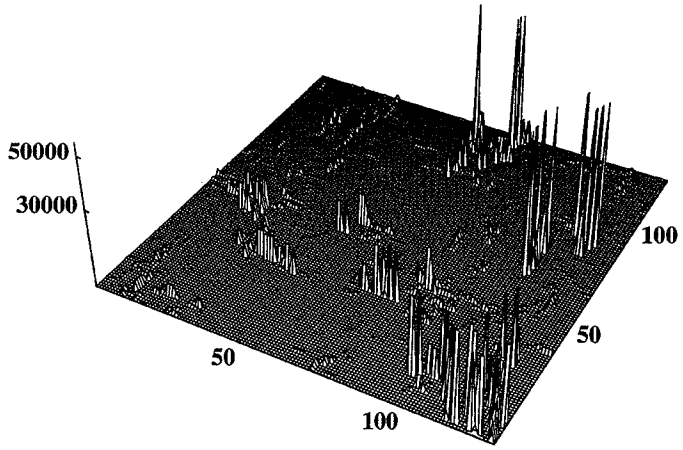

(c)

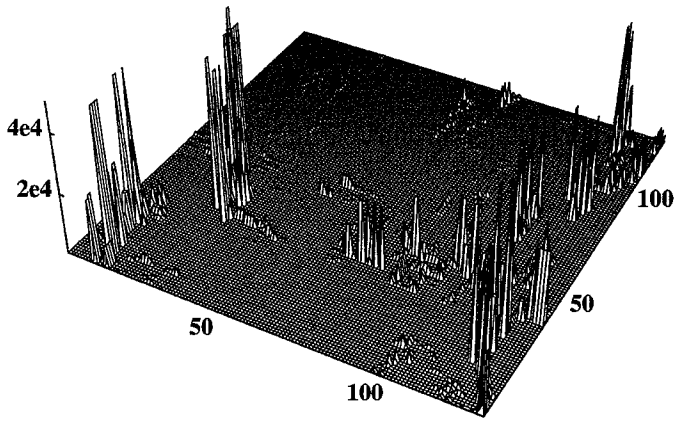

(d)

Fig. 26. (*Continued.*)

demonstrated for fractals and self-affine films [2, 5, 6]. Thus by changing the frequency one can excite different nm-sized hot spots on a film. This effect is of high potential for various applications, and it can be studied experimentally in the optical spectral range using near-field scanning optical microscopy (NSOM) providing subwavelength resolution [3, 31, 57, 88]; in the microwave range it can be studied easily by the local probe method developed [68].

We emphasize that all results are shown in the natural linear scales; therefore, what we see in the figures is a top part of the field distribution, that is, only the largest fields. The fields in other points forming a background, although smaller, are not, of course, zero. However, for the nonlinear optical effects studied here the largest fields play the most important role and the smaller background fields (that are not seeing in the figures) can in most cases be neglected.

In Figure 27, we also show results of our calculations for the average enhancements for the intensity of the local fields, $\langle|\mathbf{E}(\mathbf{r})/\mathbf{E}^{(0)}|^2\rangle$. The results are presented as a function of p, for different wavelengths, $\lambda = 0.5$ μm, $\lambda = 1.5$ μm, and $\lambda = 10$ μm. We see that the field enhancements are large on average ($\sim 10^2$) but much smaller than in the local peaks in Figure 26. This is because the largest peaks are separated by relatively large distances so that the average enhancement is not as large as the local one in the peaks.

The other moments of the field distribution, that are important for estimation of the nonlinear response, experience even stronger enhancement, especially, for the concentrations

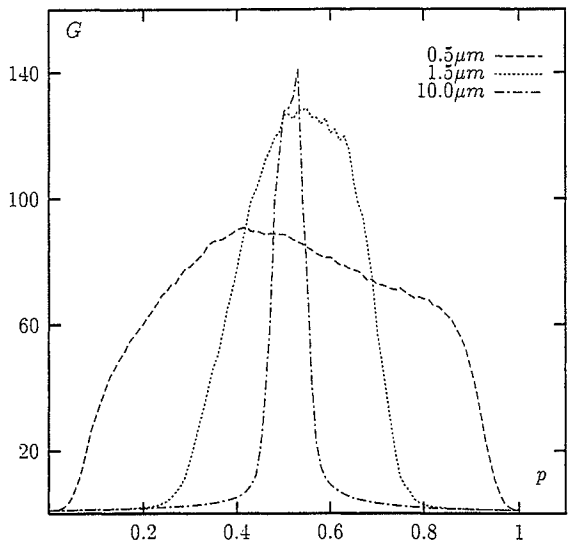

Fig. 27. Average field enhancement, $G = \langle |\mathbf{E}(\mathbf{r})/\mathbf{E}^{(0)}|^2 \rangle$, on a silver semicontinuous film as a function of the metal concentration, p, for three different wavelengths. (Source: Reprinted with permission from V. M. Shalaev and A. K. Sarychev, *Phys. Rev. B* 57, 13265 [1998]. © 1998 American Physical Society.)

close to the percolation threshold. For example, the fourth moment $\langle |\mathbf{E}(\mathbf{r})/\mathbf{E}^{(0)}|^4 \rangle$ exceeds the value 10^6 for $p = p_c$ and $\lambda > 1$ μm. It is not surprising because the local fields raised to the fourth power, $|\mathbf{E}(\mathbf{r})/\mathbf{E}^{(0)}|^4$, reach in the peaks the values 10^{11}, as follows from Figure 26.

The range of p, where the enhancements occur is very large in the visible range ($\Delta p \approx 0.9$) but it shrinks toward the larger wavelengths, as seen in the figure (see the following text also).

From the foregoing results it follows that the local fields experience strong space fluctuations on a semicontinuous film; the large fields in the peaks result in giant enhancements of optical nonlinearities considered later.

5.4. Scaling Theory of the Field Fluctuations and the Surface-Enhanced Optical Nonlinearities

As pointed out previously large local fields within spatially separated peaks on a film imply that the spatial field fluctuations are also large. One could anticipate that the local fields are strong in a semicontinuous film for ω slightly smaller than ω_p, that is, $\omega \leqslant \omega_p^*$, where ω_p^* is the renormalized plasma frequency introduced earlier. For the frequency range $\omega \leqslant \omega_p^*$ the real part of the metal dielectric constant ε_m is negative and its absolute values are of the order of unity, that is, they are close to the dielectric constant of the film substrate, ε_d. Therefore, the conductivities of the L-R and C elements in the equivalent network have the opposite signs and they are close to each other in absolute values. Thus, a semicontinuous film can be thought of as a system of the contours tuned in resonance with the frequency of the external field. These resonance modes are seen as giant spatial fluctuations in the field distributions over the film. In the dilute case $p \ll 1$ these resonances are associated with plasmon resonances of individual metal grains.

What might be more surprising is the fact that the giant fluctuations of the local fields also occur for $\omega \ll \omega_p^*$, when the contrast $H = |\varepsilon_m|/\varepsilon_d \gg 1$. If the contrast $H \gg 1$, the conductivity of the L-R and C elements of the equivalent network are quite different and a single contour cannot be excited by the external field. However, as our numerical simulations show, the field fluctuations become larger with the increase of the wavelength λ toward the infrared spectral range (see Fig. 26).

To understand the origin of the giant field fluctuations for the large contrast, $H \gg 1$, we invoke scaling arguments of the percolation theory [62]. In the following text we develop further the scaling approach from our previous work [7] and we apply it for calculating the high-order field moments.

Because enhancements for the nonlinear optical processes have maxima near the percolation threshold p_c, we assume first that the concentration of the conducting particles, p, is exactly equal to the percolation threshold, $p = p_c$. We consider the case when the frequency ω is much smaller than the plasma frequency, $\omega \ll \omega_p$, so that the contrast can be approximated as $H \approx (\omega_p/\omega)^2/\varepsilon_d \gg 1$. We also assume that $\omega \gg \omega_\tau$, that is, losses in the metal grains are relatively small. To find the field distributions over the system, we apply the renormalization procedure first suggested in [89, 90]. We divide a system into squares of size l and we consider each square as a new element. All such squares can be classified into two types. A square that contains a path of conducting particles spanning over is considered as a "conducting" element. A square without such an "infinite" cluster is considered as a nonconducting, dielectric element. Following the finite size arguments [61, 62, 89, 90], the effective dielectric constant of a conducting square, $\varepsilon_m^*(l)$, decreases with increasing its size l as

$$\varepsilon_m^*(l) = \left(\frac{l}{a_0}\right)^{-t/\nu_p} \varepsilon_m \tag{36}$$

where a_0 is the average size of the metal grains, and t and ν_p are the critical exponents for the conductivity and the percolation correlation length, respectively. For a $2d$ system, $t \approx \nu_p = \frac{4}{3}$ [13, 61, 62].

The effective dielectric constant of a dielectric square, $\varepsilon_d^*(l)$, increases with increasing its size, l as

$$\varepsilon_d^*(l) = \left(\frac{l}{a_0}\right)^{s/\nu_p} \varepsilon_d \tag{37}$$

where s is the critical exponent for the static dielectric constant; $s \approx \nu_p = \frac{4}{3}$, for a $2d$ system [13, 61, 62].

We now set the square size, l, to be equal to l^*,

$$l = l^* = a_0 \left(\frac{|\varepsilon_m'|}{\varepsilon_d}\right)^{\nu_p/(t+s)} \tag{38}$$

where $\varepsilon_m' + i\varepsilon''_m \equiv \mathrm{Re}(\varepsilon_m) + i\,\mathrm{Im}(\varepsilon_m)$. Then, in the renormalized system where each square of the size l^* is considered as a single element, the ratio of the dielectric constants of these new elements is equal to

$$\frac{\varepsilon_m^*(l^*)}{\varepsilon_d^*(l^*)} \cong \frac{\varepsilon_m}{|\varepsilon_m'|} = -1 + i\kappa \tag{39}$$

where the loss factor $\kappa = \varepsilon''_m/|\varepsilon_m'| \approx \omega_\tau/\omega \ll 1$. [Recall that in the visible and the IR spectral ranges the real part of the metal dielectric constant, ε_m', is negative and large in magnitude, $|\varepsilon_m'| \gg \varepsilon_d$.]

It follows from Eq. (39) that the renormalized system is a system of the L-R and C elements tuned in the resonance. Therefore, the local electric fields, $E^*(l^*)$, are significantly enhanced in comparison with the macroscopic field, $E^{(0)}$. High local fields $E^*(l^*)$ are due to the plasmon resonances of different metal clusters.

As shown in Ref. [7], in a $2d$ system with the ratio of ε_m to ε_d given by Eq. (39), the field E^* can be estimated as

$$E^* \cong E^{(0)}\kappa^{-\gamma/2} \gg E^{(0)} \tag{40}$$

where the critical exponent γ is about unity, $\gamma \cong 1.0$.

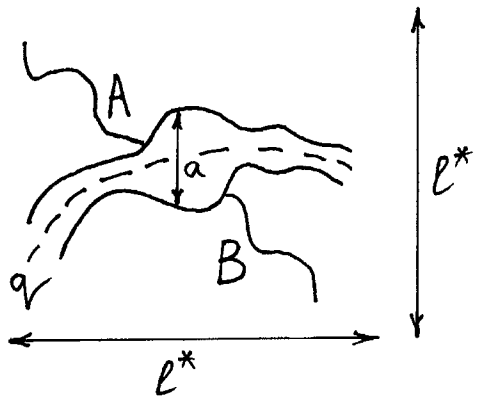

Fig. 28. Typical configuration of the conducting clusters that resonate at the frequency ω much smaller than the plasma frequency ω_p. (Source: Adapted from V. M. Shalaev and A. K. Sarychev, *Phys. Rev. B* 57, 13265 [1998].)

Now we can estimate the field fluctuations in the original system. A typical configuration of conducting clusters that resonate at frequency $\omega \ll \omega_p$ is sketched in Figure 28. The gap between the two conducting clusters A and B has a capacitive conductance $\sum_c^{AB}(l) \simeq -i\omega\varepsilon_d^*(l)a_0/4\pi$ that depends on the size l of the considered clusters.

The conducting paths coming to the gap have an inductive conductance $\sum_i^{AB}$; this is because the metal conductivity is inductive for $\omega < \omega_p^*$ ($\varepsilon_m' < 0$, $|\varepsilon_m'| \gg \varepsilon_m''$). The effective value of $\sum_i^{AB}$ can be estimated from a simple observation that a conducting square of the size l has a typical conductivity $-i\omega\varepsilon_m^*(l)/4\pi$ that we attribute to the presence of the conducting path. Thus we obtain $\sum_i^{AB}(l) \simeq -i\omega\varepsilon_m^*(l)a_0/4\pi$.

We chose the size $l = l^*$ so that capacitive and inductive conductance are equal to each other in modulus, $|\sum_c^{AB}(l^*)| = |\sum_i^{AB}(l^*)|$. Then there is a resonance in the configuration presented in Figure 28. Note that an intercluster capacitive conductance $\sum_c^{AB}(l)$ increases with the cluster size whereas an inductive conductance $\sum_i^{AB}(l)$ decreases with increasing l. Therefore we can always find proper pairs of clusters with the size $l = l^*$ to fulfill the resonance condition $|\sum_c^{AB}(l^*)| = |\sum_i^{AB}(l^*)|$ for any large (in modulus) value of the metal dielectric constant $\varepsilon_m(\omega)$, provided $\varepsilon_m'(\omega) < 0$ (i.e., $\omega < \omega_p^*$). This is the reason why the giant local field fluctuations exist up to the far infrared spectral range.

In Figure 28, we do not show many finite conducting clusters that are always present in the system. These clusters are off the resonance and, therefore, are not important for our consideration. Therefore only a small part of the metal component is involved in the resonance excitation, at any particular frequency of the applied field. Accordingly, only few metal grains carry most of the current. Nevertheless the resonating clusters cover almost the whole area of the film due to their fractal structure. If we change the frequency, another set of metal clusters resonates; these new resonating clusters still include only a small part of the metal component despite the fact that they cover almost the whole film area. For different frequencies, the metal grains that carry the current are, in general, different.

The field E_{AB} in the intercluster gap is strongly enhanced at the resonance $l = l^*$. The potential drop across the gap can be estimated as $U_{AB}^* \sim E^* l^*$, (see Eqs. (38) and 40)) and, therefore, the local field is estimated as $E(q) \sim U_{AB}^*/a(q)$, where $a(q)$ is the distance across the gap between clusters A and B, q is a varying coordinate along the gap between the two clusters (see Fig. 28).

The nth moment of the local field $E(q)$ in the gap is given by the following equation,

$$\langle |E|^n \rangle_{AB} \simeq \frac{\int {U_{AB}^*}^n a(q)^{-n+1}\, dq}{\int a(q)\, dq} \tag{41}$$

This equation can be rewritten in the following form,

$$\langle |E|^n \rangle_{AB} \simeq (E^* l^*)^n \frac{\langle a^{1-n} \rangle_{AB}}{\langle a \rangle_{AB}} \tag{42}$$

that depends only on the geometry of the intercluster gap.

We note that there is not any characteristic length in a percolating system for scales smaller than l^* except the l^* itself and the microscopical scale a_0. Therefore it is plausible to assume that the distances a are distributed uniformly between $a_{\min} \simeq a_0$ and $a_{\max} \leqslant l^*$. Then Eq. (42) gives for the electric field averaged over the gap the result $\langle E \rangle_{AB} = E^*$, which means that $\langle E \rangle_{AB}$ is equal to the "external" field E^* applied to the square of the size l^*. One could anticipate this result because the field concentrates in the intercluster gap and the averaging over the gap is equivalent to the average over the total square of the size l^*; this, along with the fact that the local field averaged over some system should be equal to the applied field, explains the obtained result.

The averaging over a system can be reduced to the averaging over a gap in the general case so that Eq. (42) estimates the moments of the field distribution for an entire semicontinuous metal film.

In particular, the second moment, $\langle |E|^2 \rangle$ (characterizing the average intensity of the local electric field) is equal to

$$\langle |E|^2 \rangle \simeq E^{*2} \left(\frac{l^*}{a_0} \right)^{s/\nu_p} \tag{43}$$

Substituting in (43) the expressions for l^* and E^* given by Eqs. (38) and (40), we obtain the expression for the average field intensity,

$$\langle |E|^2 \rangle \simeq \left| E^{(0)} \right|^2 \left(\frac{|\varepsilon'_m|}{\varepsilon''_m} \right)^{\gamma} \left(\frac{|\varepsilon_m|}{\varepsilon_d} \right)^{s/(t+s)} \tag{44}$$

For a $2d$ system, $t \approx s \approx \nu_p = \frac{4}{3}$. Substituting these critical indices and $\gamma = 1$ in (44), we obtain

$$\langle |E|^2 \rangle \simeq \left| E^{(0)} \right|^2 \frac{|\varepsilon'_m|}{\varepsilon''_m} \left(\frac{|\varepsilon_m|}{\varepsilon_d} \right)^{1/2} \tag{45}$$

From this equation follows that the average intensity of the local fields in a semicontinuous film $\langle |E|^2 \rangle$ increases with $|\varepsilon'_m|$ when the ω drops below the renormalized frequency ω_p^*; the average intensity tends to saturate as frequency decreases further (see Fig. 27) and, finally, the average intensity decreases steeply toward the long wavelength part of the spectrum: $\langle |E|^2 \rangle \sim \omega_p / \omega_\tau$, $\omega \gg \omega_p$.

Note that the field concentrates at the points of nearest approach between the resonant clusters. The sharp peaks in Figure 26 are associated with these points. We also note that all the points in the intercluster gap are important in calculating the average field $\langle E \rangle$ and the average intensity $\langle |E|^2 \rangle$.

The situation completely changes for the third and higher moments of the field distribution ($\langle |E|^n \rangle$, $n \geqslant 3$). As follows from Eqs. (41) and (42), the field in the points of the closest approach of the resonant clusters plays a decisive role for the moments with $n \geqslant 3$. In this case, we obtain

$$\langle |E|^n \rangle \simeq \left| E^{(0)} \right|^n \left(\frac{|\varepsilon'_m|}{\varepsilon_d} \right)^{[s+(n-2)\nu_p]/(t+s)} \left(\frac{|\varepsilon'_m|}{\varepsilon''_m} \right)^{n-1} \tag{46}$$

For a $2d$ system, $t \approx s \approx \nu_p = \frac{4}{3}$ so that (46) gives

$$\langle |E|^n \rangle \sim \left| E^{(0)} \right|^n \left(\frac{|\varepsilon'_m|}{\varepsilon_d} \right)^{(n-1)/2} \left(\frac{|\varepsilon'_m|}{\varepsilon''_m} \right)^{n-1} \tag{47}$$

where $n \geqslant 3$. Because in the visible, infrared, and far-infrared spectral ranges the real part of the dielectric constant of a typical metal is large, $|\varepsilon'_m| \gg \varepsilon_d$, and losses are small, $|\varepsilon'_m| \gg \varepsilon''_m$, the values of the field moments $\langle |E|^n \rangle$ exceed the corresponding moments of the incident field, $|E^{(0)}|^n$, by several orders of magnitude. This indicates the presence of the giant field fluctuations in semicontinuous metal films in the visible and, especially, in the infrared spectral ranges.

For the Drude metal, we can simplify Eq. (47) for sufficiently small frequencies, $\omega \ll \omega_p$, as

$$\langle |E|^n \rangle \simeq |E^{(0)}|^n \left(\frac{\omega_p}{\omega_\tau \sqrt{\varepsilon_d}} \right)^{n-1} \tag{48}$$

From this equation it follows that for sufficiently small frequencies the local-field moments behave like $\langle |E|^n \rangle \propto (\omega_p/\omega_\tau)^{n-1}$.

The previous estimate of the moments can be used, for example, for Raman scattering that does not depend on the phases of local fields [7],

$$G_{RS} \sim \langle |E|^4 \rangle \sim \frac{|\varepsilon'_m|^{9/2}}{\varepsilon_d^{3/2} \varepsilon''^3_m} \tag{49}$$

(Note that although Raman scattering is a linear process, its enhancement is proportional to $|E|^4$ [7], and in that sense it is similar to nonlinear processes [5].)

Now we turn to nonlinear coherent processes. To estimate enhancements for nonlinear coherent processes, such as harmonic generation, one should average the nonlinear polarization, $P^{(n)} \propto \langle E^n \rangle$; the resultant enhancement is then given by $G^{(n)} \propto |P^{(n)}|^2 \propto |\langle E^n \rangle|^2$ [5]. Therefore the parametric nonlinear optical processes are very sensitive to the relative phases of the fields at different points on a film. It is impossible to estimate enhancements, in general, considering only the absolute values of the field. However, we can estimate the upper limit for the enhancements assuming that all the fields are in phase. Formally, the upper limit for the enhancements can be obtain by neglecting the phase fluctuations, that is, with the replacement of $\langle E^n \rangle$ for a nonlinear process of the nth order by $\langle |E|^n \rangle$. By doing so, we obtain the estimate given by Eq. (47).

We also note that a widely used "decoupling procedure," $\langle |E|^n \rangle \to \langle |E|^2 \rangle^{n/2}$ (see, for example, [79, 83]) results in significantly underestimated (by several orders of magnitude) enhancement, as follows from the preceding consideration. Accordingly, the mean-field theories based on the decoupling procedure are not applicable for systems with strong field fluctuations that provide largest enhancements for optical nonlinearities.

It is instructive to note that the field intensities in a semicontinuous film, $|E(x, y)|^2$, can be viewed as peaks with the amplitudes $(E^* l^*/a_0)^2$ separated by the distances $\gg a_0$ (see Eqs. (38) and (40)). The amplitudes of the peaks, as well as a typical distance between them, increase with decreasing frequency, ω. This picture is in a qualitative agreement with Figure 26, where the field fluctuations on a silver semicontinuous film are shown. We would like to stress out that despite the large distances between the field peaks the field fluctuations can be highly correlated in space [84].

Earlier, for the sake of simplicity, we assumed that $p = p_c$. Now we estimate the $(p - p_c)$ range, where the foregoing estimates are valid [7]. Although the previous estimates were done for the percolation threshold, $p = p_c$, they must be also valid in some vicinity to the threshold, where the size l^* of the renormalized squares is smaller than the percolation correlation length, $\xi_p \cong a_0(|p - p_c|/p_c)^{-\nu_p}$ that diverges at the percolation threshold. Equating the values of l^* from (38) and the foregoing ξ_p, we obtain the following estimation for the concentration range where the preceding enhancements can be observed,

$$\frac{|p - p_c|}{p_c} \leqslant \left(\frac{\varepsilon_d}{|\varepsilon'_m|} \right)^{1/(t+s)} \tag{50}$$

For a $2d$ semicontinuous metal film, the critical exponents are $s \approx t \approx \nu_p = \frac{4}{3}$, and the earlier relation acquires the form,

$$\frac{|p - p_c|}{p_c} \leqslant \left(\frac{\varepsilon_d}{|\varepsilon'_m|}\right)^{3/8} \tag{51}$$

For the Drude metal, in the frequency range $\omega_p^* \gg \omega \gg \omega_\tau$, Eq. (51) can be rewritten as follows,

$$\frac{|p - p_c|}{p_c} \leqslant \varepsilon_d{}^{3/8}\left(\frac{\omega}{\omega_p}\right)^{3/4} \tag{52}$$

As follows from Eq. (52), the concentration range for the enhancement shrinks when the frequency decreases much below the renormalized plasma frequency, $\omega_p^* = \omega_p/\sqrt{\varepsilon_b}$. This result is in agreement with our computer simulations [7].

5.5. Surface-Enhanced Raman Scattering

For Raman scattering from molecules adsorbed on the surface the enhancement factor is given by [7],

$$G_{RS} = \frac{\langle|\varepsilon(\mathbf{r})|^2|\mathbf{E}(\mathbf{r})|^4\rangle}{\varepsilon_d^2[\mathbf{E}^{(0)}]^4} \sim \frac{|\varepsilon'_m|^{9/2}}{\varepsilon_d^{3/2}\varepsilon''^3_m} \tag{53}$$

where the first formula is exact and the second formula is the scaling result (49) with the prefactor chosen to fit the numerical results (see later). Note that formula (53) differs from (3) by factor $|\varepsilon(\mathbf{r})/\varepsilon_d|^2$. The difference results from the fact that in (3) we assumed that both the Raman and linear polarizabilities are associated with the same site on a fractal surface, whereas to obtain (53) we assumed that the linear polarizability is due to a metal grain on the film but the Raman polarizability is due to a molecule adsorbed on the grain. However, because the largest fields occur at the dielectric gaps (with the metallic clusters closely approaching each other), $\varepsilon = \varepsilon_d$ at these points, and therefore the difference between the two formulas is not significant.

In Figure 29 results of our Monte Carlo simulations are shown for Raman scattering from a silver semicontinuous film at the percolation threshold (based on the first equality in (53)) and results of the calculations based on the approximate scaling formula (second equality in (53)). One can see that the scaling formula works well for almost all frequencies, except the small frequencies that are comparable to or smaller than the relaxation constant (where the scaling theory is not applicable).

In Figure 30 we show distributions of the local Raman signal enhancements on a silver semicontinuous film at $p = p_c$, for different wavelengths, $\lambda = 1.5$ μm, $\lambda = 10$ μm, and $\lambda = 20$ μm. The Raman signal distributions were calculated using the first formula in (53) but with no averaging over samples (so that the sign $\langle\cdots\rangle$ should be omitted in this case). As seen in the figure, the local enhancements have the forms of sharp peaks sparsely distributed on the film, with the magnitudes increasing toward the long-wavelength part of the spectrum. The enhancement in peaks achieve $\sim 10^9$, for $\lambda = 1.5$ μm, $\sim 10^{11}$, for $\lambda = 10$ μm, and $\sim 10^{14}$, for $\lambda = 20$ μm. The average enhancement, G_{RS}, is much less, of the order of 10^6, for all the wavelengths (see Fig. 29). As seen in Figure 30, the peak positions strongly depend on the frequency. This nontrivial pattern for the local SERS distribution can be probed by means of near-field optical microscopy [57]. If the density of Raman-active molecules is small enough, each peak in Figure 11 is due to Raman scattering from a *single* molecule. Thus the presented picture of the SERS distribution opens an unique opportunity to perform Raman spectroscopy of a single molecule on a semicontinuous metal film. Raman scattering from a single molecule was probed in the *far* zone [94].

The obtained distribution for the local SERS results from strong fluctuations of the local fields (and currents) near the percolation threshold. Because the enhancement is

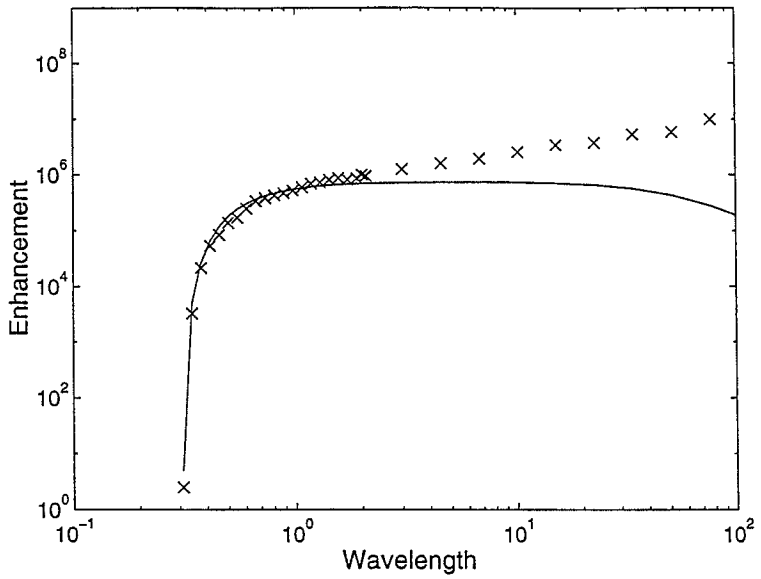

Fig. 29. Enhancement factors, G_{RS}, for Raman scattering from a silver semicontinuous film at the percolation threshold. The points are results of the numerical simulations; the solid line represents results of calculations based on the scaling result (53). (Source: Reprinted with permission from F. Brouers, S. Blacher, A. Lagarkov, A. K. Sarychev, P. Gadenne, and V. M. Shalaev, *Phys. Rev. B* 55, 13234 [1997]. © 1997 American Physical Society.)

proportional to the local field raised to the fourth power the largest contribution to the SERS signal comes from small areas where the fluctuating fields are especially high. These areas of large local fields are associated with the film eigenmodes that resonate at a given laser wavelength λ. When λ is changed new eigenmodes of a film are excited resulting again in the high local fields in the areas where the modes are located.

Note that all results are shown in the natural linear scales; therefore, what we see in the figures is a top part of the SERS distribution, that is, only the largest Stokes fields. The fields in other points forming a background, although smaller, are not, of course, zero (they cannot be seen simply because they are much smaller than the maximum fields). However, because the SERS $\propto |E(x, y)|^4$ only the largest fields play an important role and the smaller background fields (not seeing in the figures) do not contribute much to the signal.

In accordance with the previous considerations (see Fig. 25), for high frequencies, $\omega \leqslant \omega_p^*$ (for silver, $\lambda_p^* = 0.364$ nm), the local fields experience giant fluctuations. This is because at these frequencies, the real part of the metal dielectric constant, ε_m', is negative and its absolute values are of the order of ε_d. Therefore, at these frequencies, the plasmon resonance is effective for each of the metal grains that almost do not interact, provided p is well below p_c. At $p \approx p_c$, the particles' interactions become important; these interactions shift the resonance and thus they suppress the induced currents and the corresponding local fields. In accordance with this, SERS also decreases at $p \approx p_c$. However, for higher metal concentrations, $p \to 1$, the plasmon resonance associated with sparse dielectric voids (that almost do not interact at p close to 1) becomes effective, so that the local fields and corresponding SERS increase again at the larger p. Finally, at $p = 1$, the field fluctuations are absent and SERS is small. This double-maximum behavior in the SERS dependence on p is observed in experiments [7] and is in agreement with our numerical calculations based on formula (53). The results of our numerical simulations (averaged over 10 realizations) and experimental data are shown in Figure 31.

According to (53) and the Drude formula (29), SERS at the percolation threshold is frequency independent in the spectral range $\omega_p^* \gg \omega \gg \omega_\tau$, where $G_{RS} \propto (\omega_p/\omega_\tau)^3$.

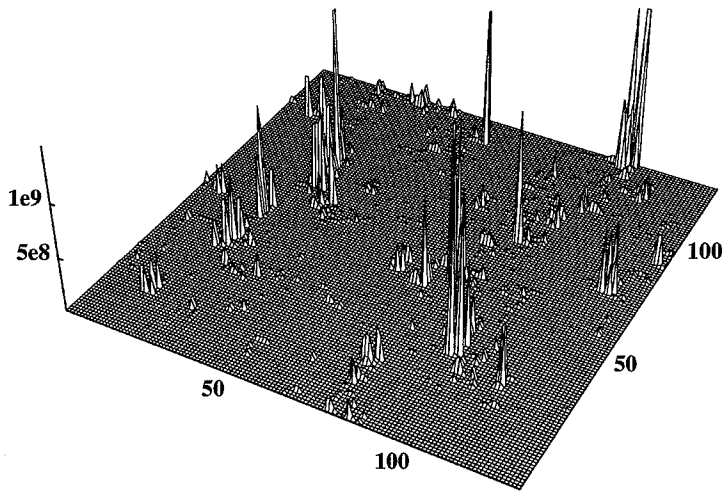

(a)

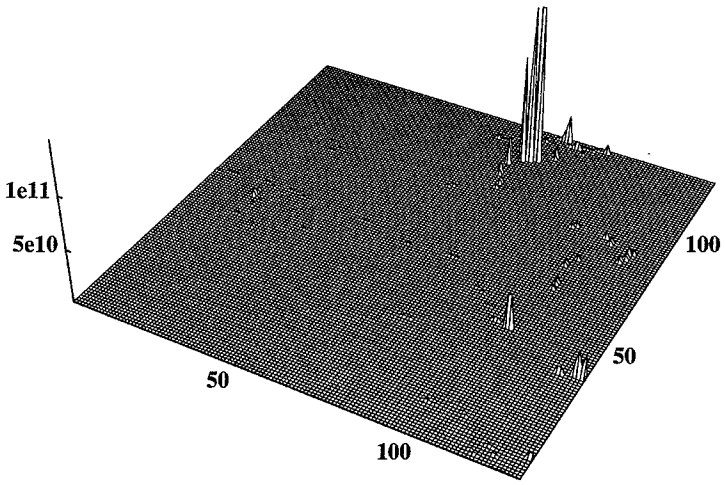

(b)

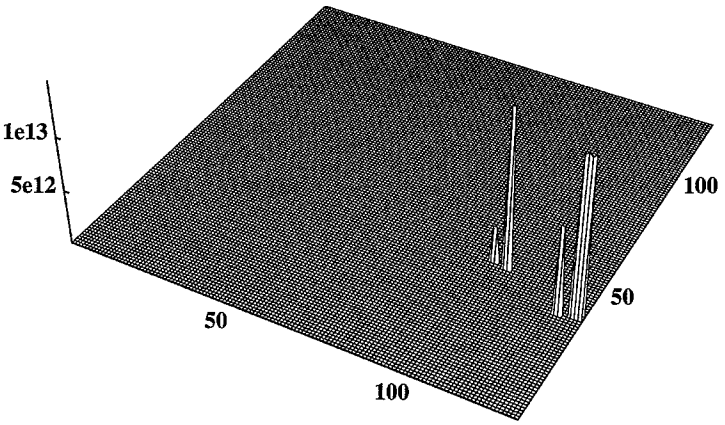

(c)

Fig. 30. Distributions of the local enhancements of Raman scattering on a silver semicontinuous film at the percolation threshold for different wavelengths: (a) $\lambda = 1.5$ μm, (b) $\lambda = 10$ μm, and (c) $\lambda = 20$ μm. (Source: Reprinted with permission from V. M. Shalaev and A. K. Sarychev, *Phys. Rev. B* 57, 13265 [1998]. © 1998 American Physical Society.)

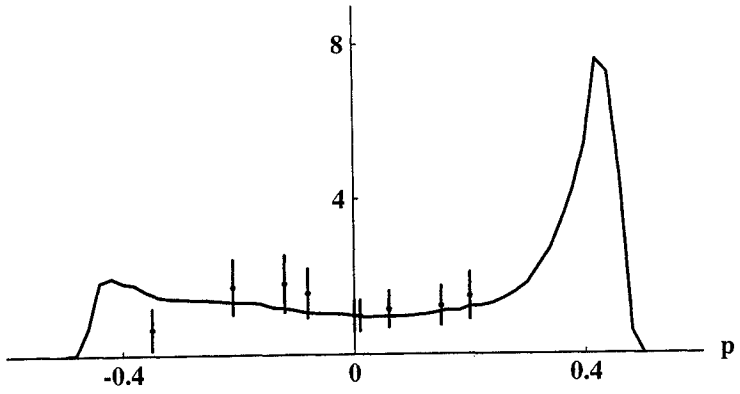

Fig. 31. The normalized SERS $\bar{G}_{RS} = G^0_{RS}(p)/G_{RS}(p = p_c)$ as a function of the metal concentration, $\Delta p = p - p_c$, on a silver semicontinuous film. (The solid line: theoretical calculations, the points: experimental data.) (Source: Reprinted with permission from P. Gadenne, F. Brouers, V. M. Shalaev, and A. K. Sarychev, *J. Opt. Soc. Am. B* 15, 68 [1998]. © 1998 Optical Society of America.)

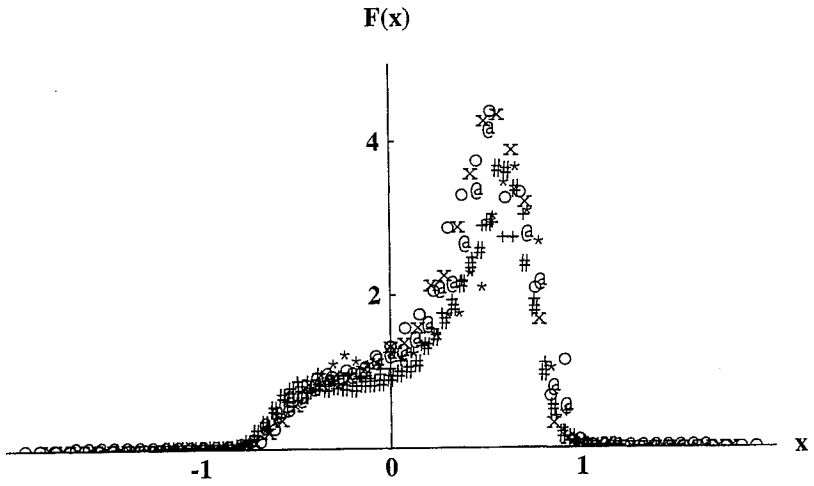

Fig. 32. The SERS scaling function, $F(x)$, as a function of $x = (p - p_c)/\Delta^*$ (see Eq. (54)), for different wavelengths: $\lambda = 0.9$ μm (#), $\lambda = 1.1$ μm (+), $\lambda = 1.3$ μm (*), $\lambda = 1.5$ μm (@), $\lambda = 1.7$ μm (×), and $\lambda = 1.9$ μm (○). (Source: Reprinted with permission from P. Gadenne, F. Brouers, V. M. Shalaev, and A. K. Sarychev, *J. Opt. Soc. Am. B* 15, 68 [1998]. © 1998 Optical Society of America.)

The scaling formula (53) gives the SERS enhancements at $p = p_c$. As pointed out previously, the scaling result is also valid approximately in some interval $\Delta p = p - p_c$ in a vicinity of p_c, when the size l^* is smaller than or equal to the percolation correlation length, $\xi_p \cong a_0|\Delta p|^{-\nu_p}$, which gives the estimation for the concentration range where the SERS occurs: $\Delta p \leqslant \Delta^* = (\varepsilon_d/|\varepsilon'_m|)^{1/(t+s)}$. Based on this estimate, the following scaling anzatz for the enhancement of Raman scattering was proposed [7],

$$G_{RS}(p, \omega) = G^0_{RS}(p_c, \omega) F\left(\frac{\Delta p}{\Delta^*}\right) \tag{54}$$

To find the scaling function $F(x)$, the quantity G_{RS} was calculated for various ω and p. For very different frequencies used in our simulations, the results collapse onto one curve $F(x)$ shown in Figure 32. This function first has a small maximum below p_c; at $p = p_c$, the function is $F(0) \approx 1$; then $F(x)$ has another larger maximum at $p > p_c$, and it finally vanishes, at $|\Delta p| > \Delta^*$. This double-peak behavior for $F(x)$ is associated with the

discussed previous evolution of the plasmon resonances with changing p and it reflects the dependence of SERS on p shown above in Figure 31. The asymmetry in $F(x)$ is related to a simple fact that, while the local-field distributions at some small p' and $1 - p'$ are qualitatively similar (resonances of metal grains and dielectric voids, respectively), the enhancement, G_{RS}, in (53) is proportional to $|\varepsilon(x, y)|^2$ whose amplitude, on average, is larger at p close to 1 (recall that $|\varepsilon_m| \gg \varepsilon_d$).

5.6. Nonlinear Optical Processes on Semicontinuous Metal Films

Now let molecules possessing the nonlinear susceptibility $\chi^{(n)}(-n\omega; \omega, \ldots, \omega)$ (that describes a process of the nth harmonic generation) be adsorbed on a dielectric substrate. Then the adding of metal grains on the film results in enhancement of the nth harmonic generation by the factor,

$$G_{n\mathrm{HG}} = \left| \left\langle \frac{\varepsilon_{n\omega}(\mathbf{r})}{\varepsilon_{d,n\omega}} \left[\frac{E_\omega(\mathbf{r})}{E_\omega^{(0)}} \right]^n \left[\frac{E_{n\omega}(\mathbf{r})}{E_{n\omega}^{(0)}} \right] \right\rangle \right|^2 \tag{55}$$

where $E_{n\omega}^{(0)}$ is the probe field oscillating at $n\omega$ and $E_{n\omega}(\mathbf{r})$ is the local *linear* field induced by $E_{n\omega}^{(0)}$. The slight difference between (55) and previously introduced (5) is due to the same reason as the difference between (53) and (3) (see the discussion following formula (53) earlier).

We calculated distributions for the local enhancements of second harmonic generation (SHG), using the formula,

$$g_{\mathrm{SHG}}(\mathbf{r}) = \frac{\varepsilon_{2\omega}(\mathbf{r})}{\varepsilon_{d,2\omega}} \left[\frac{E_\omega(\mathbf{r})}{E_\omega^{(0)}} \right]^2 \tag{56}$$

For simplicity, we assumed in (56) that there is no "secondary" enhancement for the generated field at frequency 2ω. The distribution of the local SHG enhancements, $g_{\mathrm{SHG}}(\mathbf{r})$, are shown in Figure 33 for $\lambda = 0.5$ and $\lambda = 20$ μm at $p = p_c$. Similar to the case of the SERS local distributions, the peaks in the SHG become much larger with the increase of the wavelength. The spatial separations between them also increase with λ. For the hot spots the local enhancement can be giant, reaching values up to 10^{15}, whereas the ensemble-average enhancement is relatively small. The reason for this is, in part, the destructive interference between generated fields in different points, and, in part, the fact that the peaks are separated by distances significantly larger than their spatial sizes.

Huge enhancements for Raman scattering, SHG, and other nonlinear optical scattering, that significantly exceed the ensemble average enhancements, opens a fascinating possibility to perform Raman and nonlinear spectroscopy for a single molecule.

6. CONCLUSION

In this chapter we considered surface-enhanced optical phenomena in objects with fractal morphology, such as aggregates of nanoparticles, self-affine surfaces, and random metal-dielectric thin films. We showed that optical modes of such nanostructured random objects consist of localized sharp peaks resulting in very inhomogeneous spatial distributions of local fields. In peaks (hot spots), local fields exceed the applied field by several orders of magnitudes. These peaks are localized in nm-sized areas and they result from the excitation of the fractal plasmon modes. The strongly fluctuating fields associated with the sharp peaks in various random parts of a fractal lead to giant enhancements of optical processes, especially, nonlinear ones that are proportional to the enhanced local field raised to a power higher than 1. We considered enhancements for a number of optical phenomena, including Raman scattering, nonlinear refraction and absorption, and second and higher harmonic generation.

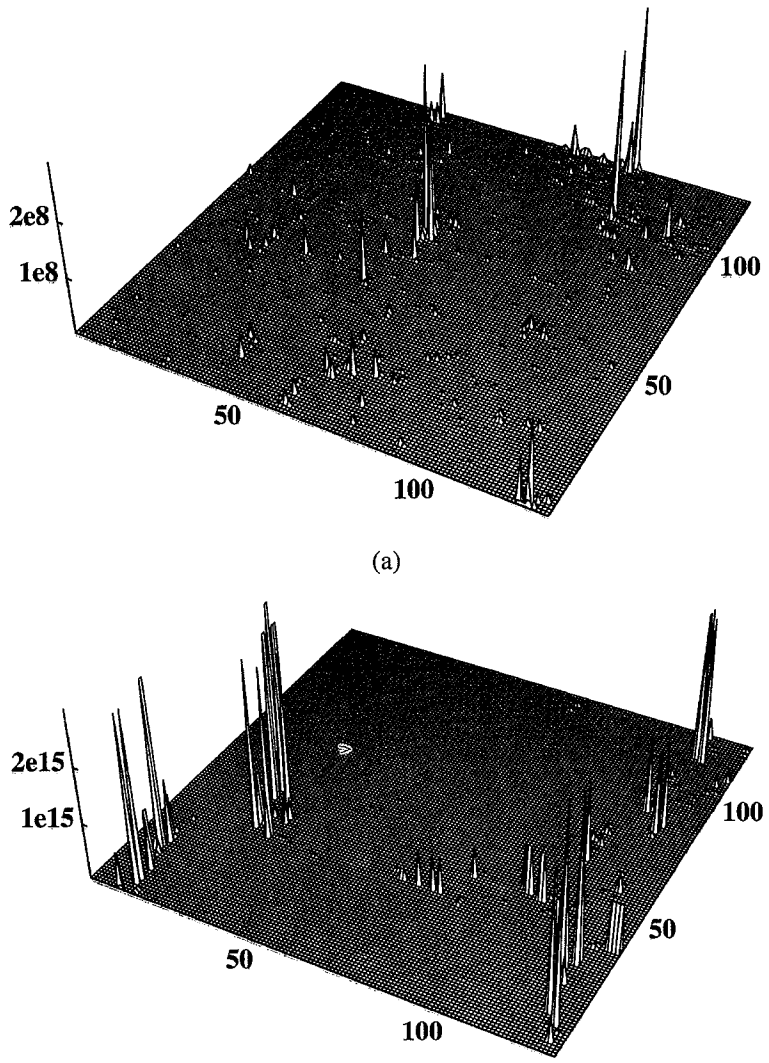

Fig. 33. Distributions of the local SHG enhancements, $g_{SHG}(\mathbf{r})$, for (a) $\lambda = 0.5\ \mu$m and (b) $\lambda = 20\ \mu$m. The film sizes are 512×512. (Source: Reprinted with permission from V. M. Shalaev and A. K. Sarychev, *Phys. Rev. B* 57, 13265 [1998]. © 1998 American Physical Society.)

As a result of such a pattern for the local-field distribution, the nonlinear signal is mostly generated from very small nm-sized areas so that the corresponding spatial distributions for the generated fields also look as a set of very sharp peaks. The enhancement in these peaks is much larger (by several orders of magnitude) than the ensemble-average enhancement partially because the peaks are separated by distances much larger than the mode spatial sizes. Another important reason is related to the fact that the well-separated peaks represent often topologically disconnected parts of the same mode and therefore are correlated in phase. Destructive (in part) interference between the local field in different parts of a film results in the decreased average enhancements. Note that the latter mechanism of the destructive interference is not important for incoherent processes, such as Raman scattering.

It is shown experimentally that, in accordance with the theoretical predictions, the degree of localization of optical excitations increases toward longer wavelengths. In accor-

dance with this, both the local and the average enhancements for nonlinear optical processes strongly increase toward the long-wavelength part of the spectrum.

Because the applied (fundamental) and generated fields have, in general, different frequencies and polarizations, they excite different fractal eigenmodes so that the field spatial distributions for the fundamental and generated waves are different as well. Accordingly, the spatial positions of the hot spots at the fundamental and generated frequencies are located, in general, in different parts of a fractal object.

This picture is expected to be typical for various optical processes in strongly disordered systems, such as the random nanostructured materials studied here. Specifically, hot spots associated with fields at different frequencies and polarizations are localized in spatially separated nm-sized areas. Note also that because the hot spots are localized in nm-sized areas and they provide giant enhancement in their locations, the unique opportunity to experimentally study *nonlinear* light scattering by a single molecule on a fractal nanomaterial becomes feasible. These novel nano-optical effects can be probed, for example, with near-field scanning optical microscopy providing the subwavelength spatial resolution.

Acknowledgments

This research was supported in part by NSF under Grants DMR 9810183 and DMR 9623663, and by NATO Grant CRG 950097. Also, acknowledgment is made to the donors of The Petroleum Research Fund, administered by the ACS, for partial support of this research.

References

1. A. Bunde, ed., "Fractals & Disorder," North-Holland, Amsterdam, 1992; S. Havlin and A. Bunde, "Fractals & Disorder," p. 97, North-Holland, Amsterdam, 1992; S. Alexander and R. Orbach, *J. Phys. Lett.* 43, L1625 (1982); R. Rammal and G. Toulouse, *J. Phys. Lett.* 44, L13 (1983); B. Sapoval, T. Gobron, and X. X. Margolina, *Phys. Rev. Lett.* 67, 2974 (1991).
2. V. M. Shalaev, *Phys. Rep.* 272, 61 (1996).
3. D. P. Tsai, J. Kovacs, Z. Wang, M. Moskovits, V. M. Shalaev, J. Suh, and R. Botet, *Phys. Rev. Lett.* 72, 4149 (1994); V. M. Shalaev and M. Moskovits, *Phys. Rev. Lett.* 75, 2451 (1995).
4. Y. E. Danilova and V. P. Safonov, in "Fractals Reviews in the Natural and Applied Sciences" (M. M. Novak, ed.), p. 101, Chapman & Hall, London, 1995.
5. V. M. Shalaev, E. Y. Poliakov, and V. A. Markel, *Phys. Rev. B* 53, 2437 (1996); V. A. Markel, V. M. Shalaev, E. B. Stechel, W. Kim, and R. L. Armstrong, *Phys. Rev. B* 53, 2425 (1996).
6. V. M. Shalaev, R. Botet, J. Mercer, and E. B. Stechel, *Phys. Rev. B* 54, 8235 (1996); E. Y. Poliakov, V. M. Shalaev, V. A. Markel, and R. Botet, *Opt. Lett.* 21, 1628 (1996); E. Y. Poliakov, V. A. Markel, V. M. Shalaev, and R. Botet, *Phys. Rev. B* 57, 14901 (1998).
7. F. Brouers, S. Blacher, A. Lagarkov, A. K. Sarychev, P. Gadenne, and V. M. Shalaev, *Phys. Rev. B* 55, 13234 (1997); P. Gadenne, F. Brouers, V. M. Shalaev, and A. K. Sarychev, *J. Opt. Soc. Am. B* 15, 68 (1998); V. M. Shalaev and A. K. Sarychev, *Phys. Rev. B* 57, 13265 (1998).
8. R. Jullien and R. Botet, "Aggregation and Fractal Aggregates," World Scientific, Singapore, 1987; J. Feder, "Fractals," Plenum, New York, 1988.
9. R. Chiarello, V. Panella, J. Krim, and C. Thompson, *Phys. Rev. Lett.* 67, 3408 (1991); C. Douektis, Z. Wang, T. L. Haslett, and M. Moskovits, *Phys. Rev. B* 51, 11,022 (1995); A. L. Barbasi and H. E. Stanley, "Fractal Concepts in Surface Growth," Cambridge Univ. Press, Cambridge, U.K., 1995.
10. V. A. Markel, L. S. Muratov, M. I. Stockman, and T. F. George, *Phys. Rev. B* 43, 8183 (1991); M. I. Stockman, L. N. Pandey, L. S. Muratov, and T. F. George, *Phys. Rev. Lett.* 72, 2486 (1994); M. I. Stockman, L. N. Pandey, L. S. Muratov, and T. F. George, *Phys. Rev. B* 51, 185 (1995); M. I. Stockman, L. N. Pandey, and T. F. George, *Phys. Rev. B* 53, 2183 (1996).
11. M. Moskovits, *Rev. Mod. Phys.* 57, 783 (1985); A. Otto, I. Mrozek, H. Grabhorn, and W. Akemann, *J. Phys. Condens. Matter* 4, 1143 (1992); "Surface Enhance Raman Scattering" (R. K. Chang and T. E. Furtak, eds.), Plenum, New York, 1982; M. I. Stockman, V. M. Shalaev, M. Moskovits, R. Botet, and T. F. George, *Phys. Rev. B* 46, 2821 (1992).
12. V. M. Shalaev and M. I. Stockman, *JETP* 65, 287 (1987); A. V. Butenko, V. M. Shalaev, and M. I. Stockman, *JETP* 67, 60 (1988).

13. D. J. Bergman and D. Stroud, *Solid State Phys.* 46, 147 (1992).
14. R. W. Boyd, "Nonlinear Optics," Academic Press, New York, 1992.
15. S. G. Rautian, V. P. Safonov, P. A. Chubakov, V. M. Shalaev, and M. I. Shtockman, *JETP Lett.* 47, 243 (1988); A. V. Butenko, P. A. Chubakov, Y. E. Danilova, S. V. Karpov, A. K. Popov, S. G. Rautian, V. P. Safonov, V. V. Slabko, V. M. Shalaev, and M. I. Stockman, *Z. Phys D* 17, 283 (1990).
16. J. J. Jackson, "Classical Electrodynamics," Wiley, 1975.
17. P. B. Johnson and W. Christy, *Phys. Rev. B* 6, 3470 (1972).
18. J. E. Sansonetti and J. K. Furdyna, *Phys. Rev. B* 22, 2866 (1980).
19. U. Kreibig and L. Genzel, *Surf. Sci.* 156, 678 (1985); U. Kreibig and P. Zacharis, *Z. Phys.* 231, 128 (1970); U. Kreibig and M. Vollmer, "Optical Properties of Metal Clusters," Springer-Verlag, Berlin, Heidelberg, 1995.
20. M. Ausloos, P. Clippe, and A. A. Lucas, *Phys. Rev. B* 18, 7176 (1978).
21. P. Clippe, R. Evrard, and A. A. Lucas, *Phys. Rev. B* 14, 1751 (1976).
22. J. M. Gerardyand and M. Ausloos, *Phys. Rev. B* 22, 4950 (1980).
23. F. Claro, *Solid State Commun.* 29, 229 (1984).
24. E. M. Purcell and C. R. Pennypacker, *Astrophys. J.* 186, 705 (1973).
25. B. T. Draine, *Astrophys. J.* 333, 848 (1988).
26. S. B. Singham and C. F. Bohren, *J. Opt. Soc. Am. A* 11, 1867 (1988).
27. V. A. Markel, *J. Mod. Opt.* 40, 2281 (1993).
28. D. Weitz and M. Oliveria, *Phys. Rev. Lett.* 52, 1433 (1984); J. A. Creighton, in "Surface Enhanced Raman Scattering" (R. K. Chang and T. E. Furtak, eds.), Plenum, New York, 1982.
29. Y. E. Danilova, N. N. Lepeshkin, S. G. Rautian, and V. P. Safonov, *Physica A* 241, 231 (1997); Y. E. Danilova, V. A. Markel, and V. P. Safonov, *Atmos. Oceanic Opt.* 6, 821 (1993).
30. Y. E. Danilova, V. P. Drachev, S. V. Perminov, and V. P. Safonov, *Bull. Russian Acad. Sci. Phys.* 60, 342 (1996); *Bull. Russian Acad. Sci. Phys.* 60, 374 (1996).
31. S. I. Bozhevolnyi, V. A. Markel, V. Coello, W. Kim, and V. M. Shalaev, *Phys. Rev. B* 58, 11441 (1998).
32. C. Flytzanis, *Prog. Opt.* 29, 2539 (1992); D. Ricard, P. Roussignol, and C. Flytzanis, *Opt. Lett.* 10, 511 (1985); F. Hache, D. Ricard, C. Flytzanis, and U. Kreibig, *Appl. Phys. A* 47, 347 (1988).
33. M. Sheik-Bahae, A. A. Said, T. H. Wei, D. J. Hagan, and E. W. VanStryland, *IEEE J. Quantum Electron.* Q26, 760 (1990).
34. F. A. Zhuravlev, N. A. Orlova, V. V. Shelkovnikov, A. I. Plehanov, S. G. Rautian, and V. P. Safonov, *JETP Lett.* 56, 260 (1992).
35. A. W. Olsen and Z. H. Kafafi, *J. Am. Chem. Soc.* 113, 7758 (1991).
36. M. P. Andrews, M. G. Kuzyk, and F. Ghbremichael, *Nonlin. Opt.* 6, 103 (1993).
37. I. A. Akimov, A. V. Baranov, V. M. Dubkov, V. I. Petrov, and E. A. Sulabe, *Opt. Spectrosc.* 63, 1276 (1987).
38. J. E. Sipe and R. W. Boyd, *Phys. Rev. B* 46, 1614 (1992); R. J. Gehr, G. L. Fisher, R. W. Boyd, and J. E. Sipe, *Phys. Rev. A* 53, 2792 (1996); G. L. Fisher, R. W. Boyd, R. J. Gehr, S. A. Jenekhe, J. A. Osaheni, J. E. Sipe, and L. A. Weller-Brophy, *Phys. Rev. Lett.* 74, 1871 (1995); R. W. Boyd, R. J. Gehr, G. L. Fisher, and J. E. Sipe, *Pure Appl. Opt.* 5, 505 (1996).
39. S. V. Karpov, A. K. Popov, S. G. Rautian, V. P. Safonov, V. V. Slabko, V. M. Shalaev, and M. I. Stockman, *JETP Lett.* 48, 571 (1988); Y. E. Danilova, A. I. Plekhanov, and V. P. Safonov, *Physica A* 185, 61 (1992).
40. V. P. Safonov, V. M. Shalaev, V. A. Markel, Y. E. Danilova, N. N. Lepeshkin, W. Kim, S. G. Rautian, and R. L. Armstrong, *Phys. Rev. Lett.* 80, 1102 (1998).
41. H. Zhu and R. S. Averback, *Philos. Mag. Lett.* 73, 27 (1996).
42. K. Baba, K. Yamaki, and M. Miyagi, "Chemistry and Physics of Small-scale Structures," Technical Digest Series, Vol. 2, p. 52, Optical Society of America, Santa Fe, NM, 1997.
43. For a spheroid, there are three non-degenerate resonances with non-zero total dipole moment.
44. J. M. Kim and J. M. Kosterlitz, *Phys. Rev. Lett.* 62, 2289 (1989).
45. The complete set of formulas for the case of electromagnetic waves scattering from smooth random surfaces can be found in Refs. [46, 47].
46. A. Marvin, T. Toigo, and V. Celli, *Phys. Rev. B* 11, 2777 (1975); F. Toigo, A. Marvin, V. Celli, and N. Hill, *Phys. Rev. B* 15, 5618 (1977).
47. A. A. Maradudin and D. L. Mills, *Phys. Rev. B* 11, 1392 (1975).
48. P. Beckmann and A. Spizzichino, "The Scattering of Electromagnetic Waves from Rough Surfaces," Artech House, Norwood, MA, 1987.
49. A. Ishimaru, in "Scattering in Volumes and Surfaces" (M. Nieto-Vesperinas and J. C. Dainity, eds.), Elsevier, North-Holland, Amsterdam, 1990.
50. R. M. Fitzgerland and A. A. Maradudin, *Waves Random Media* 4, 275 (1994).
51. P. Chappetta, *J. Phys. A Math. Gen.* 13, 2101 (1980); D. Keller and C. Bustamente, *J. Chem. Phys.* 84, 2961 (1986).
52. S. B. Singham and C. F. Bohren, *J. Opt. Soc. Am. A* 5, 1867 (1988).
53. M. K. Singham, S. B. Singham, and G. C. Salzman, *J. Chem. Phys.* 85, 3807 (1986); P. J. Flatau, G. L. Stephens, and B. T. Draine, *J. Opt. Soc. Am. A* 7, 593 (1990); C. E. Dungley and C. F. Bohren, *J. Opt. Soc. Am. A* 8, 81 (1991).

54. M. V. Berry and I. C. Percival, *Opt. Acta* 33, 577 (1986).
55. V. M. Shalaev, R. Botet, and R. Jullien, *Phys. Rev. B* 44, 12126 (1991).
56. V. M. Shalaev, R. Botet, and A. V. Butenko, *Phys. Rev. B* 48, 6662 (1993).
57. E. Betzig, et al., *Science* 257, 189 (1992).
58. A. Petri and L. Pietronero, *Phys. Rev. B* 45, 12,864 (1992).
59. R. W. Cohen, G. D. Cody, M. D. Coutts, and B. Abeles, *Phys. Rev. B* 8, 3689 (1973).
60. G. A. Niklasson and C. G. Granqvist, *J. Appl. Phys.* 55, 3382 (1984).
61. J. P. Clerc, G. Giraud, and J. M. Luck, *Adv. Phys.* 39, 191 (1990).
62. D. Stauffer and A. Aharony, "Introduction to Percolation Theory," 2nd ed., Taylor and Francis, Philadelphia, 1991.
63. Y. Yagil, P. Gadenne, C. Julien, and G. Deutscher, *Phys. Rev.* 46, 2503 (1992).
64. T. W. Noh, P. H. Song, S.-I. Lee, D. C. Harris, J. R. Gaines, and J. C. Garland, *Phys. Rev.* 46, 4212 (1992).
65. P. Gadenne, A. Beghadi, and J. Lafait, *Opt. Commun.* 65, 17 (1988).
66. P. Gadenne, Y. Yagil, and G. Deutscher, *J. Appl. Phys.* 66, 3019 (1989).
67. Y. Yagil, M. Yosefin, D. J. Bergman, G. Deutscher, and P. Gadenne, *Phys. Rev. B* 43, 11,342 (1991).
68. A. N. Lagarkov, K. N. Rozanov, A. K. Sarychev, and A. N. Simonov, *Physica A* 241, 199 (1997).
69. J. C. Maxwell Garnett, *Philos. Trans. R. Soc. London* 203, 385 (1904).
70. D. A. G. Bruggeman, *Ann. Phys. Leipzig* 24, 636 (1935).
71. F. Brouers, J. P. Clerc, and G. Giraud, *Phys. Rev. B* 44, 5299 (1991); F. Brouers, J. M. Jolet, G. Giraud, J. M. Laugier, and Z. A. Randriamanantany, *Physica A* 207, 100 (1994).
72. A. P. Vinogradov, A. M. Karimov, and A. K. Sarychev, *Zh. Eksp. Teor. Fiz.* 94, 301 (1988); [*Sov. Phys. JETP* 67, 2129 (1988)].
73. G. Depardieu, P. Frioni, and S. Berthier, *Physica A* 207, 110 (1994).
74. A. K. Sarychev, D. J. Bergman, and Y. Yagil, *Physica A* 207, 372 (1994); *Phys. Rev. B* 51, 5366 (1995).
75. L. de Arcangelis, S. Redner, and H. J. Herrmann, *J. Phys. Lett.* 46, L585 (1985); P. M. Duxbury, P. L. Leath, and P. D. Beale, *Phys. Rev. B* 36, 367 (1987); B. Khang, G. G. Bartrouni, S. Redner, L. de Arcangelis, and H. J. Herrmann, *Phys. Rev. B* 37, 7625 (1988); A. P. Vinogradov, A. V. Goldenshtein, and A. K. Sarychev, *Zh. Tekh. Fiz.* 59, 208 (1989).
76. H. J. Herrmann and S. Roux, eds., "Statistical Models for the Fracture of Disordered Media," Elsevier, North-Holland, Amsterdam, 1990; P. Meakin, *Science* 252, 226 (1991); P. M. Duxbury and P. L. Leath, *Phys. Rev. B* 49, 12,676 (1994).
77. K. K. Bardhan and R. K. Chakrabarty, *Phys. Rev. Lett.* 72 (1994); U. N. Nandi and K. K. Bardhan, *Europhys. Lett.* 31, 101 (1995).
78. A. K. Sarychev and F. Brouers, *Phys. Rev. Lett.* 73, 2895 (1994).
79. D. Stroud and P. M. Hui, *Phys. Rev. B* 37, 8719 (1988); P. M. Hui and D. Stroud, *Phys. Rev. B* 49, 11,729 (1994); D. Stroud and X. Zhang, *Physica A* 207, 55 (1994); X. Zhang and D. Stroud, *Phys. Rev. B* 49, 944 (1994).
80. D. J. Bergman, *Phys. Rev. B* 39, 4598 (1989); O. Levy, D. J. Bergman, and D. G. Stroud, *Phys. Rev. E* 52, 3184 (1995); D. Bergman, O. Levy, and D. Stroud, *Phys. Rev. B* 49, 129 (1994); O. Levy and D. Bergman, *Physica A* 207, 157 (1994); O. Levy, D. J. Bergman, and D. G. Stroud, *Phys. Rev. E* 52, 3184 (1995); D. Bergman, O. Levy, and D. Stroud, *Phys. Rev. B* 49, 129 (1994); O. Levy and D. Bergman, *Physica A* 207, 157 (1994).
81. V. M. Shalaev, V. P. Safonov, E. Y. Poliakov, V. A. Markel, and A. K. Sarychev, in "Nanostructured Materials: Clusters, Composites, and Thin Films" (V. M. Shalaev and M. Moskovits, eds.), Vol. 679, p. 88, ACS Symposium Series, Am. Chem. Soc., Washington, DC, 1997.
82. V. M. Shalaev, E.Y. Poliakov, V. A. Markel, and R. Botet, *Physica A* 241, 249 (1997); V. M. Shalaev, M. I. Stockman, and R. Botet, *Physica A* 185, 181 (1992); V. M. Shalaev, V. A. Markel, and V. P. Safonov, *Fractals* 2, 201 (1994); V. M. Shalaev et al., *Physica A* 207, 197 (1994).
83. K. W. Yu, Y. C. Wang, P. M. Hui, and G. Q. Gu, *Phys. Rev. B* 47, 1782 (1993); K. W. Yu, P. M. Hui, and D. Stroud, *Phys. Rev. B* 47, 14,150 (1993); W. M. V. Wan, H. C. Lee, P. M. Hui, and K. W. Yu, *Phys. Rev. B* 54, 3946 (1996); K. W. Yu, *Phys. Rev. B* 49, 9989 (1994); K. W. Yu, P. M. Hui, and H.-C. Lee, *Phys. Lett.* 210, 115 (1996); P. M. Hui, *Phys. Rev. B* 49, 15,344 (1994); K. W. Yu, Y. C. Chu, and E. M. Y. Chan, *Phys. Rev. B* 50, 7984 (1994); P. M. Hui and K. H. Chung, *Physica A* 231, 408 (1996); L. Gao and Z. Li, *Phys. Lett. A* 222, 207 (1996); X. Liu and Z. Li, *Phys. Lett. A* 223, 475 (1996); C. Zhang, X. Wu, and S. Wu, *Phys. Rev. B* 54, 16,349 (1996).
84. F. Brouers, S. Blacher, and A. K. Sarychev, in "Fractals in the Natural and Applied Sciences" (M. Novak, ed.), Chap. 24, Chapman and Hall, London, 1995.
85. J. P. Clerc, G. Giraud, and J. M. Luck, *Adv. Phys.* 39, 191 (1990).
86. F. Brouers, J. P. Clerc, and G. Giraud, *Phys. Rev. B* 47, 666 (1993).
87. A. M. Dykhne, *Zh. Eksp. Teor. Fiz.* 59, 110 (1970); [*Sov. Phys. JETP* 32, 348 (1971)].
88. S. I. Bozhevolnyi, I. I. Smolyaninov, and A. V. Zayats, *Phys. Rev. B* 51, 17,916 (1995).
89. P. J. Reynolds, W. Klein, and H. E. Stanley, *J. Phys. C* 10, L167 (1977).

90. A. K. Sarychev, *Zh. Eksp. Teor. Fiz.* 72, 1001 (1977); [*Sov. Phys. JETP* 45, 524 (1977)].
91. J. Bernasconi, *Phys. Rev. B* 18, 2185 (1978).
92. A. Aharony, *Physica A* 205, 330 (1994).
93. D. J. Frank and C. J. Lobb, *Phys. Rev. B* 37, 302 (1988).
94. K. Kneipp et al., *Phys. Rev. Lett.* 78, 1667 (1997); S. Nie and S. R. Emory, *Science* 275, 1102 (1997).